UC Davis
UC Davis Electronic Theses and Dissertations

Title

A Study of Galaxy Evolution and Cosmology using Early-type Galaxies at Intermediate Redshift

Permalink

https://escholarship.org/uc/item/7dx0d731

Author

Mozumdar, Pritom

Publication Date

2024

Peer reviewed|Thesis/dissertation

eScholarship.org Powered by the California Digital Library
University of California

A Study of Galaxy Evolution and Cosmology using Early-type Galaxies at Intermediate Redshift

By

Pritom Mozumdar
Dissertation

Submitted in partial satisfaction of the requirements for the degree of

Doctor of Philosophy

in

Physics

in the

Office of Graduate Studies

of the

University of California

Davis

Approved:

Christopher Fassnacht, Chair

David Wittman

Tucker Jones

Committee in Charge

2024

Copyright © 2024 by
Pritom Mozumdar
All rights reserved.

Contents

List of Figures . . . vii
List of Tables . . . xxiv
Abstract . . . xxvi
Acknowledgments . . . xxvii

1 Introduction **1**
1.1 ETGs to probe galaxy evolution . . . 1
1.1.1 Evolution of rotational support in ETGs . . . 2
1.1.2 Evolution of total density slope . . . 3
1.2 ETGs to resolve the Hubble tension . . . 5
1.2.1 Theoretical background . . . 5
1.2.2 Stellar kinematics of ETGs to measure H_0 . . . 9
1.3 Overview of this dissertation . . . 10

2 Kinematics of lens galaxies from slit spectroscopy **12**
2.1 Introduction . . . 13
2.2 Targets . . . 15
2.2.1 J0147+4630 . . . 17
2.2.2 B0445+123 . . . 17
2.2.3 B0631+519 . . . 17
2.2.4 J0659+1629 . . . 17
2.2.5 J0818-2613 . . . 18
2.2.6 J0924+0219 . . . 18
2.2.7 J1433+6007 . . . 18
2.2.8 J1817+2729 . . . 18
2.3 Observations and data reduction . . . 19
2.3.1 Observations . . . 19
2.3.2 Data reduction . . . 24
2.3.3 Forward modeling and 1D extraction . . . 26

2.4 Data analysis . . . 27
2.4.1 Redshift measurement . . . 27
2.4.2 Velocity dispersion measurement . . . 28
2.5 Discussion . . . 31
2.5.1 Comparison to previous redshift and velocity dispersion measurements . . . 31
2.5.2 Comparison to predictions from SIS lens models . . . 31
2.6 Conclusion . . . 33

3 A MUSE sample of early-type galaxies at intermediate redshift 35
3.1 Introduction . . . 35
3.2 MUSE sample selection . . . 38
3.3 Data reduction . . . 39
3.3.1 Stellar kinematics . . . 43
3.3.2 Photometry . . . 45
3.4 Data analysis . . . 45
3.4.1 Measuring size and ellipticity . . . 46
3.4.2 Measuring kinematic properties . . . 46
3.4.3 Measuring stellar population . . . 48
3.5 Results and discussions . . . 53
3.5.1 λ_R confirms visual kinematic classification . . . 53
3.5.2 Kinematic misalignment . . . 55
3.5.3 Global stellar population properties . . . 55
3.6 Conclusion . . . 59

4 Early-type galaxies exhibit increased rotational support at intermediate redshift 61
4.1 Introduction . . . 61
4.2 MUSE sample and data products . . . 63
4.2.1 MUSE sample selection and kinematics extraction . . . 63
4.2.2 MUSE data products . . . 64
4.3 Reference MaNGA local sample . . . 64
4.3.1 MaNGA survey and kinematics data . . . 64

4.3.2 Structural and stellar properties of MaNGA sample . . . 64
4.3.3 MaNGA sample selection . . . 66
4.4 Correction of the observed λ_R for the MUSE sample . . . 67
4.4.1 Fitting for Sérsic index . . . 68
4.4.2 Applying correction for PSF effects . . . 70
4.5 Results and discussion . . . 73
4.5.1 λ_R in M_* - σ plane . . . 73
4.5.2 Measuring redshift evolution of rotational support . . . 74
4.6 Robustness of results . . . 78
4.6.1 Comparing structural properties from MGE and Sérsic fit . . . 78
4.6.2 Comparing Sérsic index from different apertures . . . 78
4.6.3 Effects of aperture size on λ_R . . . 80
4.6.4 Comparing λ_R from different apertures of MUSE galaxies to MaNGA . . . 81
4.7 Conclusion . . . 82

5 Evolution in the total mass density slopes of early-type galaxies at intermediate redshift 84
5.1 Introduction . . . 84
5.2 Data . . . 86
5.2.1 Sample selection . . . 87
5.2.2 Stellar kinematics and photometry . . . 87
5.3 Analysis method . . . 89
5.3.1 Jeans anisotropic modelling . . . 89
5.3.2 Multi-Gaussian expansion . . . 92
5.3.3 Mass models and kinematic anisotropy . . . 94
5.3.4 Fitting procedure . . . 99
5.3.5 Measuring dynamical quantities . . . 100
5.4 Results and discussion . . . 102
5.4.1 Comparing different JAM models . . . 102
5.4.2 Correlations of total density slope with galaxy properties . . . 104
5.4.3 Redshift evolution within the MUSE sample . . . 106

5.4.4 Redshift evolution with other dynamical and lensing studies 110
5.5 Conclusion 116

6 Summary and future work **118**
6.1 Stellar kinematics of ETGs to increase precision of H_0 118
6.2 A MUSE sample of ETGs to study galaxy evolution 119
6.3 ETGs show evidence of a decrease in rotation support over cosmic time 120
6.4 Redshift evolution of the total density slope of ETGs 120
6.5 Future work 121
6.6 Final remarks 123

List of Figures

1.1 Discrepancy in inferred and measured H_0 values from early and late Universe distant anchors, a.k.a. Hubble tension (Verde et al., 2019). The inferred H_0 utilizing data from the early Universe is clustered around 67 km s^{-1} Mpc^{-1}while the measurements from different late Universe distant anchors are around 74 km s^{-1} Mpc^{-1}. The combined discrepancy considering all measurements from the early and late Universe shown in this plot is 6.1σ 6

1.2 Strong lensing of the background quasar by the foreground galaxy creates four images of the source and variations in light travel time from each of these lensed images along with other data sets, allow us to measure H_0 via time-delay cosmography method (Illustration: Martin Millon/Swiss Federal Institute of Technology Lausanne. Galaxy and quasar image: Hubble Space Telescope/NASA). 7

2.1 Images of the lens systems, part of the collected 2D spectra, and the corresponding 1D spatial profiles. The 1D spatial profiles have been generated by collapsing the data in the 2D spectra along the spectral axis. The slit position (green) for each lens system is also shown. For the lens system, J0147+4630, J0659+1629, J0818-2613, J1433+6007, and J1817+2729, we have used archival *HST* images (PI: T. Treu) and for B04453+123, B0631+519 and J0924+0219, we have used ground based AO images (PI: C. D. Fassnacht). 19

2.2 Illustration of model fitting to 1D spatial profiles. Left column - each row shows the 1D spatial profile (blue) with individual model components for a single lens system. The model components are Moffat profiles, which represent the deflector and lensed quasars, with an additive polynomial function representing the background. The profile component representing the deflector is marked black and other profile components generally representing the lensed quasar images are marked with yellow. Right column - The top panel in each row shows the 1D spatial profile (blue) with 1σ uncertainty (orange) and the corresponding model (green) that fits the data in that profile. The bottom panel shows the residual (red) between the data and the model normalised to the uncertainties in data. The uncertainties on the spatial profiles of B0445+123 and B0631+519 are higher compared to others because these 1D profiles were generated from single frames, while for other lens systems, the corresponding profiles were generated from coadded frames. 20

2.3 1D spectra and velocity dispersion fits for the deflectors from the lens system J0147+4630 and B0445+123. The plot for each system consists of three panels. Top panel - the extracted and smoothed 1D spectrum of the deflector is plotted over the observed wavelength where the smoothing has been done using a boxcar filter of size around 2.5 Å. Prominent stellar and telluric absorption lines are marked if present. And the measured redshift of the deflector is mentioned in the lower right corner of the plot. Middle panel - the pPXF generated model fit (red) to measure the velocity dispersion is plotted on top of the original unsmoothed spectrum (black). A smoothed version (yellow) of the original spectrum is also presented to show the goodness of the fit. The grey parts are the masked or excluded regions from the fit. Bottom panel - the green dots show the residuals between the unsmoothed flux and the model fit for each wavelength normalized to the respective model fits. 21

2.4 1D spectra and velocity dispersion fits for the deflectors from the lens system B0631+519, J0659+1629 and J0818-2613. The description of the figure is same as Figure 2.3. 22

2.5 1D spectra and velocity dispersion fits for the deflectors from the lens system J0924+0219, J1433+6007 and J1817+2729. The description of the figure is same as Figure 2.3. 23

2.6 Illustration showing relations among the velocity dispersion measurements of the deflectors. The scatter plots between each pair of deflectors show corresponding velocity dispersion measurements for three hundred setups where each marker shows the measurements from the same setup. The blue-shaded curves are the individual velocity dispersion distributions of the deflectors. The set-ups were varied by changing the wavelength ranges, set of the spectra of the templates, and degree of the additive polynomial. In general, the covariance terms are negligible except in a few cases, for which they should be taken into account. The lens system J0659+1629 has been excluded from this analysis as the extracted deflector spectrum for this system only covers a small wavelength range. The plot in the upper-right shows a heat-map of the covariance matrix calculated from these velocity dispersion measurements, where the measurements were normalized to their respective mean. 32

3.1 Distribution of MUSE sample properties. Left: Distribution of galaxies in the (σ, z) plane. The redshifts and integrated velocity dispersion, σ, were measured using the corresponding central spectra of the galaxies. Individual central spectrum was created by co-adding all the spectra from spaxels within approximately one effective radius, R_e. Right: Distribution of galaxies in the plane of the spatial extension of the extracted resolved stellar kinematics data in units of R_e^{maj}, and number of Voronoi bins with a target SNR 12. R_e^{maj} is the semi-major axis of the elliptical half-light isophote of the galaxy. The number of bins and the associated histogram are plotted in a log scale and the color map shows the galaxy redshifts. 38

3.2 Example of kinematics extraction from galaxies at different redshifts. The galaxies are A370_8644 (z = 0.371, top), MACS1149_62 (z = 0.551, middle) and COSMOSGR35_1101259 (z = 0.747, bottom). In each case, two extracted spectra (blue) from two different Voronoi bins, one close to the galaxy center and the other close to the edge, are shown with kinematic fitting from PPXF (red). The green markers are residuals between data and the fitted model at each wavelength and the gray regions mark the excluded wavelength range from fitting. Additionally, for each galaxy, the HST image, 2D map of the Voronoi binning of the spaxels at target SNR 12, and extracted velocity (median subtracted) and velocity dispersion maps are also depicted. The green circle in each HST image shows the extension of the extracted kinematic data relative to the observed surface brightness. 40

3.3 SPS fitting from PPXF. Top: Fitting was done using FSPS templates. Bottom: Fitting was performed using GaLAXEV templates. In both cases, the blue curve shows the observed galaxy spectrum from A370_8644 (z=0.371), the red curve is the best-fitting model (stellar continuum + gas) from PPXF, the orange curve is the best-fitting gas-only spectrum, and the green diamonds are the residuals. The grey-shaded regions were masked and excluded from fitting. 49

3.4 2D distribution in (λ_R, ϵ). λ_R was measured using equation 1 and and ϵ is the observed ellipticity derived from MGE models. The circle and square markers correspond to visually classified (using V map) regular and non-regular rotators. The solid green line is the predicted theoretical relation for an edge-on ($i = 90°$) isotropic rotator (Cappellari, 2016, equation 14) and the dashed green line represents one-third of that (Emsellem et al. (2007) used this line to differentiate between regular and non-regular rotators). The magenta line shows a theoretical upper limit on global anisotropy, $\beta = 0.7\epsilon_{\rm ins}$, provided the intrinsic shape of the galaxy from an edge-on view (Cappellari, 2016, equation 11), and the grey dotted lines show how the magenta line changes with different inclinations ($\Delta i = 10°$), while the grey dashed lines show how the galaxies move across the diagram with changing inclination, ($\Delta i = 10°$), and for a set of given intrinsic ellipticity values ($\Delta\epsilon_{\rm ins} = 0.1$). The black solid lines defined by $\lambda_{R_e} < 0.08 + \varepsilon/4$ and $\varepsilon < 0.4$ (Cappellari, 2016, equation 19) separates non-regular rotators from regular rotators. Left Panel: The red and blue colors denote non-regular and regular rotators respectively, and in general confirm our visual classification. Right Panel: The galaxies are plotted in (ϵ, λ_R) plane with their integrated velocity dispersion indicated by the color map. 53

3.5 Misalignment between kinematic and photometric PAs as a function of ϵ. PAs of the photometric major axis, $PA_{\rm phot}$, were measured using the sky-subtracted HST images, and PAs of the kinematic major axis, $PA_{\rm kin}$ were measured from the observed velocity maps. The blue circles denote visually identified regular rotators and the red squares show the non-regular rotators. The plot is symmetrized about the black solid line along 0° to eliminate any indication of bias towards positive or negative misalignments. The dashed lines show ±10°, 30° misalignments. Similar to local Universe (see Fig. 6 in Cappellari, 2016), most of the fast rotators in MUSE sample also show < 10° misalignment between $PA_{\rm phot}$ and $PA_{\rm kin}$. 54

3.6 Age, metallicity and (M_*/L) estimates from SPS models in the mass-size plane. Distributions of luminosity-weighted and LOESS-smoothed age (left panel), metallicity, [Z/H] (middle panel), and stellar mass-to-light ratio, (M_*/L) (right panel) on the mass–size plane (lg R_e^{maj} vs lg M_*). The galaxy semi-major axis within half-light elliptical isophote, R_e^{maj} was measured from MGE models (see section 3.4.1), and stellar mass, M_* was measured by multiplying estimated M_*/L with total luminosity (see section 3.4.3.3). The top panel shows results from SPS analysis with FSPS templates and the bottom with GALAXEV templates. In each panel, the gray dashed lines indicate the lines of constant σ_e for 100, 150, 200, 250, 300 and 350 kms^{-1} from left to right and the black dotted lines are for constant surface mass density, $\Sigma_e = 10^8, 10^9, 10^{10}, 10^{11}$ M$_\odot$ kpc^{-2} from top to bottom. A kernel density estimate of the galaxy number density is also indicated by the grey contour lines. 56

3.7 Age and metallicity from different SPS models with σ_e. The top panel shows the distribution of luminosity-weighted and LOESS-smoothed age on the (σ_e, [Z/H]) plane, and the bottom panel shows the distribution of the luminosity-weighted and LOESS-smoothed global metallicity, [Z/H] on the (σ_e, age) plane, from SPS analysis with two different template sets. In both rows, the left column shows results from fitting with FSPS templates and the right from GALAXEV templates. In each plot, a kernel density estimation of the galaxy number density is indicated by the grey contours. 57

3.8 Comparing LOESS-smoothed stellar mass, M_* (right panel) and mass-to-light ratio, M_*/L (left panel) from two different SPS models with color-coded velocity dispersion, σ_e. In both plots, the black line denotes the best-fit line and the red dotted lines show the selection region of galaxies for fitting. The coefficients of the best-fit lines were measured using the LtsFit python package (Cappellari et al., 2013b). The red line shows the one-to-one relation between the measurements from different SPS models. A kernel density estimate of the galaxy number density is also indicated by the grey contour lines. In the case of M_*/L, the one-to-one line deviates significantly from the best-fit line. We have to shift the estimates from the Galaxev model, both M_* and M_*/L, by 0.2 dex to bring them close to the one-to-one relation. As expected, both M_* and M_*/L estimates from each model increase with σ_e. 58

4.1 The number density histograms of the statistically matched MaNGA ETG sample (dashed line) and MUSE sample (solid line). Left: Histograms for stellar mass, log M_*. For both samples, the stellar mass was measured from SPS fitting using pPXF with templates from the FSPS model (check section 3.4.3.3 and 4.3.2). A mass cut of log $M_*(M_\odot) \geq 10.65$ was applied to the original MaNGA ETG sample. Right: Histograms for integrated velocity dispersion, σ. The p-values of the corresponding K-S tests are shown in the title of the respective plots. 66

4.2 An example of a 2D Sérsic model fitting to the HST image of a galaxy. Left triangular panel: A corner plot showing the probability distributions and associated pairwise covariances of the seven free parameters of the fitted 2D Sérsic model using a Bayesian MCMC method. The fit was performed to the HST image of the galaxy COSMOSGR32_1158312 (z=0.725). The median of the chain for each parameter with the 1 σ uncertainty, measured using the 16th and 84th percentile values, was shown on top of each probability distribution plot. Middle top panel: Comparison of the 1D radial profile of the surface brightness created from the best-fit Sérsic model (blue) with the 1D radial profile from data of the galaxy (red). Right top panel: The top plot shows the HST image of the galaxy and the edge of the adopted elliptical mask (green solid line), the middle plot is the synthetic image created from the best-fitting 2D Sérsic model and the bottom plot shows the noise-weighted residuals. 69

4.3 λ_R values of the MUSE sample before and after applying the PSF correction. The circles represent the observed λ_R and the diamonds represent the PSF corrected or intrinsic values. The dashed line connects a galaxy's observed and intrinsic λ_R. The galaxies for which a PSF correction was not applicable, kept to their original observed values. A correction was not applied to a galaxy if the Sérsic index, n, was beyond the range of $0.5 < n < 6.5$ or $R_e^{maj} < \sigma_{PSF}$ or corrected $\lambda_R = \frac{\mathrm{R|V|}}{\mathrm{R}\sqrt{\mathrm{V}^2+\sigma^2}} > 1$, as in these cases the correction is not reliable. 71

4.4 Comparison of the running medians in the observed and intrinsic λ_R and $\lambda_R/\sqrt{\epsilon}$ values of the MUSE sample. In each plot, we only show the observed (marked by circles) and intrinsic (marked by diamonds) values of the 81 galaxies that were PSF-corrected. The observed and corrected values are sorted according to their velocity dispersion or stellar mass and allocated in bins with equal numbers of galaxies. The square boxes represent the medians in the bins and the uncertainty of the medians in each bin was estimated using a bootstrap resampling method. Left panel: The top plot shows the running medians of the observed λ_R (black line) which were not PSF corrected and intrinsic or PSF corrected (red line), and the bottom plot shows the running medians for $\lambda_R/\sqrt{\epsilon}$. In these two plots, the galaxies were sorted according to their velocity dispersion σ. Right panel: Same as left panel, but this time the galaxies were sorted according to their stellar mass, M_* . 72

4.5 PSF-corrected λ_R in the M_* - σ_e plane. Left: This plot shows the intrinsic λ_R of 81 MUSE galaxies to which PSF correction was applied. Right: Intrinsic λ_{R_e} of the matched MaNGA sample containing 746 ETG galaxies. In both plots, the black dashed lines divide the corresponding sample into four parts where the top-right part is dominated by galaxies with high M_* and σ_e but lower λ_R. Contrarily, the bottom-left part is dominated by galaxies with low M_* and σ_e but higher λ_R. The first group represents mostly non-regular rotators and the second group represents regular rotators. 73

4.6 Evidence of increased rotational support in high-redshift galaxies. In each plot, the diamond markers point to the PSF-corrected values of the MUSE galaxies. The corresponding PSF-corrected values from MaNGA galaxies are shown as a kernel density estimate (KDE) of the galaxy number density using grey contour lines. The red squares denote the running medians from the PSF-corrected values of MUSE galaxies and the blue squares are for similar quantities from MaNGA galaxies. Each set of medians and uncertainties was measured in the bins of an equal number of galaxies sorted by their velocity dispersion or stellar mass. Left panel: The top plot shows the running medians of the intrinsic λ_R and the bottom plot shows the running medians for $\lambda_R/\sqrt{\epsilon}$. In these two plots, the galaxies were sorted according to their velocity dispersion σ. Right panel: Same as left panel, but this time the galaxies were sorted according to their stellar mass, M_*. 75

4.7 Comparison of estimates of effective radius and ellipticity from MGE and Sérsic fits. Left: Comparison between semi-major axis within elliptical half-light isophote, $R_{e,maj}^{MGE}$ and effective radius, R_e^{sersic}. The black line is the one-to-one line, the red line denotes the best-fit line and the red dashed and red dotted lines show 1σ and 3.5σ intrinsic scatter. The coefficients of the best-fit lines and intrinsic scatters were measured using the LtsFit python package (Cappellari et al., 2013b). Right: Comparison of ellipticities. The description of lines are same as the left plot. The one-to-one line in the left plot shows that the size estimates from the Sérsic fitting are usually higher than the ones from the MGE method. However, for ellipticity measurements, there is no such obvious bias. 77

4.8 Comparison of Sérsic index estimates from 2D Sérsic fitting with elliptical and square aperture. The black line denotes the one-to-one line, the red line is the best-fit line and the red dashed and red dotted lines show 1σ and 3.5σ intrinsic scatter. The coefficients of the best-fit lines and intrinsic scatters were measured using the LtsFit python package (Cappellari et al., 2013b). The one-to-one line shows that, in general, the Sérsic index measured using an elliptical aperture is higher than the square aperture. A square aperture by including more background light and thus flattening the galaxy's light profile, may lead to a lower Sérsic index value. 79

4.9 Comapring measured λ_R of MUSE galaxies from different aperture sizes. Left: Comparison between an elliptical aperture with a semi-major axis of 2 R_e^{maj} and a circular aperture of radius 2 R_e. The red is the best-fit line and the red dotted line shows the 3.5σ intrinsic scatter. The black line is the one-to-one line. Right: Comparison between elliptical apertures with semi-major axes of 2 R_e^{maj} and 1 R_e^{maj}. The description of the lines is the same as the left plot. The one-to-one line is closer to the best-fit line when the λ_R value is small in both cases. The intrinsic scatter and deviation of the one-to-one line from the best-fit line are more significant in the right plot as in this case, the aperture sizes are significantly different. However, aperture size does not affect the galaxies with $\lambda_R < 0.1$, which are predominantly rounder and kinematically classified as non-regular rotators. . 79

4.10 Comparing PSF-corrected λ_R and $\lambda_R/\sqrt{\epsilon}$ of the MUSE sample from different apertures with MaNGA galaxies. Left: Running medians from three sets of PSF-corrected λ_R values of MUSE galaxies from three different sizes of apertures, an elliptical aperture with a semi-major axis of 2 R_e^{maj} (red squares with dotted line), a circular aperture of radius 2 R_e (green circles with dashed line), and an elliptical aperture with a semi-major axis of 1 R_e^{maj} (black diamonds with dashed-dot line), are plotted along with the ones from the MaNGA sample (blue squares with solid line). Each set of markers represents the medians in the bins of galaxies sorted by their stellar mass and the lines display the decreasing trends in medians with increased mass. A kernel density estimate of the number density of MaNGA galaxies is shown using grey contour lines. Except in a few cases, in each bin, the running medians were within statistical uncertainties of one another. The effect of aperture size is prominent in bins of low-mass galaxies ($M_* < 11.3$), however, almost disappears in the bins of high-mass galaxies ($M_* > 11.3$). Right: Running medians from three sets of PSF-corrected $\lambda_R/\sqrt{\epsilon}$ values of MUSE galaxies along with the MaNGA sample. The description of different markers and lines remains the same as the left plot. We see a similar pattern as the left, however, the overall difference between medians has decreased. 82

5.1 Example of MGE fits to HST images of the MUSE galaxies at different redshift. The first and third columns show the HST image and the second and fourth columns show the corresponding MGE model contours (red curves) with observed surface brightness contours (black curves). The galaxy ID and redshifts are marked on the left side of the respective galaxy's HST image. The galaxies were selected randomly from different redshift bins. 91

5.2 Example of galaxies with different qualities of JAM fit (Qual=3, 2, 1, and 0). Each row represents a galaxy and for each galaxy, the HST image, observed and recovered V and V_{rms} fields are presented. The black curves show the observed and modeled surface brightness contours in respective kinematic maps. Both the observed and modeled kinematic maps are rotated such that the major axis of a galaxy aligns with the image's x-axis. Note that the quality of fit decreases from Qual=3 to Qual=0. 97

5.3 Example of corner plots for galaxy A370_8644. Each plot represents a JAM model with one of the four mass profiles (MFL, power law, NFW, and gNFW) and the spherical orientation of the velocity ellipsoid. The black-dashed lines show the 16th, 50th, and 84th percentiles of each posterior distribution. Additionally, the observed and modeled V_{rms}, using the median parameter set of the corresponding model, is also displayed on the right side of the individual corner plot. 98

5.4 Comparison of measured $\overline{\gamma}$ values between the JAM_{cyl} and JAM_{sph} models with three different mass profiles. Left: comparison between JAM models with power-law mass profile, Middle: comparison between JAM models with NFW profile, and Right: comparison between gNFW models with different orientations. In each plot, the black line denotes the one-to-one line, the red solid line represents the best-fit line, while the red dashed and red dotted lines indicate the 1σ and 3σ intrinsic scatter, respectively. The coefficients of the best-fit lines and intrinsic scatters were measured using the LtsFit python package (Cappellari et al., 2013b). In all three cases the one-to-one line shows that the JAM models with spherical velocity ellipsoid orientations tend to yield higher estimates of the total density slope than their cylindrical counterparts with the same mass profile. This discrepancy is more pronounced in the power-law models than in the NFW and gNFW models. The MFL model was excluded because, in this case, the total density slopes are uniquely determined by their luminosity density slopes and do not vary with JAM models. 101

5.5 Comparison of measured $\overline{\gamma}$ values from three different JAM_{cyl} models. Left: comparison between JAM_{cyl} + MFL model and JAM_{cyl} + power law model, Middle: comparison between JAM_{cyl} + gNFW model and JAM_{cyl} + power law model, and Right: comparison between JAM_{cyl} + gNFW and JAM_{cyl} + NFW model. The description of the plots is the same as Fig. 5.4. The measurements from the NFW and gNFW models are mostly consistent with each other with observed RMS scatter of 0.01. However, the power-law model shows more deviation from the other two mass profiles and tends to overestimate the $\overline{\gamma}$ values compared to both the NFW and gNFW models. 103

5.6 Comparison of measured $\overline{\gamma}$ quantities from three different JAM_{sph} models. Left: comparison between JAM_{sph} + MFL model and JAM_{sph} + power law model, Middle: comparison between JAM_{sph} + gNFW model and JAM_{sph} + power law model, and Right: comparison between JAM_{sph} + gNFW and JAM_{sph} + NFW model. Similar to the cylindrical case, the tightest correlation is observed between the NFW and gNFW models, and the power-law model shows more deviation from the other two mass profiles and tends to overestimate the $\overline{\gamma}$ values compared to both the NFW and gNFW models. The description of the plots is the same as Fig. 5.4. 103

5.7 Observed linear correlation between the total density slope, $\overline{\gamma}$ and other galaxy properties: central velocity dispersion, σ_e, effective radius, R_e, total mass, M_{tot}, stellar mass, M_* and stellar surface mass density Σ. The best-fitting parameters, corresponding errors, and Pearson coefficients with p-values were measured using the LtsFit package. In each plot, the black solid line represents the best-fit line and the black dashed lines are 1σ observed intrinsic scatter from the best-fit while the outliers were clipped at 3σ level. The resulting Pearson correlation coefficients from the fits and corresponding p-values are printed at the top of each plot. The stellar surface mass density and dynamical total mass were measured in this Chapter while other properties were defined in Chapter 3. Among the five galaxy parameters, only R_e and Σ show significant correlation with $\overline{\gamma}$. 105

5.8 Graphical representation of the best-fit lines from the six JAM models listed in Table 5.2. For each model, the solid line shows the best-fit line obtained from fitting conducted using all of 108 galaxies and the dashed line is using galaxies with only Qual=2, 3. The slopes from Qual=2,3 galaxies in all six cases are negative and suggest that the total density slopes have become steeper with cosmic time. However, the slopes from all galaxies with either NFW or gNFW mass models are relatively less negative than ones with high-fit-quality galaxies. The slopes from power-law models with all galaxies are slightly positive. However, the slopes derived fitting all galaxies are within the 1σ uncertainty of each other and thus statistically indistinguishable. 108

5.9 The evolution of the total density slope, $\overline{\gamma}$, as a function of redshift is depicted in two plots. The top plot shows $\overline{\gamma}$ values measured using the $\mathrm{JAM_{cyl}}$ + gNFW model, while the bottom plot uses the $\mathrm{JAM_{sph}}$ + gNFW model. In each plot, galaxies are marked based on their JAM modeling quality: green diamonds for Qual 3, black squares for Qual 2, and blue circles for Qual 1, each with associated error bars. The red solid line represents the best-fit line using $\overline{\gamma}$ values from all galaxies, whereas the blue solid line represents the best-fit line using only Qual 3 and 2 galaxies. The dashed and dotted lines indicate the 1σ and 3σ intrinsic scatter, respectively. The coefficients of the best-fit lines and intrinsic scatters were measured using the LtsFit Python package (Cappellari et al., 2013b). The shaded region shows the uncertainty associated with the best-fit line. For both models, the slope derived from high-fit-quality galaxies alone is more negative than the slope from all galaxies. However, in both cases, the best-fit lines and associated slopes are within the uncertainty of each other. The near-zero slope of the best-fit line from all galaxies suggests no significant evolution over cosmic time. Conversely, the negative slope from the best-fit line with high-fit-quality galaxies suggests that the total density slope of ETGs has become steeper at lower redshifts, corroborating findings from some lensing studies. 109

5.10 Comparison of the measured total density slope, $\overline{\gamma}$ for the overlapping galaxies from the MUSE sample (blue circles) and Frontier Field sample (red square)(Derkenne et al., 2021). The overlapping galaxies, in total 18, were identified by matching the galaxy IDs, coordinates, redshifts, and central velocity dispersions. For the MUSE sample, the measurements from the $\mathrm{JAM_{cyl}}$ + gNFW model were used as the comparison set was coming from a similar model. Although there are some differences in the underlying model assumptions and analysis processes between the two studies, in most cases, the measurements are within the 1σ uncertainty of each other. 110

5.11 The number density histograms of the statistically matched Frontier Field (dashed line) and MUSE sample (solid line). From left to right the histograms for effective radius, R_e, total stellar mass, M_{tot}, and surface mass density Σ of the two samples are shown. The p-values of the corresponding K-S tests are shown as the title of the respective plots. 110

5.12 Total density slope,$\overline{\gamma}$ as a function of redshift from different dynamical and lensing studies. The measured $\overline{\gamma}$ using dynamical modeling techniques are plotted with non-grey colors - the MUSE values are shown as blue circles and the Frontier Field quantities (Derkenne et al., 2021) as red squares. Total density slopes measured using gravitational lensing techniques (Auger et al., 2010; Sonnenfeld et al., 2013; Li et al., 2018) are presented using different grey markers. The 1σ uncertainties on each estimated $\overline{\gamma}$ are also plotted using associated colors. The red, grey, and blue solid lines show the best-fit lines from the combined dynamics sample (MUSE + Frontier Field), combined lens sample (SLACS + SL2S + BELLS & BELLS Gallery), and combined lens + dynamics sample respectively and the associated shaded region in the same color are 1 σ confidence interval estimated through a bootstrap sampling method. Though the dynamics and lens sample vary in mass and size, their surface mass density distributions, which is the most correlated galaxy parameter to $\overline{\gamma}$, originate from the same underlying population (a two-sample K-S test yields a p-value of 0.11 rejecting the null hypothesis that the underlying surface mass density distribution is different). 112

5.13 The number density histograms of the combined dynamics (dashed line) and lens sample (solid line). From left to right the histograms for velocity dispersion, σ_e, effective radius, R_e, and surface mass density Σ of the two samples are shown. The p-values of the corresponding K-S tests are shown as the title of the respective plots. Though the two samples do not match in mass and size they statistically match over Σ. 114

List of Tables

2.1 Summary of spectroscopic observation of the lens systems for which redshifts and stellar velocity dispersions of the deflectors have been reported in this paper. Position angle (PA) of the slits was measured from North to East direction. The seeing conditions (FWHM) were estimated using the data from the corresponding nights. 16

2.2 Measured redshifts of the deflectors with associated uncertainties using the extracted 1D spectra. Previously known values, if any also given with corresponding references. 25

2.3 Measured S/N per angstrom of the extracted deflector spectra and single aperture velocity dispersion with associated statistical and systematic uncertainties. As a sanity check, SIS velocity dispersions are presented to compare with the measured velocity dispersions. The quasar redshifts and Einstein radii reported here have been used to calculate the SIS velocity dispersions. Note that, for B0445+123 and B0631+519, the source redshift is unknown. Thus a possible range of source redshift has been assumed to calculate the corresponding SIS velocity dispersion range. 28

3.1 Information related to the data cubes used in this work such as ESO archive ID, program ID, effective exposure, galaxy cluster or field within the cube, and number of galaxies collected from the cube are listed in the table. 41

3.2 Information about archival HST images and the catalogs used in this work. All images are available at the Mikulski Archive for Space Telescopes (MAST). The catalogs were used to identify galaxies in the MUSE IFU white and HST images. 42

3.3 This table presents the galaxy ID, coordinates, redshift, and other measured kinematic, structural, and stellar population properties for a subset of MUSE galaxies. 52

5.1 The eight models with the parameters and parameter boundaries. $\mathrm{JAM_{cyl}}$ denotes a dynamical model with the cylindrical alignment of the velocity ellipsoid and $\mathrm{JAM_{sph}}$ is for spherical orientation. The anisotropy parameter for a $\mathrm{JAM_{cyl}}$ or a $\mathrm{JAM_{sph}}$ model is σ_z/σ_R or σ_θ/σ_r respectively. q'_{min} is the minimum observed axial ratio and $\mathcal{R}(q)$ is the empirical lower limit of the velocity dispersion ratio. 95

5.2 The coefficients of the best-fit lines to the measured total density slopes ($\overline{\gamma}$) using different JAM models. Each measured set of $\overline{\gamma}$ values was fitted using the relation $\overline{\gamma} = a + b_0(z - z_0)$, where z_0 is the median of the z values and Δ is the RMS deviation between the data and the fitted relation. The fitting was conducted either using galaxies of Qual=3, 2, 1 or only with Qual=3,2. The observed RMS scatters of the fits are also listed in the table. For a graphical representation of all best-fit lines see Fig. 5.8. 107

5.3 The coefficients of the best-fit lines to the measured total density slopes ($\overline{\gamma}$) using different dynamical and lensing studies. 111

Abstract of the Dissertation

A Study of Galaxy Evolution and Cosmology using Early-type Galaxies at Intermediate Redshift

In this dissertation, I used early-type galaxies (ETGs) at intermediate redshifts ($0.25 < z < 0.75$) to study both galaxy evolution and cosmology. I assembled a novel sample of 180 galaxies with integral field unit (IFU) data within this redshift range. Utilizing the extracted kinematic maps and photometric data, I measured the structural, kinematic, and stellar population properties of these galaxies. By comparing this sample with a subset of ETGs from the MaNGA survey, I demonstrated that the degree of rotational support in ETGs has decreased at lower redshifts. Furthermore, I investigated the discrepancies between observational results from lensing studies and predictions from cosmological simulations concerning the evolution of the total density slope of ETGs, which present conflicting views. Using Jeans anisotropic modeling, I modeled the observed resolved kinematics and measured the total density slope of this sample. My findings suggest that the slope in the $\gamma - z$ plane is generally negative, indicating an increase in the total density slope with decreasing redshift. However, due to the high level of uncertainty, I cannot conclusively dismiss the possibility of a zero or positive slope. In addition to studying these non-lensing ETGs, I also worked with ETGs which act as strong gravitational lenses, to measure the Hubble constant using the time-delay cosmography method. A crucial factor in accurately measuring the Hubble constant is the stellar kinematics of the lensing galaxies, which is challenging to measure due to the spatial blending of light caused by atmospheric seeing in ground-based telescopes. To address this, I developed a forward modeling method to extract high signal-to-noise ratio (SNR) one-dimensional spectra, enabling reliable kinematic measurements. The results presented in this dissertation contribute to our understanding of galaxy evolution and provide insights that could help resolve the Hubble tension, i.e., the discrepancy between independent inferences of the current expansion rate of the Universe. By improving our knowledge of ETG properties across redshifts and refining methods to measure the Hubble constant, this work advances our comprehension of the fundamental processes governing the Universe.

Acknowledgments

I would like to express my deepest gratitude to those who have supported me throughout this journey. To my parents, Mita and Tushar, who dedicated their lives to my well-being and education, thank you for your unwavering love and sacrifice. To my wife, Arni, your loving support has been invaluable, and to my daughter, Devnandini, who has been a source of unbounded happiness and joy for the past year and a half, thank you for being the driving force that inspired me to complete this work.

I am profoundly thankful to my adviser, Chris, for your guidance, kindness, patience, thoughtfulness, and wisdom. Your mentorship has been instrumental in shaping this dissertation. I also extend my heartfelt thanks to my collaborator, Michele, whose continued guidance has enabled me to accomplish a significant portion of this work.

Chapter 1

Introduction

Early-type galaxies (ETGs), which include elliptical (E) and lenticular (S0) galaxies, are characterized by their smooth light profiles, lack of star formation, deficiency of gas or dust and predominance of old stellar populations. These galaxies offer crucial insights into galaxy evolution due to their complex kinematics and mass distribution (Cappellari, 2016). In addition, ETGs play a critical function in cosmology through strong gravitational lensing. In this chapter, I describe how ETGs could be utilized to answer open questions in astrophysics and cosmology.

1.1 ETGs to probe galaxy evolution

Galaxies in our Universe can be broadly classified into two main categories based on their morphological features—spiral galaxies (S) and elliptical galaxies (E). This classification scheme then extends further based on the morphology of the spiral arms (Sa-Sd), the presence of a central stellar bar (SBa-SBd), and how spheroidal elliptical galaxies are (E0-E7). Some galaxies are morphologically irregular (Irr) and some exhibit features similar to both spiral and elliptical galaxies (S0). The E and S type galaxies are also respectively known as "early" and "late"-type galaxies.

The advent of integral-field unit (IFU) spectrographs has significantly advanced our understanding of early-type galaxies (ETGs) in the local Universe. IFU datacubes provide detailed 2D maps of galaxy velocity and velocity dispersion fields, which enable the classification of ETGs into regular and non-regular rotators (Cappellari, 2016). Regular rotators exhibit organized rotation and disk-like structures, while non-regular rotators display more complex dynamics (Emsellem et al., 2007). Studies using IFU data from surveys such as SAURON (de Zeeuw et al., 2002), ATLAS3D (Cappellari et al., 2011), and CALIFA (Sánchez et al., 2012) have shown that even fast rotators in

local ETGs have significant dispersion support (Emsellem et al., 2011). This raises the question of whether ETGs at intermediate redshift ($0.1 < z < 1$) exhibit similar kinematic characteristics or are more rotation-supported.

Moreover, IFU data have enabled detailed dynamical modeling of local ETGs using techniques such as Jeans Anisotropic Models (JAM) (Jeans, 1922) and Schwarzschild orbit superposition methods (Schwarzschild, 1979). These methods determine the mass distribution within galaxies by modeling the observed kinematics (e.g. Cappellari, 2008). Research has indicated that the slope of the mass density profile ($\rho(r) \propto r^{-\gamma}$) in local ETGs is approximately γ =2, where the parameter γ quantifies the radial variation in mass distribution (e.g. Cappellari et al., 2015; Poci et al., 2017; Bellstedt et al., 2018; Li et al., 2019). This suggests that local ETGs generally exhibit a balance between luminous and dark matter. Investigating whether this mass distribution remains consistent over cosmic time, and if not, then how the total density slope evolves with redshift, is crucial.

In this dissertation, I address these questions by analyzing the resolved stellar kinematics of a statistically significant sample of ETGs at intermediate redshift.

1.1.1 Evolution of rotational support in ETGs

The dominant mode of stellar motion in a galaxy–whether it be ordered rotation or random motion–plays a crucial role in shaping its dynamics and mass distribution, offering insights into its formation and evolution. Massive galaxies at high redshift ($z \sim 2$) have shown substantial rotational support (e.g. van Dokkum et al., 2015; Wisnioski et al., 2015; Belli et al., 2017). Conversely, local ETGs, even the 'fast-rotator' galaxies display significant dispersion support (e.g. Emsellem et al., 2007, 2011). This contrast implies a major shift in rotational support over cosmic time. To address this, earlier research has compared the rotational dynamics of ETGs across both the local and distant Universe (e.g. Belli et al., 2017; Bezanson et al., 2018). Using disky quiescent galaxies at $1 < z < 2.5$, as defined by their Sérsic indices, Belli et al. (2017) observed that the characteristic V/σ ratio decreases from 3 to 1.5 at $z = 0$. Similarly, Bezanson et al. (2018) investigated this evolution by comparing the V/σ ratio in 104 quiescent galaxies ($0.6 < z < 1.0$) from the Large Early Galaxy Astrophysics Census (LEGA-C) spectroscopic survey (van der Wel et al., 2016) to a sample of 91 low-redshift ETGs ($0.005 < z < 0.03$) from the Calar Alto Legacy Integral Field Area (CALIFA) survey (Sánchez et al., 2012). They found that at fixed velocity dispersion, the higher-redshift galaxies on average exhibit 94 ± 22% higher rotational support than their

local counterparts. However, constrained by the absence of IFU data, these studies relied on slit spectroscopy to measure the velocity and velocity dispersion profiles. In this work, I revisit this question using a substantial sample of intermediate-redshift ETGs with high-quality IFU data. This dataset ensures direct comparability with the local ETGs, which typically have their kinematics derived from IFU measurements.

To measure the degree of rotational support in an ETG, I have used a luminosity-weighted quantity λ_R (Emsellem et al., 2007), an approximation to galaxy angular momentum, defined as

$$\lambda_R = \frac{\langle R|V|\rangle}{\left\langle R\sqrt{V^2+\sigma^2}\right\rangle} = \frac{\sum_{i=0}^{N} F_i R_i \,|V_i|}{\sum_{i=0}^{N} F_i R_i \sqrt{V_i^2+\sigma_i^2}}, \tag{1.1}$$

where V_i is the LOS stellar velocity, σ_i is the velocity dispersion, R_i is the distance from the galaxy center, and F_i is the total flux of a spaxel within the adopted aperture. By comparing λ_R at the population level for samples of low and high-z ETGs, I have qualitatively measured the extent to which rotational support has evolved over cosmic time.

1.1.2 Evolution of total density slope

Galaxies generally exhibit a mass distribution where baryonic matter, such as stars and gas, is concentrated in the inner regions, and dark matter dominates the outer regions. This distribution is often described by a power-law density profile, $\rho(r) \propto r^{-\gamma}$, where γ represents the total density slope, reflecting how rapidly the mass density (ρ) declines with radius (r). Understanding the evolution of γ is essential for studying galaxy evolution, as it provides insights into how key processes such as mergers, gas accretion, and feedback mechanisms have influenced the structure and dynamics of galaxies over cosmic time. In the $\gamma - z$ plane, a negative slope indicates that the density profile becomes steeper as redshift decreases. This suggests that the mass distribution becomes more concentrated in the later stages of galaxy evolution, often due to processes like wet mergers, which enhance central mass concentration, and increased star formation (Barnes & Hernquist, 1991; Mihos & Hernquist, 1994). Conversely, a zero slope implies little change in the density profile over time. A positive slope suggests a flattening of the profile, potentially resulting from dry mergers, which contribute to a more diffuse mass distribution by merging gas-poor galaxies, or from the cessation of star formation (Hilz et al., 2013). Early-type galaxies (ETGs) are particularly advantageous for this analysis due to their stable structures.

At intermediate redshifts, measuring the total density slopes of ETGs involves a combination of observational techniques and theoretical models. On the observational side, a significant contribution comes from the gravitational lensing method, which measures γ of the lensing galaxy, by analyzing the distortion of background objects caused by its mass distribution. Studies using lensing surveys, such as the Lenses Structures and Dynamics (LSD) survey, Sloan Lens ACS Survey (SLACS), Strong Lenses in the Legacy Survey (SL2S), and BOSS Emission-Line Lens Survey (BELLS), which combined cover a redshift range of $0.1 < z < 0.8$, have found that the density profiles of ETGs are often shallower at the earlier epochs compared to later times. (Gavazzi et al., 2007; Auger et al., 2010; Lagattuta et al., 2010; Ruff et al., 2011; Bolton et al., 2012; Sonnenfeld et al., 2013; Li et al., 2018; Tran et al., 2024). For example, using the SL2S sample, Sonnenfeld et al. (2013) found that $\mathrm{d}\gamma/\mathrm{d}z = -0.10 \pm 0.12$, after accounting for dependencies of γ on other galaxy parameters.

Cosmological simulations offer a theoretical perspective by modeling galaxy formation and evolution across cosmic time. Simulations like IllustrisTNG (Pillepich et al., 2018) and Magneticum (Dolag, 2015) provide predictions about how the total density slope evolves with redshift. For instance, IllustrisTNG suggests a minimal change in the density slope below ($z \sim 1$) (Wang et al., 2019), while Magneticum simulations show a decrease from approximately $\gamma \sim 2.3$ at $z = 1$ to $\gamma \sim 2.0$ at $z = 0$ (Remus et al., 2017). These findings depict a different picture from the lensing studies.

Another way to measure γ is by using dynamical modeling techniques, which involve analyzing the kinematics of galaxies to infer their mass distribution. While dynamical modeling can provide detailed insights into the total density slope, the current studies at intermediate redshift cover a limited redshift range, restricting their ability to study the evolution of the density slope in the $(\gamma - z)$ plane effectively (Derkenne et al., 2021, 2023).

Motivated by the contradictory picture about the evolution of γ at intermediate redshifts from lensing studies and cosmological simulations, in this work, I measured the total density slope of a sample of galaxies over a redshift range of $0.25 < z < 0.75$ using Jeans anisotropic modeling. This dynamical modeling method has been extensively used in several studies both in local and intermediate redshift (e.g. Derkenne et al., 2021, 2023; Zhu et al., 2023). I extended this dynamical modeling technique up to z = 0.75 for the first time and provided a complementary perspective to gravitational lensing findings (see Chapter 5 for relevant theoretical background and results).

1.2 ETGs to resolve the Hubble tension

In addition to their fundamental role in understanding galaxy evolution, early-type galaxies (ETGs) can also help address unresolved questions in cosmology. One such issue is the statistically significant 5σ discrepancy between the measured and inferred values of the current expansion rate of the Universe, known as the Hubble tension. Here I describe how the stellar kinematics of both lens and non-lens ETGs are utilized to precisely measure the Hubble constant and potentially resolve this tension.

1.2.1 Theoretical background

Our Universe is expanding and distant galaxies are receding from each other. In the 1920s, Edwin Hubble provided the first empirical evidence for this expansion through observation and measured the rate of this expansion, the so-called Hubble constant (H_0). This parameter is crucial as it quantifies the current rate of the Universe's expansion and serves as a foundation for estimating its age and size. One can utilize different cosmological phenomena that happened at the various epochs of the Universe's history to measure H_0. Using cosmic microwave background (CMB) radiation, which is a relic from the early Universe, the Planck collaboration has inferred a H_0 value of 67.4 ± 0.5 km s^{-1} Mpc^{-1} under the assumption of the standard cosmological model (cold dark matter with a cosmological constant, ΛCDM) (Planck Collaboration et al., 2020). However, using data from the local (or late) Universe and a cosmic distance ladder approach, where absolute magnitudes of type Ia supernovae in the Hubble flow have been calibrated by Cepheids and parallax distances, the SHOES team has reported a H_0 value of 74.0 ± 1.4 km s^{-1} Mpc^{-1} (Riess et al., 2021). Several other independent probes also bolster this discrepancy between the model-dependent extrapolation and direct measurement of H_0 (e.g., Abbott et al., 2018; Aiola et al., 2020; Freedman et al., 2020; Pesce et al., 2020; Kourkchi et al., 2020; Blakeslee et al., 2021). This unambiguous discrepancy is currently known as the Hubble tension (see Fig. 1.1) (Verde et al., 2019; Abdalla et al., 2022). If systematic uncertainties in the measurement processes cannot account for this discrepancy, modifying the standard cosmological model or introducing new physics would be necessary.

Early-type galaxies (ETGs) can contribute to resolving the Hubble tension via the strong lensing time-delay method. This method provides a one-step measurement of the distance scale and thus H_0 (Refsdal, 1964; Treu & Marshall, 2016) and is independent of the above two methods. Given

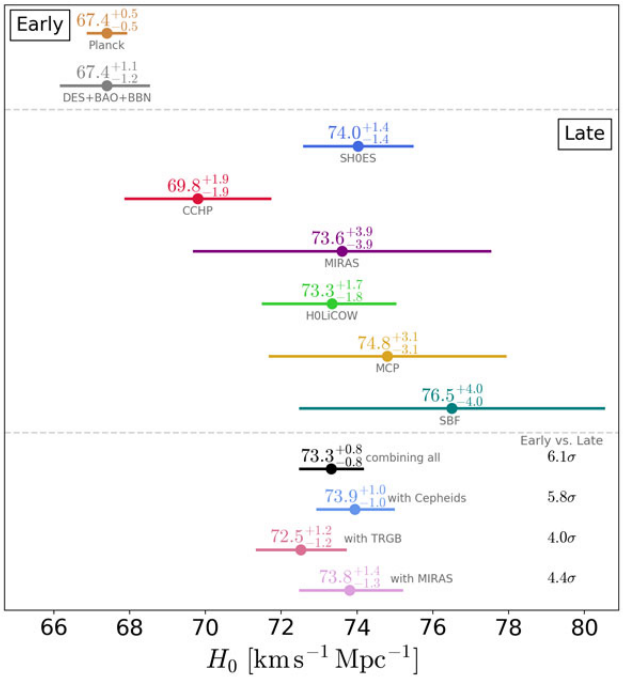


Figure 1.1: Discrepancy in inferred and measured H_0 values from early and late Universe distant anchors, a.k.a. Hubble tension (Verde et al., 2019). The inferred H_0 utilizing data from the early Universe is clustered around 67 km s^{-1} Mpc^{-1}while the measurements from different late Universe distant anchors are around 74 km s^{-1} Mpc^{-1}. The combined discrepancy considering all measurements from the early and late Universe shown in this plot is 6.1σ

the ambiguity about whether the H_0 tension arises from systematic uncertainties in measurements or new physics, an independent probe like this is crucial. When a time variable source such as a quasar or a supernova is strongly lensed by a foreground galaxy (deflector), multiple images of the background source form, and the lensed light from these images arrive at different times [Fig 1.2]. For a fixed source position β, we can then measure the time-delay Δt between two images located at angular positions θ_A and θ_B as

$$\Delta t_{AB} = \frac{(1+z_d)}{c}\frac{D_d D_s}{D_{ds}}\left((\theta_A-\beta)^2-(\theta_B-\beta)^2-(\psi(\theta_A)-\psi(\theta_B))\right) \tag{1.2}$$

where z_d is the deflector redshift, D_d, D_s, D_{ds} are respectively the angular diameter distances between the observer and the deflector, the observer and the source, and the deflector and source, and ψ is the gravitational potential (this is a scaled 2D version of the 3D potential and depends on mass distribution) of the deflector. The combination of three angular diameter distances along with the deflector redshift factor is referred to as the time-delay distance, $D_{\Delta t}$:

$$D_{\Delta t} \equiv (1+z_d)\frac{D_d D_s}{D_{ds}} \propto \frac{1}{H_0} \tag{1.3}$$

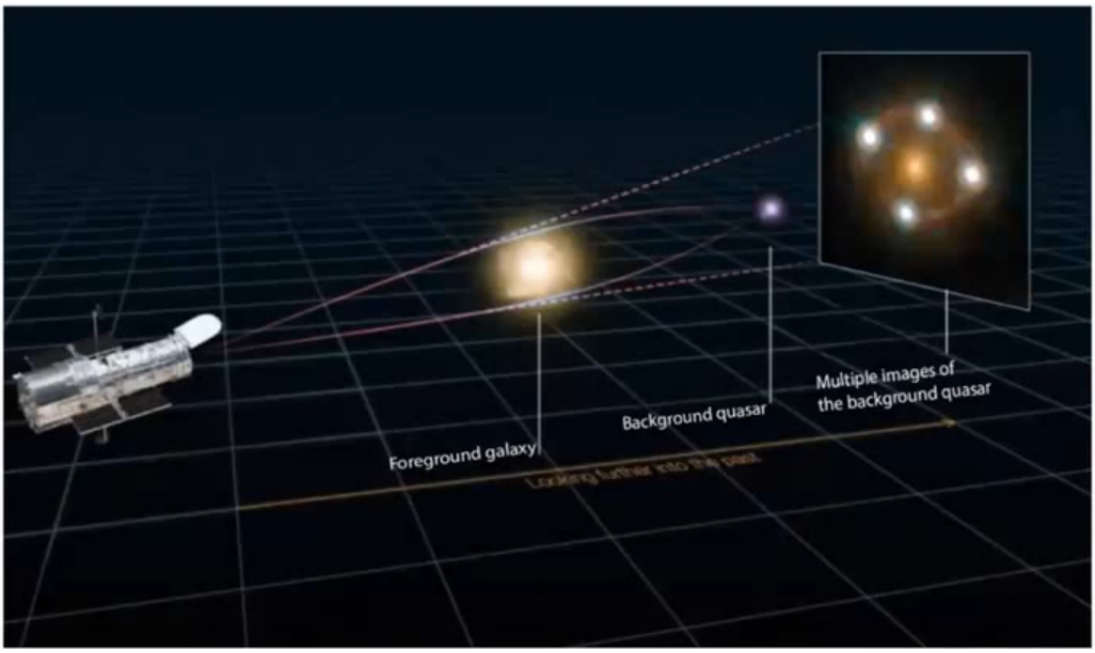


Figure 1.2: Strong lensing of the background quasar by the foreground galaxy creates four images of the source and variations in light travel time from each of these lensed images along with other data sets, allow us to measure H_0 via time-delay cosmography method (Illustration: Martin Millon/Swiss Federal Institute of Technology Lausanne. Galaxy and quasar image: Hubble Space Telescope/NASA).

By measuring high-precision time delays from multiple images, $\mathcal{D}_{\rm td}$, and redshifts and stellar kinematics of the deflector from spectroscopy, $\mathcal{D}_{\rm spec}$, accurately modeling the mass distribution within the deflector, $\mathcal{D}_{\rm img}$ and estimating the extra-lensing deflection due to the large-scale mass distribution between the source and observer along the line of sight, $\mathcal{D}_{\rm los}$, one can infer $D_{\Delta t}$ and hence constrain H_0 as it is inversely proportional to the time-delay distance (e.g., Wong et al., 2020; Millon et al., 2020b; Birrer et al., 2020; Rusu et al., 2020; Shajib et al., 2020; Chen et al., 2019).

As these data sets are independent, one can formulate four independent likelihoods and combine them to conduct a joint cosmographic inference of H_0 using a Bayesian framework (Birrer et al., 2020). For a set of cosmographic parameters $\theta_{\rm cos}$ and the data set, $\mathcal{D} = \left\{\mathcal{D}_{\rm img}\,, \mathcal{D}_{\rm td}\,, \mathcal{D}_{\rm spec}\,, \mathcal{D}_{\rm los}\right\}$,

the joint likelihood can be written as

$$\begin{aligned}\mathcal{L}\left(\mathcal{D} \mid \theta_{\rm cos}\right) = \int & \mathcal{L}\left(\mathcal{D}_{\rm img} \mid \xi_{\rm mass}, \xi_{\rm light}\right) \\ & \times \mathcal{L}\left(\mathcal{D}_{\rm td} \mid \xi_{\rm mass}, \xi_{\rm light}, \lambda, \theta_{\rm cos}\right) \\ & \times \mathcal{L}\left(\mathcal{D}_{\rm spec} \mid \xi_{\rm mass}, \xi_{\rm light}, \beta_{\rm ani}, \lambda, \theta_{\rm cos}\right) \\ & \times \mathcal{L}\left(\mathcal{D}_{\rm los} \mid \kappa_{\rm ext}\right) \\ & \times p\left(\xi_{\rm mass}, \xi_{\rm light}, \lambda, \kappa_{\rm ext}, \beta_{\rm ani}\right) {\rm d}\xi_{\rm mass}\, {\rm d}\xi_{\rm light}\, {\rm d}\lambda\, {\rm d}\kappa_{\rm ext}\, {\rm d}\beta_{\rm ani}.\end{aligned}$$

In the above joint likelihood, $\xi_{\rm light}$ includes the parameters related to the source and deflector surface brightness, $\xi_{\rm mass}$ comprises parameters related to the deflector mass distribution, λ is related to mass-sheet transform (MST), $\beta_{\rm ani}$ describes anisotropy in the orbital distribution of the stellar velocity and $\kappa_{\rm ext}$ encodes the mass distribution along the LOS. This likelihood combines datasets from a single-lens system. However, we can adopt a Bayesian hierarchical framework and incorporate datasets from a sample of time-delay lenses. As the dataset from each lens system is independent, the joint likelihood would take the form

$$p\left(\theta_{\rm cos} \mid \{\mathcal{D}_i\}_N\right) \propto \int \prod_i^N \mathcal{L}\left(\mathcal{D}_i \mid \theta_{\rm cos}, \xi\right) p(\theta_{\rm cos}, \xi) {\rm d}\xi$$

Here ξ represents all the nuisance parameters. Among the nuisance parameters, some are sampled globally at the population level but others are constrained independently per lens. The advantage of the hierarchical method is that it allows us to constrain those parameters that could not be efficiently constrained for an individual lens and as a result, it provides a tighter constraint on H_0.

Considerable improvements over the last two decades in the data quality and analysis techniques in all the aspects of the time-delay strong lensing method have transformed this approach into an effective and reliable tool to measure H_0. However, the well-known mass-sheet degeneracy and mass-anisotropy degeneracy (MAD) impose significant uncertainty in the inference of H_0 through this method. The MST is a mathematical degeneracy that implies that different mass distributions in the deflector can predict the same set of imaging observables (image position, flux ratios, etc.). As these different mass models lead to different time-delay distances, the precision of the measured value of H_0 suffers considerably. Assuming a specific mass model such as the power-law mass profile can induce a potential systematic in the H_0 because such an assumption artificially breaks the MST (e.g., Xu et al., 2016; Sonnenfeld, 2018; Kochanek, 2020, 2021).

Assuming such a mass model and utilizing data from six lens systems, the H0LiCOW collaboration has inferred a H_0 value of 73.3 km s^{-1} Mpc^{-1} with 2.4% uncertainty (Wong et al., 2020). However, if the mass model assumptions were relaxed, then uncertainty on the inferred H_0 increases significantly as the MST is only constrained by stellar kinematics and time-delay measurements (see the joint likelihood definition above). Using seven lenses, six of which are from H0LiCOW, with single aperture kinematics and a maximally flexible mass profile, Birrer et al. (2020) measured H_0 = 74.5 km s^{-1} Mpc^{-1} with 8% uncertainty. Therefore, the stellar kinematics of the deflector is one of the crucial ingredients to accurately measure H_0 with time-delay cosmography, when the maximal degeneracy in H_0 due to the MST of the mass model is allowed to be explored (Birrer et al., 2020; Birrer & Treu, 2021). Additionally, stellar kinematics are the only data that depends on anisotropy (β_{ani}) and thus they can constrain mass-anisotropy degeneracy (MAD). However, to achieve percent-level precision, a sample of 40 or more time-delay lenses, for which we have measured stellar kinematics of the deflectors to 5% or better, is required in addition to kinematic information from a large sample of non-time-delay lenses (Birrer & Treu, 2021). In this regard, I measured the integrated and resolved kinematics of several lens ETGs to increase the current sample size.

1.2.2 Stellar kinematics of ETGs to measure H_0

Stellar kinematics of ETGs could improve the precision of H_0 inference from the following three directions

- Stellar kinematics and redshifts of the lensing galaxies are necessary to increase the sample size of the quasar-galaxy lens systems for which the Hubble constant can be measured, hence increasing the precision of its inference. However, it is challenging to even extract uncontaminated and high signal-to-noise ratio (S/N) 1D spectra of the deflectors. The angular separations between the quasar images and the deflector in a lens system are typically on the order of 1″. Hence, in seeing limited ground-based observations, the observed spectra of the lens systems become spatially blended. The situation is more complicated as the deflectors are generally orders of magnitude fainter than the bright quasar images. Traditional optimal extraction codes based on the algorithm of Horne (1986) are not up to the task as they do not account for the blending or cross-contamination. Hence, better extraction codes are required

to overcome these issues. One possible solution is to forward model all the light within an aperture and then extract only the deflector contribution. In this work, I implemented such a method and successfully extracted integrated stellar kinematics of several lensing galaxies.

- The MST is a mathematical degeneracy that could be partially mitigated in a model-independent way using the integrated stellar velocity dispersion of the lensing galaxy (Treu & Koopmans, 2002; Suyu et al., 2014; Birrer et al., 2020). However, to alleviate the MAD, the resolved velocity dispersion of the lensing galaxies is required. Extracting resolved kinematics of a lensing galaxy is a much more daunting task than achieving integrated kinematics because of the reasons described in the above section. Nevertheless, I have helped to extract resolved kinematics of the lensing galaxy in the quasar-lens system RXJ1131-1231. In Shajib et al. (2023), we found that by introducing this resolved kinematics for only one lens system while keeping other relevant data unchanged, it is possible to achieve a similar level of precision on H_0 inference as from the seven systems with only integrated velocity dispersions.

- Given the challenges associated with extracting both integrated and resolved stellar kinematics from lensing galaxies, an alternative approach can be employed. In this study, I compiled a sample of non-lensed early-type galaxies (ETGs) at intermediate redshift with high-quality IFU data for the purpose of studying galaxy evolution. From this sample, I selected a subset of ETGs whose redshift and integrated velocity dispersion match the range of the TDCOSMO sample of lensing galaxies. The resolved kinematics data extracted from this selected non-lensed sample can provide insights into the global anisotropy of TDCOSMO like early-type galaxies at the population level. This knowledge can be incorporated as an informed prior in the Bayesian hierarchical framework for H_0 inference, thereby indirectly addressing the mass-anisotropy degeneracy. However, due to time constraints, I have not been able to complete this project, which remains as future work.

1.3 Overview of this dissertation

In the next chapter, I describe a forward modeling method, and how this method was utilized to extract high S/N 1D spectra of eight lens galaxies. From the extracted spectra, redshifts and

integrated velocity dispersions were measured with high precision. I also suggested a framework to estimate systematic and statistical uncertainties of the velocity dispersion measurements along with their associated covariances. These results, combined with other ancillary data, such as high-resolution images of the lens systems, and time delays, will help to reach percent-level precision on the H_0 inference by adding to the current TDCOSMO quasar-galaxy lens sample. Additionally, the proposed framework for systematic tests is being incorporated into the TDCOSMO kinematics pipeline.

Next, in Chapter 3 I have gathered a sample of massive ETGs within the redshift range of 0.25-0.75 from existing ESO archive data observed through the Multi-Unit Spectroscopic Explorer (MUSE) and extracted under the MUSE-DEEP[1] collection. These IFU data with unprecedented depth and high SNR are favorable to extracting resolved stellar kinematics up to a few effective radii. Using these high SNR data I measured various kinematic, morphological, and stellar population properties of this sample. From these measurements, I estimated global trends in early-type galaxies at intermediate redshifts and compared them with their local counterparts.

In chapters 4 and 5, I used this MUSE sample of ETGs to investigate two unresolved questions in galaxy evolution. I investigated the degree to which ETGs at intermediate redshift are supported by rotation versus random stellar motions in Chapter 4. To conduct this analysis, I used the galaxy parameters measured in Chapter 3 and applied corrections when necessary. From this analysis, I found significant evidence of a decrease in rotational support over cosmic time. To compare with a local reference, I used a sample of ETGs from the MaNGA survey, focusing on galaxies with redshifts below 0.05 and stellar masses of $\log M_*(M_\odot) \geq 10.65$. In Chapter 5, I used Jeans anisotropic modeling to measure the total density slope of the MUSE sample. This technique measures the total density slopes by predicting the second moments of the stellar velocity distribution and comparing them with observed kinematic maps. I utilized the high SNR resolved kinematics maps of the MUSE galaxies extracted in Chapter 3 for this analysis.

Finally, in Chapter 6, I summarize the main results from each chapter, discuss some future projects, and conclude this dissertation.

[1] https://doi.org/10.18727/archive/42

Chapter 2

Lensing galaxy redshift and velocity dispersion measurements from Keck spectroscopy

This chapter was published as Mozumdar, P., et al., 2023, A&A 672, A20 and reproduced here with minor formatting changes.

We have measured the redshifts and single-aperture velocity dispersions of eight lens galaxies using the data collected by the Echellette Spectrograph and Imager (ESI) and Low-Resolution Imaging Spectrometer (LRIS) at W.M. Keck observatory on different observing nights spread over three years (2018-2020). These results, combined with other ancillary data, such as high-resolution images of the lens systems, and time delays, are necessary to increase the sample size of the quasar-galaxy lens systems for which the Hubble constant can be measured, using the time-delay strong lensing method, hence increasing the precision of its inference. Typically, the 2D spectra of the quasar-galaxy lens systems get spatially blended due to seeing by ground-based observations. As a result, the extracted lensing galaxy (deflector) spectra become significantly contaminated by quasar light, which affects the ability to extract meaningful information about the deflector. To account for spatial blending and extract less contaminated and higher signal-to-noise ratio (S/N) 1D spectra of the deflectors, a forward modeling method has been implemented. From the extracted spectra, we have measured redshifts using prominent absorption lines and single aperture velocity dispersions using the penalized pixel fitting code pPXF. In this paper, we report the redshifts and single aperture velocity dispersions of eight lens galaxies—J0147+4630, B0445+123, B0631+519, J0659+1629, J0818-2613, J0924+0219, J1433+6007, and J1817+2729. Among these systems, six do not have previously measured velocity dispersions; for the other two, our measurements are consistent with previously reported values. Additionally, we have measured the previously unknown redshifts of

the deflectors in J0818-2613 and J1817+2729 to be 0.866 ± 0.002 and 0.408 ± 0.002, respectively.

2.1 Introduction

The Hubble constant, H_0, denotes the current expansion rate of our Universe. The value of H_0, though first measured almost a century ago, is still a matter of debate. Utilizing cosmic microwave background (CMB) radiation, which is a relic from the early universe, the Planck collaboration has measured a Hubble parameter at the last scattering surface ($z \sim 1100$) and then inferred a H_0 value of 67.4 ± 0.5 km s^{-1} Mpc^{-1} (Planck Collaboration et al., 2020) under the assumption of the standard cosmological model (cold dark matter with a cosmological constant, ΛCDM). However, using data from the local (or late) Universe and a cosmic distance ladder approach, where absolute magnitudes of type Ia supernovae in the Hubble flow have been calibrated by Cepheids and parallax distances, the SH0ES team has measured $H_0 = 73.04 \pm 1.04$ km s^{-1} Mpc^{-1} (Riess et al., 2021). Several other independent probes also bolster this discrepancy between the model-dependent extrapolation and direct measurement of H_0 (e.g., Abbott et al., 2018; Aiola et al., 2020; Freedman et al., 2020; Pesce et al., 2020; Kourkchi et al., 2020; Blakeslee et al., 2021). This unambiguous discrepancy is currently known as the Hubble tension (Verde et al., 2019; Abdalla et al., 2022). If systematic uncertainties in the measurement processes cannot account for this discrepancy, modifying the standard cosmological model or introducing new physics would be necessary. In this picture, more independent probes are crucial to resolving this issue.

One independent way to measure H_0 is to use the time-delay strong lensing method (Refsdal, 1964). When a time variable source such as a quasar or a supernova is strongly lensed by a foreground galaxy (deflector), multiple images of the background source form, and the lensed light from these images arrive at different times. These relative delays depend on the gravitational potential (mass distribution) of the deflector, the large-scale mass distribution along the line of sight, and a combination of angular diameter distances involving the source, deflector, and observer, called the time-delay distance ($D_{\Delta t}$). By measuring high-precision time delays from multiple images and redshifts of the deflector and the source from spectroscopy, accurately modeling the mass distribution within the deflector, and estimating the extra-lensing deflection due to the large-scale mass distribution between the source and observer along the line of sight, one can infer $D_{\Delta t}$ and angular

diameter distance to the deflector (D_d), and, hence constrain H_0 as it is inversely proportional to the time-delay distance (e.g., Wong et al., 2020; Millon et al., 2020b; Birrer et al., 2020; Rusu et al., 2020; Shajib et al., 2020; Chen et al., 2019). Since the first robust measurement of the time delays in the J0957+561 system, and the associated determination of H_0 (Kundić et al., 1997; Oscoz et al., 1997, 1996), considerable improvements in the data quality and analysis techniques in all the aspects of the time-delay strong lensing approach over the last two decades have transformed this method into an effective and reliable tool to measure H_0. However, the well-known mass-sheet transform (MST; Falco et al., 1985; Schneider & Sluse, 2013) can still introduce significant uncertainty in this method (e.g, Birrer et al., 2020). The MST is a mathematical degeneracy which implies that different mass distributions in the deflector can predict the same set of imaging observables (image position, flux ratios, etc.). As these different mass models lead to different time-delay distances, the precision of the measured value of H_0 suffers considerably. Assuming a specific mass model such as the power-law mass profile can induce a potential systematic in the H_0 because such an assumption artificially breaks the MST (e.g., Xu et al., 2016; Sonnenfeld, 2018; Kochanek, 2020, 2021). However, this mathematical degeneracy is mitigated by introducing an independent tracer of mass, such as the stellar velocity dispersion of the deflector (Treu & Koopmans, 2002; Koopmans et al., 2003; Suyu et al., 2014). Therefore, the stellar kinematics of the deflector is one of the crucial ingredients to accurately measure H_0 using time-delay cosmography when the maximal degeneracy in H_0 due to the MST of the mass model is allowed to be explored (Birrer et al., 2020; Birrer & Treu, 2021). One can also impose tighter constraints on other cosmological parameters from joint inference of $D_{\rm d}$ and $D_{\Delta t}$ by combining the time-delay measurements and lens models with the stellar velocity dispersions of the deflectors (e.g., Jee et al., 2015, 2016; Birrer et al., 2016, 2019; Shajib et al., 2018).

Besides improving the robustness of the analysis methods, and checking for unknown systematics (Millon et al., 2020b; Gilman et al., 2020; Chen et al., 2021b; Van de Vyvere et al., 2022; Shajib et al., 2022; Gomer et al., 2022), another ongoing effort of the Time-Delay COSMOgraphy (TDCOSMO) collaboration is to increase the sample size of lensed quasar systems with measured $D_{\Delta t}$. By mitigating the uncertainties at the population level, this large sample of quasar-galaxy lens systems with their associated data, especially stellar velocity dispersion of the deflectors, can help to achieve a sub-percent measurement of H_0 (Birrer & Treu, 2021). This coordinated effort

covers observations and analyses of important properties. For example, measuring time delays requires monitoring of the source images' light curves with adequate sampling (e.g., Courbin et al., 2018; Millon et al., 2020a). High-resolution imaging from the *Hubble Space Telescope* (*HST*) or ground-based adaptive optics (AO) instruments is crucial for lens modeling (e.g., Wong et al., 2017; Shajib et al., 2019; Chen et al., 2019). High S/N spectroscopic observations provide redshifts of the source and the deflector along with stellar kinematics of the deflector (e.g., Suyu et al., 2017). Environmental studies of the lens systems to quantify the extra-lensing distortion also depend on photometric and spectroscopic observations (e.g., Rusu et al., 2017; Sluse et al., 2019). As a part of this effort, in this paper, we report newly measured redshifts and single aperture velocity dispersions of the deflectors from eight quasar-galaxy lens systems—J0147+4630, B0445+123, B0631+519, J0659+1629, J0818-2613, J0924+0219, J1433+6007, and J1817+2729.

Due to limitations associated with the ground-based observations, the 2D spectra of the quasar-galaxy lens systems are typically spatially blended, and it is a challenging task to extract clean and high S/N 1D spectra of the deflectors. To overcome this issue, we have implemented a forward modeling method to extract 1D spectra of the deflectors and, provided the S/N of the extracted spectra are sufficiently high, we have measured single aperture velocity dispersions and the redshifts. This paper is structured in the following way. In section 2.2, a brief description of the target lens systems and related information is provided. Next, the observational setup, data reduction pipeline, and how the 1D spectra have been extracted using the forward modeling method are described in section 2.3. In section 2.4, the measurement process of the redshifts and the single aperture velocity dispersions of the deflectors are presented along with the results. Finally, sections 2.5 and 3.6 discuss the reported results and conclusions respectively. A flat ΛCDM cosmology with $H_0 = 70.0$ km s^{-1} Mpc^{-1}and $\Omega_{\rm m} = 0.3$ is adopted when necessary.

2.2 Targets

This section provides a brief description of the eight quasar-galaxy lens systems for which the deflector redshifts and velocity dispersions are measured. The images of these lens systems along with the slit positions are presented in Figure 2.1.

Table 2.1: Summary of spectroscopic observation of the lens systems for which redshifts and stellar velocity dispersions of the deflectors have been reported in this paper. Position angle (PA) of the slits was measured from North to East direction. The seeing conditions (FWHM) were estimated using the data from the corresponding nights.

Lens system	RA (J2000)	Dec (J2000)	Date of observation (UT)	Instrument	Total exposure (sec)	Seeing (arcsec)	Slit PA (degree)	Slit width (arcsec)	Slit Length (arcsec)
J0147+4630	01:47:10.20	+46:30:40.50	Dec 1, 2018	ESI	7200	0.70	7	1.0	20
B0445+123	04:48:23.25	+12:27:51.10	Dec 13, 2020	LRIS	12000	1.06	67	1.5	175
B0631+519	06:35:11.70	+51:56:48.50	Nov 21, 2020	LRIS	6080	0.69	315	1.0	175
J0659+1629	06:59:03.82	+16:29:08.90	Mar 3, 2019	LRIS	6800	1.33	65	1.0	175
J0818-2613	08:18:28.24	−26:13:24.80	Apr 10, 2019	ESI	3600	0.71	90	1.0	20
J0924+0219	09:24:55.82	+02:19:24.80	Dec 1, 2018	ESI	7200	0.70	10	1.0	20
J1433+6007	14:33:22.80	+60:07:15.60	Apr 10, 2019	ESI	7200	0.71	88	1.0	20
J1817+2729	18:17:30.68	+27:29:43.50	Apr 10, 2019	ESI	4800	0.71	315	1.0	20

2.2.1 J0147+4630

This quadruple lensed quasar system was coincidentally discovered (Berghea et al., 2017) in the Panoramic Survey Telescope and Rapid Response System (Pan-STARRS1; Chambers et al., 2016) survey data. The spectroscopic redshift of the quasar is 2.341 ± 0.001 (Lee, 2017). The redshift of the deflector is also measured, $z_d = 0.678 \pm 0.001$, along with the velocity dispersion, 313 ± 14 km s^{-1}, by Goicoechea & Shalyapin (2019). In this paper, we provide an independent measurement of the velocity dispersion of the deflector using a larger wavelength range than the one used in the previous measurement. Lens modeling has been carried out by Shajib et al. (2019) using *HST* imaging of the system.

2.2.2 B0445+123

This radio-loud double-imaged AGN was discovered by Argo et al. (2003) in the Cosmic Lens All-Sky Survey (CLASS; Myers et al., 2003; Browne et al., 2003). Radio observations have measured the separation between the lensed images to be $1.32''$. Although the AGN redshift is yet to be measured, spectroscopic observations have found that the deflector redshift is $z_d = 0.5583 \pm 0.0003$ (McKean et al., 2004).

2.2.3 B0631+519

This is another radio-loud double-imaged lens system discovered by CLASS (York et al., 2005). Observations at different radio wavelengths have revealed two compact lensed images separated by around $1.16''$. *HST* imaging of the system has shown that there are two galaxies along the line of sight of the quasar. The main lensing galaxy is at redshift, $z_d = 0.6196 \pm 0.0004$ and the other one is at redshift 0.0896 ± 0.0001 (McKean et al., 2004). However, the quasar redshift is yet unknown.

2.2.4 J0659+1629

This quadruply-lensed quasar was first identified as a lens candidate by Delchambre et al. (2019) using *Gaia* data release 2 (Gaia Collaboration et al., 2018). This detection was confirmed by Stern et al. (2021) with measured source redshift, $z_s = 3.083$ and deflector redshift, $z_d = 0.766$. The system was also independently discovered by Lemon et al. (2022). Lens modeling of the system is conducted by Schmidt et al. (2022) using *HST* imaging.

2.2.5 J0818-2613

Stern et al. (2021) first discovered this quadruply imaged quasar system using *Gaia* data release 2 and measured the quasar redshift, $z_s = 2.164$, using Keck-LRIS spectroscopy. This lens system was also independently reported by Lemon et al. (2022) with a measured quasar redshift, $z_s = 2.155$. Schmidt et al. (2022) performed lens modeling using *HST* images of the system. In this paper, we report the redshift and velocity dispersion of the deflector.

2.2.6 J0924+0219

This quadruply lensed quasar was discovered using Sloan Digital Sky Survey (SDSS; York et al., 2000) data. Inada et al. (2003) first reported this quad along with the measured source redshift $z_s = 1.524$, while Ofek et al. (2006) and Eigenbrod et al. (2006) measured the lens redshift, $z_d = 0.393$. Time-delay data between the two brightest images is available (Millon et al., 2020a). Lens modeling is presented by Eigenbrod et al. (2006) using *HST* imaging and recently by Chen et al. (2021a) using AO-based imaging.

2.2.7 J1433+6007

This quad was detected in the SDSS data release 12 photometric catalog (Alam et al., 2015). The source and deflector redshift, and deflector velocity dispersion were first measured by Agnello et al. (2018). The reported redshifts of the source and the deflector are, $z_s = 2.737 \pm 0.003$ and $z_d = 0.407 \pm 0.002$, respectively. The measured velocity dispersion is 216 ± 55 km s^{-1} using a $1''$ aperture (Agnello et al., 2018). However, this measurement only used the Ca K line and the spectrum was significantly contaminated by quasar light. In this paper, we present a new velocity dispersion measurement on a larger wavelength range and higher S/N deflector spectrum. Shajib et al. (2019) and Schmidt et al. (2022) both performed lens modeling using *HST* imaging.

2.2.8 J1817+2729

This quad was first identified as a lens candidate by Delchambre et al. (2019) using *Gaia* data release 2 and then independently confirmed with measured source redshift, $z_s = 3.07$, by Lemon et al. (2019); Stern et al. (2021). Detailed mass modeling has been conducted by Rusu & Lemon (2018) using SUBARU/FOCAS imaging and by Schmidt et al. (2022) using *HST* imaging. In this paper, we present the deflector's redshift and velocity dispersion.

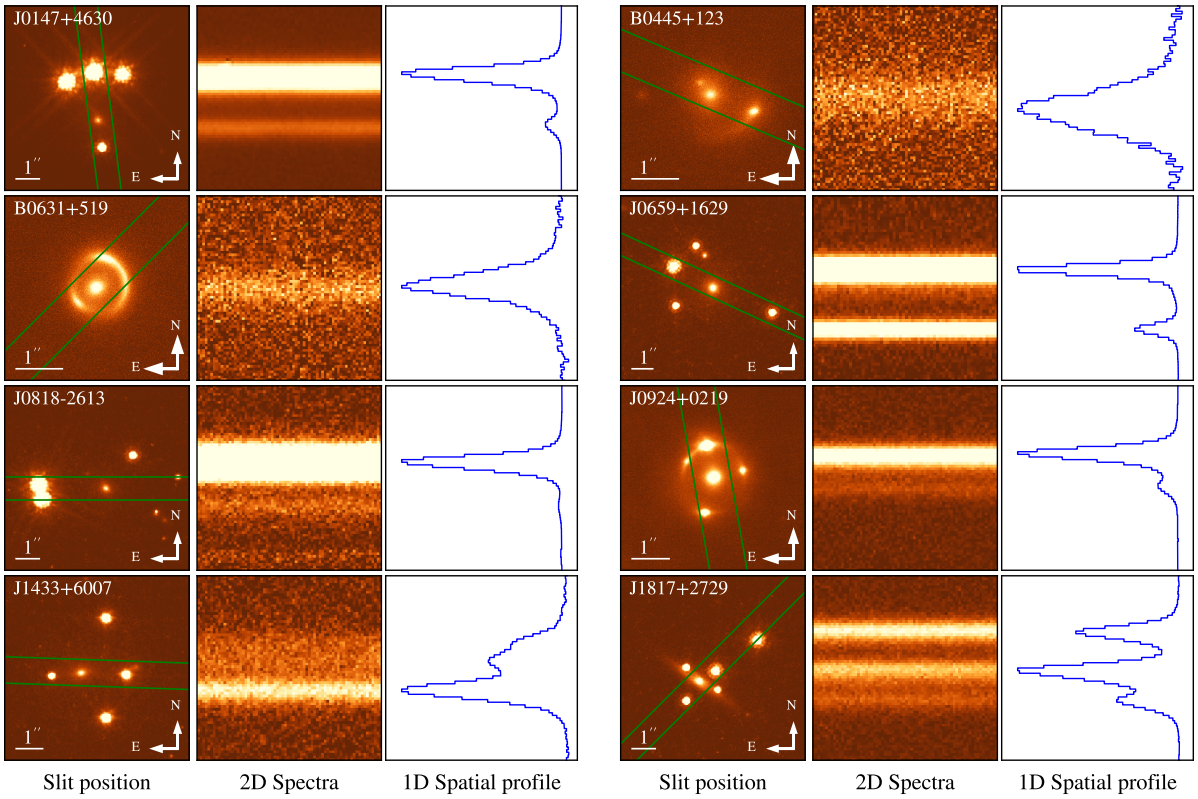


Figure 2.1: Images of the lens systems, part of the collected 2D spectra, and the corresponding 1D spatial profiles. The 1D spatial profiles have been generated by collapsing the data in the 2D spectra along the spectral axis. The slit position (green) for each lens system is also shown. For the lens system, J0147+4630, J0659+1629, J0818-2613, J1433+6007, and J1817+2729, we have used archival *HST* images (PI: T. Treu) and for B04453+123, B0631+519 and J0924+0219, we have used ground based AO images (PI: C. D. Fassnacht).

2.3 Observations and data reduction

In this section, we first describe the observations for our sample of eight lens systems, which include two different spectrographs and three different setups. Next, the data reduction pipelines are described. Finally, we present the forward modeling method and how the 1D spectra were extracted from the respective 2D spectra.

2.3.1 Observations

The spectroscopic observations for the target lens systems were carried out using the Low Resolution Imaging Spectrometer (LRIS; Oke et al. 1995) and the Echellette Spectrograph, and Imager (ESI; Sheinis et al. 2002) mounted on the 10m Keck telescopes. The observing nights were spread over three years, from 2018 to 2020, with typical seeing conditions (FWHM) ranging $\sim 0.7\,''$ - $1.33\,''$.

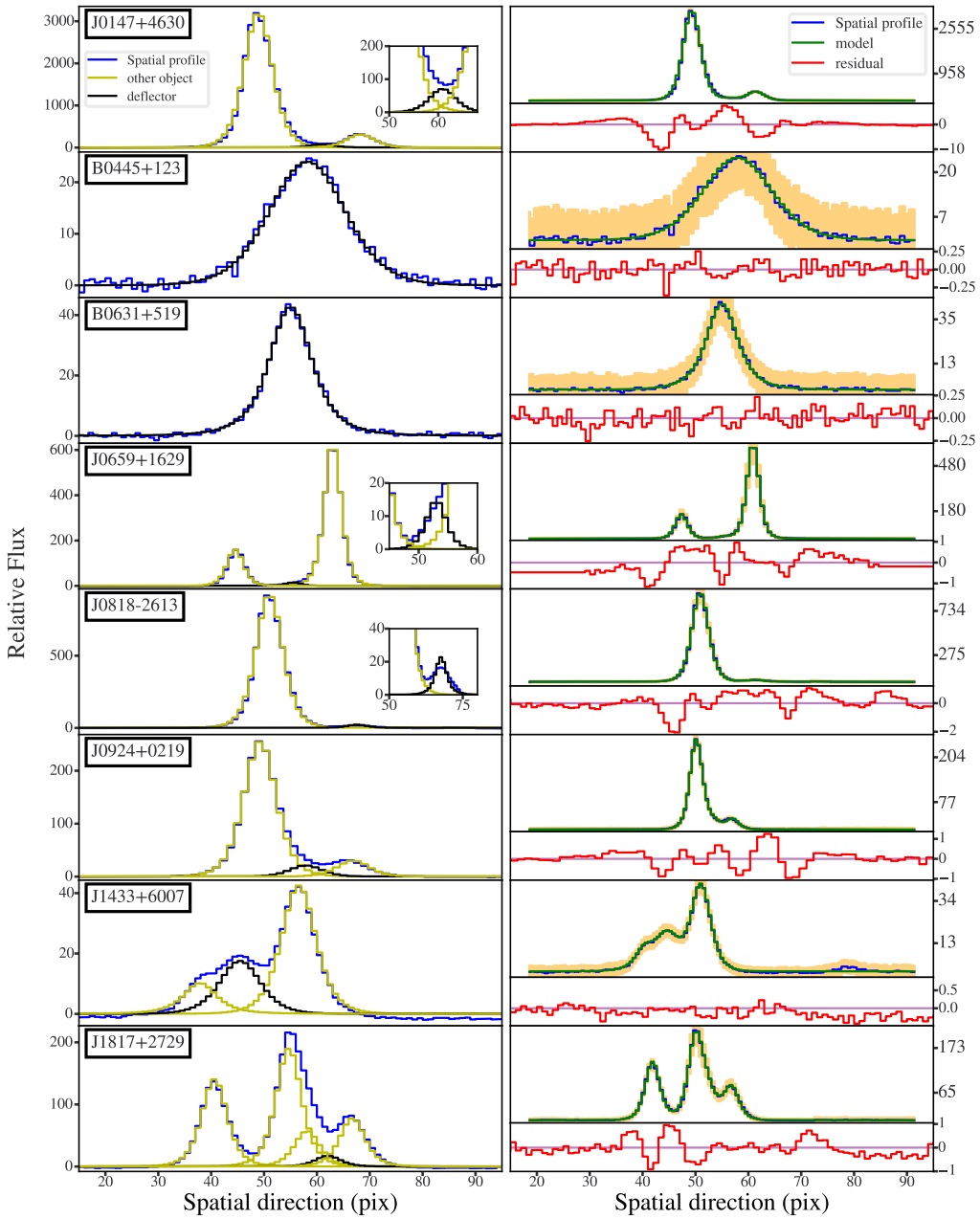


Figure 2.2: Illustration of model fitting to 1D spatial profiles. Left column - each row shows the 1D spatial profile (blue) with individual model components for a single lens system. The model components are Moffat profiles, which represent the deflector and lensed quasars, with an additive polynomial function representing the background. The profile component representing the deflector is marked black and other profile components generally representing the lensed quasar images are marked with yellow. Right column - The top panel in each row shows the 1D spatial profile (blue) with 1σ uncertainty (orange) and the corresponding model (green) that fits the data in that profile. The bottom panel shows the residual (red) between the data and the model normalised to the uncertainties in data. The uncertainties on the spatial profiles of B0445+123 and B0631+519 are higher compared to others because these 1D profiles were generated from single frames, while for other lens systems, the corresponding profiles were generated from coadded frames.

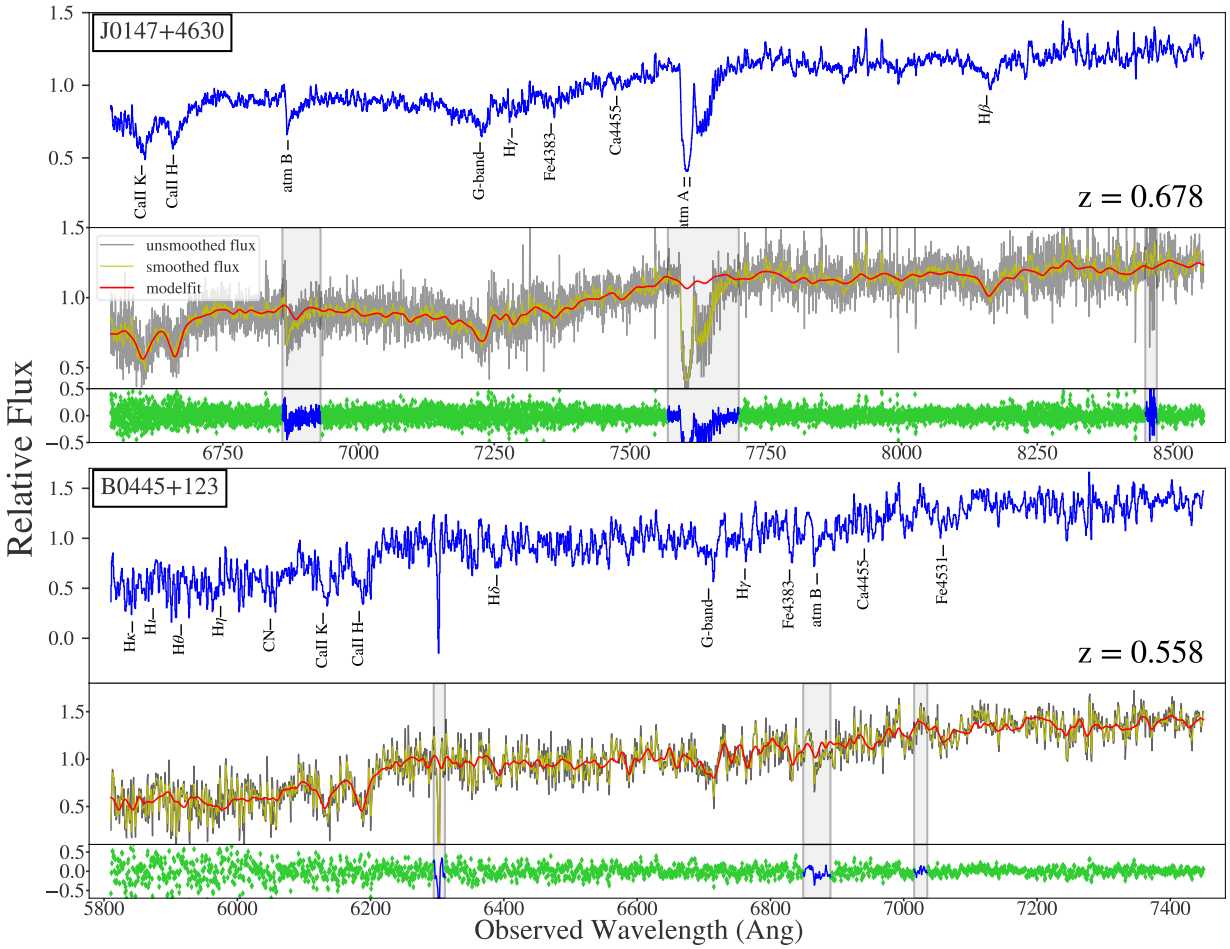


Figure 2.3: 1D spectra and velocity dispersion fits for the deflectors from the lens system J0147+4630 and B0445+123. The plot for each system consists of three panels. Top panel - the extracted and smoothed 1D spectrum of the deflector is plotted over the observed wavelength where the smoothing has been done using a boxcar filter of size around 2.5 Å. Prominent stellar and telluric absorption lines are marked if present. And the measured redshift of the deflector is mentioned in the lower right corner of the plot. Middle panel - the pPXF generated model fit (red) to measure the velocity dispersion is plotted on top of the original unsmoothed spectrum (black). A smoothed version (yellow) of the original spectrum is also presented to show the goodness of the fit. The grey parts are the masked or excluded regions from the fit. Bottom panel - the green dots show the residuals between the unsmoothed flux and the model fit for each wavelength normalized to the respective model fits.

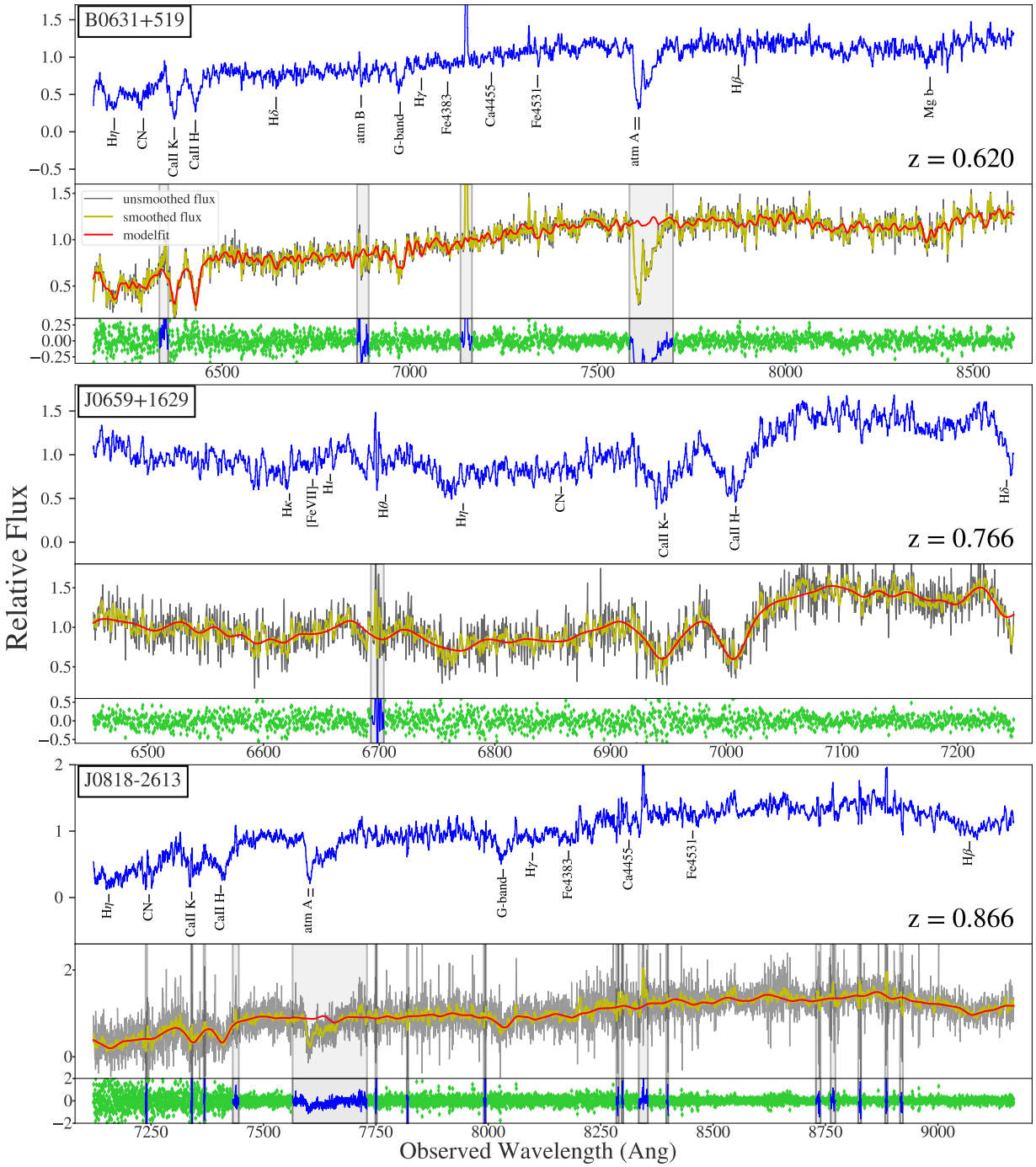


Figure 2.4: 1D spectra and velocity dispersion fits for the deflectors from the lens system B0631+519, J0659+1629 and J0818-2613. The description of the figure is same as Figure 2.3.

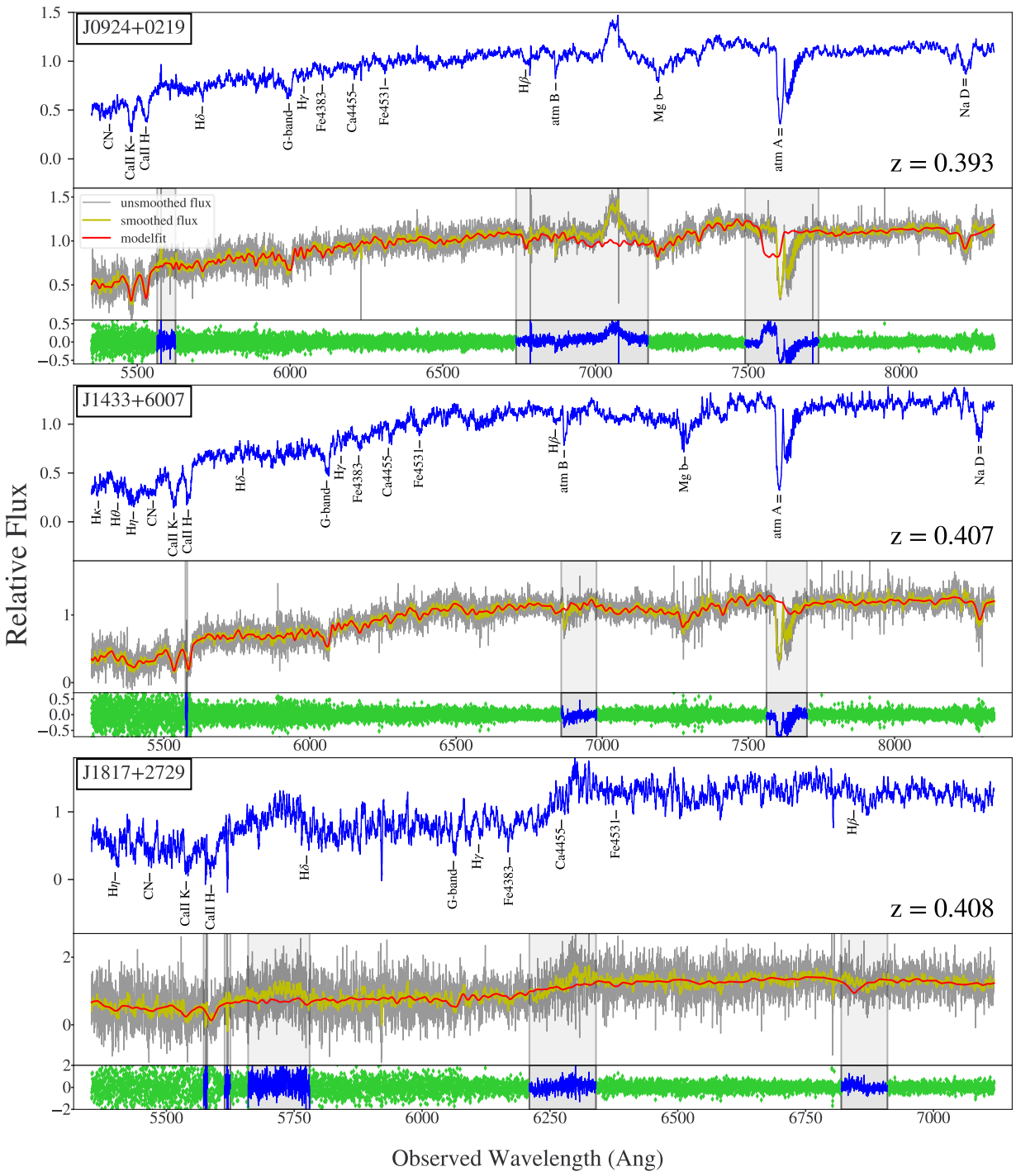


Figure 2.5: 1D spectra and velocity dispersion fits for the deflectors from the lens system J0924+0219, J1433+6007 and J1817+2729. The description of the figure is same as Figure 2.3.

The ESI spectra were taken in Echellette mode using the 1.0″ wide slit which provides a spectral resolution $R \approx 4000$. This setup covers a wavelength range from 3900 Å to 10900 Å with a constant dispersion in logarithmic space corresponding to 11.5 km s^{-1} in velocity, while the pixel scale in the spatial direction varies from 0.120″ in the bluest order to 0.168″ in the reddest order. The LRIS spectra were collected in the long-slit mode using both blue and red arms simultaneously. A dichroic was used to split the light beam at 5696 Å. The blue side was configured with a 600/4000 grism that provides a 0.63 Å/pixel dispersion and covers a wavelength range of 3040-5630 Å with a spectral resolution of $R \approx 1100$ at central wavelength $\lambda \approx 4340$ Å. On the red side, two different configurations were used. To observe the lens systems B0445+123 and B0631+519, a 600/7500 grating was used, which produces a dispersion of 0.8 Å/pixel while covering a wavelength range of 5600-9000 Å. For the lens system J0659+1629, the 1200/7500 grating was used, which covers a wavelength range of 5600-7250 Å with a dispersion of 0.4 Å/pixel. Both setups on the red side provide a spectral resolution of $R \approx 1400$. The plate scales on the blue and the red side are 0.123″/pixel and 0.135″/pixel, respectively. The position angle (PA) of a slit was generally chosen in such a way that the brightest quasar image of the corresponding lens system fell within the slit along with the deflector and at least another quasar image. The total integration time for each system was divided typically into $n \times 2400$ s or $n \times 1800$ s or $n \times 1200$ s exposures. A summary of the main observing information is provided in Table 2.1.

2.3.2 Data reduction

The LRIS data for the lens system B0445+123 and B0631+519 were reduced using the PypeIt (Prochaska et al., 2020) pipeline and for J0659+1629 using the LPipe (Perley, 2019) pipeline. These packages performed overscan subtraction, bias and dark current correction, and flat-fielding. Finally, the packages produced sky-subtracted 2D science spectra and the corresponding variance and wavelength data. PypeIt provides 2D wavelength images while LPipe generates 1D wavelength solutions. The pixels contaminated with cosmic rays were marked by comparing each frame to the respective median frame. A median frame for each system was created by combing all the 2D image frames from that system. After that, a rectification was applied to all reduced 2D data to account for any possible tilts present in the spectra, using a spline interpolation method. These rectified science, variance, and wavelength data were used to extract the 1D spectra, as described in the next section.

The ESI data were processed via a custom python-based data reduction package. The code automatically locates the ten individual spectral orders, performs a bias subtraction and flat field correction on the data, rectifies the orders, subtracts the sky emission, and performs a wavelength calibration. The cosmic-ray rejection for the ESI data was performed by running edge-detection algorithms that our tests have shown to be effective for this process. The output of the code includes the calibrated and background-subtracted data for each exposure and the corresponding variance spectra.

For B0445+123 and B0631+519, the 1D deflector spectra were extracted from each 2D science frame and then coadded using an inverse-variance weighting process to get the final 1D spectra. As the 2D wavelength solutions for these two systems varied from frame to frame, it was easier to handle the issue when the 1D spectra were extracted from each frame. For the remainder of the lens systems, first, the individual 2D spectra were coadded with a inverse variance weighting, and then the 1D deflector spectra were extracted from the coadded 2D spectra.

Table 2.2: Measured redshifts of the deflectors with associated uncertainties using the extracted 1D spectra. Previously known values, if any also given with corresponding references.

Lens system	Redshift (z_d)	Previous measurement	References
J0147+4630	0.678 ± 0.0004	0.678± 0.001	Goicoechea & Shalyapin (2019)
B0445+123	0.558 ± 0.001	0.5583± 0.0003	McKean et al. (2004)
B0631+519	0.620 ± 0.001	0.6196± 0.0004	McKean et al. (2004)
J0659+1629	0.766 ± 0.0015	0.766	Stern et al. (2021)
J0818-2613	0.866 ± 0.002	None	
J0924+0219	0.393 ± 0.0008	0.393	Eigenbrod et al. (2006)
J1433+6007	0.407 ± 0.0006	0.407± 0.002	Agnello et al. (2018)
J1817+2729	0.408 ± 0.002	None	

2.3.3 Forward modeling and 1D extraction

The angular separations between the quasar images and the deflector in a lens system are typically on the order of 1″. Hence, in seeing limited ground-based observations, the 2D spectra of the lens systems become spatially blended. This situation gets more complicated as the deflectors are generally orders of magnitude fainter than the bright quasar images. For example, in Figure 2.1 the 2D spectra of J0147+4630, J0924+0219, and J1817+2729 do not show any distinct trace from the deflector. In this situation, it is challenging to extract uncontaminated and high S/N 1D spectra of the deflectors. Traditional optimal extraction codes based on the algorithm of Horne (1986) are not up to the task as they do not account for the blending or cross-contamination. To overcome this challenge, we have implemented a forward modeling method (e.g., Sluse et al., 2007; Shalyapin & Goicoechea, 2017; Goicoechea & Shalyapin, 2019). First, a global model is created that emulates the data in a 1D spatial profile of the 2D science spectrum. The 1D spatial profile is constructed by collapsing part of the 2D spectrum, typically containing a spectral width of 300-400 pixels, along the spectral axis. The model consists of several Moffat (Moffat, 1969) profiles along with an additive polynomial function. Each component profile in the model represents either a quasar image or the deflector that is wholly or partially captured by the slit and therefore has a significant contribution to the total light distribution across the slit, while the polynomial models the background. The model is further refined by constraining the parameters of the profiles in the following way. The projected center to center distances of the objects along the slit are fixed based on the corresponding measured distances between the objects using archival *HST* images or AO-based images of the systems. We assume that the same point spread function (PSF) is applicable for all objects in the slit, and therefore they require that the profiles have the same shape parameters. This is a reasonable assumption for the galaxies given their point-like sizes in the images of the lens systems, especially when considering the effects of seeing. Figure 2.2 shows a refined global model for each lens system along with individual profile components. This figure also shows the residuals normalized to the uncertainties in the data of the corresponding 1D spatial profiles. Once the initial global description of the spatial profile has been determined, we take a multi-step approach to determine the component fluxes at each wavelength. The spatial profile in a single column of the detector, that is, at a specific wavelength, is typically too noisy to do a full model fit to that single profile. Therefore, we take the following steps to use binned data to determine the model

parameter values in each individual column. (1) We divide the 2D spectrum into spectral bins of equal widths, typically around 20-25 spectral pixels, and construct a series of 1D spatial profiles by summing the 2D data within these spectral-bins. Then we fit the global model to these spatial profiles. From the fitted models, we get a set of values for each centroid and shape parameter in the global model. (2) We fit a low-order polynomial as a function of wavelength to each set of fitted centroid and shape parameters values to describe their wavelength-dependence. (3) We create an individual model similar to the global model for each wavelength using the above-mentioned fitted polynomials, where all the parameters except the amplitudes are kept fixed, and then we fit the amplitudes. (4) We obtain the total flux for each object (quasar or galaxy) at each wavelength by integrating the corresponding fitted Moffat profile along the spatial direction. We also calculate the associated variance on flux using the covariance matrix generated in the fitting process.

All the extracted 1D spectra have been response-corrected using a spectrophotometric standard stellar spectrum collected by the same spectrograph on the corresponding observing night and extracted following the procedure described above. In Figures 2.3 to 2.5, the extracted and smoothed deflector spectra are presented with the absorption and telluric lines marked. The smoothing has been done using a boxcar filter of size around 2.5 Å.

2.4 Data analysis

In this section, we discuss the redshift and velocity dispersion measurements of the deflectors and their associated uncertainties. We also discuss how the S/N of the spectra were measured and describe a test to check the covariance of the velocity dispersion measurements.

2.4.1 Redshift measurement

Among the eight lensing galaxies presented in this paper, only the redshifts of the deflectors in J0818-2613 and J1817+2729 were not previously measured. The aforementioned forward modeling method enabled us to extract the deflector spectra for both of these systems with sufficient S/N where several absorption lines such as Ca II K and H and the G-band are clearly visible after smoothing (Figures 2.4 and 2.5). The redshifts are presented in Table 2.2. The reported uncertainties are the standard deviations of the redshifts measured using several absorption lines such as CN, Ca II K and H, G band, Hβ, Hδ, Mg b etc. Our measured redshifts for the remainder of the six deflectors

Table 2.3: Measured S/N per angstrom of the extracted deflector spectra and single aperture velocity dispersion with associated statistical and systematic uncertainties. As a sanity check, SIS velocity dispersions are presented to compare with the measured velocity dispersions. The quasar redshifts and Einstein radii reported here have been used to calculate the SIS velocity dispersions. Note that, for B0445+123 and B0631+519, the source redshift is unknown. Thus a possible range of source redshift has been assumed to calculate the corresponding SIS velocity dispersion range.

Lens system	S/N per Å	Velocity dispersion (km s^{-1})	Statistical uncertainty (km s^{-1})	Systematic uncertainty (km s^{-1})	Source redshift (z_s)	Einstein radius (arcsec)	SIS vel. disp. (km s^{-1})
J0147+4630	12	283	30	12	2.377	1.886	339
B0445+123	12	136	21	13	2.0 - 3.5	0.675	198-184
B0631+519	18	147	9	10	2.0 - 3.5	0.58	190-174
J0659+1629	13	326	28	13	3.083	2.124	356
J0818-2613	7	392	46	22	2.15	2.896	472
J0924+0219	23	209	9	12	1.523	0.94	223
J1433+6007	20	261	6	7	2.74	1.581	272
J1817+2729	5	198	45	25	3.07	0.893	203

are consistent with the previously known values.

2.4.2 Velocity dispersion measurement

To achieve reliable velocity dispersion measurements, high S/N spectra are necessary. The mean S/N per angstrom for all the extracted deflector spectra except J0659+1629 were calculated using rest-frame wavelength ranges 4150–4250 Å and 4630–4760 Å. These two wavelength ranges were chosen based on the lack of any prominent absorption or telluric lines and also because none of the spectra have any emission lines or other contamination present within these ranges. However, as these rest-frame wavelength ranges were not available for the extracted deflector spectrum of J0659+1629 system, a separate rest-frame wavelength range from 3990 Å to 4090 Å was used to calculate the S/N per angstrom. The estimated S/N of the deflector spectra are reported in Table 2.3.

To measure the line-of-sight (LOS) stellar velocity dispersions of the lensing galaxies, we have

used a penalized pixel fitting method implemented through an in-house analysis pipeline VELDIS[1] which is a wrapper around the PPXF package (Cappellari & Emsellem, 2004; Cappellari, 2017). This method measures the velocity dispersion by fitting a model to the observed galaxy spectrum in pixel space. The models are created using a weighted linear combination of the broadened stellar templates to which a sum of orthogonal polynomials is added. The additive polynomials are used to adjust the continuum shape of the templates during the fit. As templates we have used the Indo-US stellar library (Valdes et al., 2004), which consists of 1273 stellar spectra covering a wavelength range of 3460 - 9464 Å with constant dispersion of 0.4 Å and FWHM resolution ~ 1.35 Å (Beifiori et al., 2011). The FWHM resolutions of the instruments used to collect our spectra have been measured by fitting Gaussian profiles to several emission lines at varying wavelengths from the corresponding sky spectra. Though the measured FWHM resolutions depend on wavelength, the range of resolutions is not significant enough to affect the velocity dispersion measurement. Thus we have adopted a constant FWHM resolution and ignored its wavelength dependence. As prescribed in Cappellari (2017), we have shifted the galaxy wavelengths and FWHM resolutions of the galaxy spectrographs to the rest frame, as the redshifts of the observed deflectors are relatively high. In the observed frame, the FWHM of all our observations was higher than that of the templates. However, Gaussian smoothing was carried out on the template spectra only if the observed FWHM was higher than the templates' after shifting to the rest frame. For all the galaxy spectra, we have masked the atmospheric A-band and B-band absorption lines, if present. Emission lines from the foreground galaxies and contaminated regions due to quasar light, if any, have also been excluded from the fit. Figures 2.3 to 2.5 show all the fits generated by PPXF. In these plots, the gray-colored spectra are the unsmoothed, logarithmically rebinned deflector spectra, the red-colored spectra are the best fit models, and the yellow-colored spectra are the smoothed versions of the original spectra. The vertical shaded regions mark the excluded part of the deflector spectra from the fitting. The green dots show the residuals between the unsmoothed flux and the model fit for each wavelength normalized to the respective model fits. Unlike the optimal extraction-based methods, the extraction technique presented in this paper and others (e.g., Goicoechea & Shalyapin, 2019; Melo et al., 2021) doesn't require defining an aperture along the spatial direction. Thus, the measured velocity dispersions correspond to the integrated velocity dispersions within a rectangular spectroscopic aperture of the

[1] https://github.com/pmozumdar/veldis

respective slit-widths and slit-lengths centered on the deflectors (see Table 2.1). After obtaining the velocity dispersion measurements from the fits, we have estimated the statistical and systematic uncertainties associated with the corresponding measurements. To determine the statistical uncertainty, we have performed three hundred Monte-Carlo simulations by adding Gaussian noise to the smoothed deflector spectra. The noise at each wavelength has been generated using normal distributions with variances equal to the variances of the corresponding galaxy spectra while ignoring the pixel-to-pixel covariances, as they are negligible compared to the respective variances. The fits are carried out with the same setup used to measure the respective velocity dispersion reported here. We measured the systematic uncertainties by conducting roughly three hundred fits while varying the wavelength range of the observed galaxy spectrum that was used for the measurement, the subset of templates, and the degree of the additive polynomials. The measured velocity dispersions of the deflectors along with the associated statistical and systematic uncertainties are reported in Table 2.3.

While fitting for the velocity dispersion, we have attempted to include as many absorption lines as possible without compromising the respective S/N of the deflector spectra. However, the S/N levels of the extracted spectra affect the measured velocity dispersions significantly. From the reported uncertainties in Table 2.3, it is clear that both the statistical and systematic uncertainty increase noticeably as the S/N levels decrease. On the contrary, both of these uncertainties improve when the S/N levels of the extracted spectra are around 20 or above, as is the case for the deflectors in the B0631+519, J0924+0219, and J1433+6007 lens system. In any case, all the extracted spectra are mostly uncontaminated by the quasar light, and the absorption features are sufficiently strong enough to conduct a velocity dispersion measurement.

We have also checked whether the velocity dispersion measurements of the deflectors vary preferentially in the same direction given the same set-up, e.g., the same rest-frame wavelength range, the same set of templates, etc. The lens system J0659+1629 has been excluded from this analysis as the extracted deflector spectrum for this system only covers a small wavelength range and thus provides almost no scope to vary the wavelength. With the rest of the deflectors, we have performed around three hundred sets of fits under different set-ups while using the same set-up for each group of seven fits corresponding to seven deflectors. The set-ups were varied by

changing the wavelength ranges, the templates used, and the degree of the additive polynomial. These measurements and how they co-vary for each pair of deflectors are shown as a corner plot in Figure 2.6. The figure also presents the heat-map of the covariance matrix calculated from these velocity dispersion measurements, where the measurements were normalized to their respective mean. From this figure, one can see that except in a few cases, there is almost no correlation among the velocity dispersion measurements of the seven deflectors. However, in those cases the off-diagonal terms in the covariance matrix are essential and can not be ignored.

2.5 Discussion

2.5.1 Comparison to previous redshift and velocity dispersion measurements

The redshifts of the six deflectors, which were previously known, match our measurements to within 1σ. Among the eight lens systems, the deflector velocity dispersions of the J0147+4630, and J1433+6007 lens systems were previously measured. For the deflector in J0147+4630, the previous measurement is 313 ± 14 km s^{-1} using a 0.5″-width slit under subarcsecond seeing conditions (Goicoechea & Shalyapin, 2019). This result is within the uncertainty of our measurement of $283 \pm 30 \pm 12$ km s^{-1} (see Table 2.3). However, using the same wavelength range (6000 - 7500 Å) as in the previous measurement, but with the setting used in this paper, we obtained a velocity dispersion value of 311 km s^{-1}. Hence, the difference between the measurements in their means may arise from the difference in the used wavelength ranges, aperture sizes and seeing conditions, etc. For the deflector in J1433+6007, the previous measurement is 216 ± 55 km s^{-1} by fitting only to Ca K line (Agnello et al., 2018). The data for this measurement was collected using a 1″ wide spectroscopic aperture under $\sim$ 1″ seeing. Our measured velocity dispersion for this deflector is $261 \pm 6 \pm 7$ km s^{-1} (see Table 2.3), which is higher but still within the uncertainty of the previous measurement.

2.5.2 Comparison to predictions from SIS lens models

The strength of the absorption lines, especially Ca II K and H, presence of 4000 Å break and the lack of emission lines in the extracted spectra confirm that the deflectors of the lens systems reported in this paper are early-type galaxies. Thus as a sanity check, we have compared measured velocity dispersion values with theoretically derived ones by assuming a singular isothermal sphere (SIS) profile for the galaxies. This mass profile is the simplest choice to predict the velocity dispersion

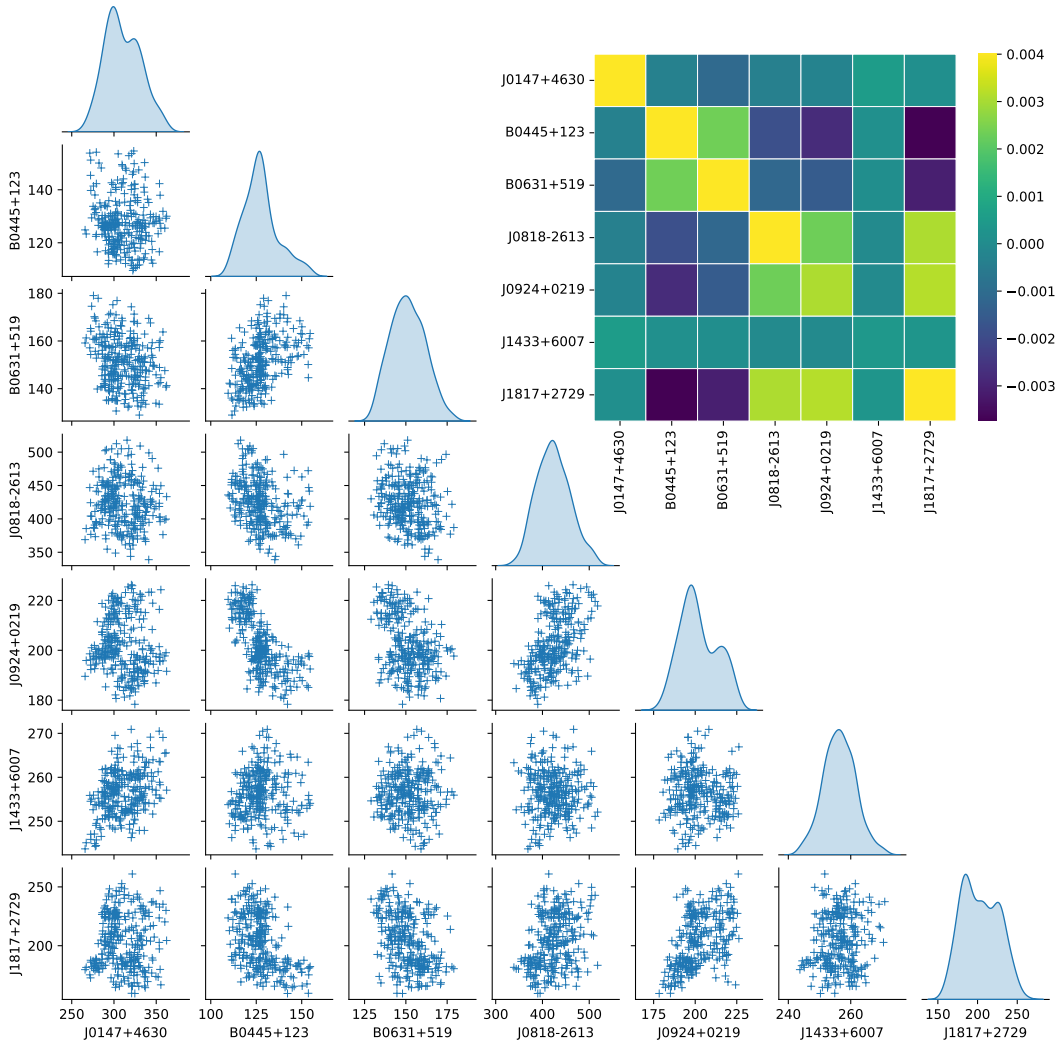


Figure 2.6: Illustration showing relations among the velocity dispersion measurements of the deflectors. The scatter plots between each pair of deflectors show corresponding velocity dispersion measurements for three hundred setups where each marker shows the measurements from the same setup. The blue-shaded curves are the individual velocity dispersion distributions of the deflectors. The set-ups were varied by changing the wavelength ranges, set of the spectra of the templates, and degree of the additive polynomial. In general, the covariance terms are negligible except in a few cases, for which they should be taken into account. The lens system J0659+1629 has been excluded from this analysis as the extracted deflector spectrum for this system only covers a small wavelength range. The plot in the upper-right shows a heat-map of the covariance matrix calculated from these velocity dispersion measurements, where the measurements were normalized to their respective mean.

using only a single lens model parameter, that is the Einstein radius. Under this assumption, the single-aperture velocity dispersion of the system $\sigma_{\rm SIS}$ can be calculated as -

$$\sigma_{\rm SIS} = \sqrt{\frac{c^2}{4\pi}\theta_{\rm E}\frac{D_{\rm s}}{D_{\rm ds}}}$$

where $\theta_{\rm E}$ is the Einstein radius in arcseconds, $D_{\rm s}$ and $D_{\rm ds}$ are the angular diameter distances between the observer and the source, and the deflector and the source, respectively, and c is the speed of light. For lens systems J0147+4630, J0659+1629, J0818-2613, J1433+6007, and J1817+2729, the mean value of Einstein radius obtained by lens modeling in Schmidt et al. (2022) was used, and for the system J0924+0219, the mean value of Einstein radius obtained by lens modeling in Chen et al. (2021a) was used. However, as detailed lens modeling for B0445+123 and B0631+519 is not available, the Einstein radius was set to half of the quasar image separation measured from AO-based images. Also, the source and deflector redshifts of these lens systems are known, except for B0445+123 and B0631+519, for which the source redshifts are still not measured. Thus, we have assumed a possible range of source redshift for these two lens systems. Using a flat ΛCDM cosmology with $H_0 = 70.0$ km s^{-1} Mpc^{-1}, $\Omega_{\rm m} = 0.3$, we have calculated the angular diameter distances and the corresponding SIS velocity dispersions of the deflectors. In our sample, all the measured velocity dispersions in their mean are lower than the corresponding SIS velocity dispersions. These offsets are due to the vast simplification of the mass distribution assumption and chosen arbitrary cosmology. The deviation of the measurements from the respective SIS predictions is within 3% - 20%, except for B0445+123. The mean and scatter of the measured to SIS velocity dispersion ratios ($\sigma_{\rm measured}/\sigma_{\rm SIS}$) are 0.87 and 0.08. This systematic overestimation of the SIS predictions may not persist for a bigger sample size. We will explore this hypothesis in the future when such a sample is available. If this trend continues, it would be possible to estimate what modifications to the assumed galaxy mass model would minimize this trend. The Einstein radii, source and deflector redshifts, and SIS velocity dispersion values are noted in Table 2.3.

2.6 Conclusion

The redshifts and velocity dispersions of the lensing galaxies are crucial data for measuring the Hubble constant using the time-delay strong lensing method. However, collecting stellar kinematics data with a high S/N is challenging from seeing limited gound-based setups as the spectra of the lensing galaxies become spatially blended with those of the often much brighter lensed quasar images. In this paper we have :

- Developed a forward modeling technique and used it to extract 1D spectra of eight lensing galaxies, even in the presence of much brighter lensed quasar images.

- Used the extracted spectra to measure the deflector redshifts in all of our targets, including two that have never been measured before, in the J0818-2613 and J1817+2729 systems. For the remainder of the targets, our measured redshifts agree with those in the literature to within 1σ.

- Made the first measurements of the stellar velocity dispersions for six of the eight lensing galaxies in our sample. The new velocity dispersion measurements were made for the deflectors in B0445+123, B0631+519, J0659+1629, J0818-2613, J0924+0219 and J1817+2729 systems.

- Checked whether there exists significant covariance among the velocity dispersion measurements of the seven deflectors. In general, we found that covariances are negliglible except in a few cases, for which they should be taken into account.

- Compared the measured velocity dispersions to those predicted by a SIS mass model as a sanity check. In our sample, all the measured velocity dispersions in their mean are lower than the corresponding SIS predictions, and the deviations of the measurements are within 3% - 20% of the respective SIS velocity dispersions except B0445+123.

The Hubble tension is one of the major unanswered questions in current physics with immense consequences, and time-delay cosmography has proved its potential to resolve this issue. Though the mass-sheet transform (MST) poses significant uncertainty in the inferred H_0 using this method, stellar kinematics such as single aperture velocity dispersion can help break this degeneracy (Birrer et al., 2020). However, to achieve percent-level precision, a sample of 40 or more time-delay lenses is required, for which we have measured integrated velocity dispersions of the deflectors to 5% or better. Even in this scenario, kinematic measurements from a sample of $\sim$ 200 nontime-delay lens systems are still necessary (Birrer & Treu, 2021). The results in this paper will help to reach this percent-level precision by adding to the current sample.

Chapter 3

A MUSE sample of early-type galaxies at intermediate redshift

3.1 Introduction

Galaxies have gone through a significant evolution over cosmic time. Understanding this evolution is integral to an understanding of structure formation, dark matter-baryonic interactions, and large-scale cosmology. One can probe this evolutionary pathway by analyzing the mass distribution and kinematics and measuring the morphological, structural, and stellar population properties of the galaxies (e.g. Naab & Ostriker, 2017). In this regard, early-type galaxies (ETG) are of particular interest as they are usually massive, and bright, contain old, passive stellar populations, and are usually free of dust allowing the collection of high-quality data even at high redshift. However, the fact that their spectra typically have only absorption lines makes this harder.

An ongoing question in the study of galaxy evolution is how massive ETGs assemble their mass as a function of redshift. Several studies, including observational surveys and hydro-dynamical simulations, have attempted to answer this question by measuring the total density slope of the underlying mass distribution of the galaxies. However, studies based on observational data used a sample covering a narrow redshift range both in the local Universe ($z \sim 0.01$) (e.g. SAURON (de Zeeuw et al., 2002), ATLAS3D (Cappellari et al., 2011), CALIFA (Sánchez et al., 2012), SAMI (Bryant et al., 2015), MaNGA (Bundy et al., 2015)) and intermediate redshift ($z \sim 1$) (e.g. Derkenne et al., 2023, 2021; Sonnenfeld et al., 2013; Bolton et al., 2012; Auger et al., 2010). Although one can compare studies done at different redshift ranges, the difference in data quality and analysis methods used in these studies may undermine the conclusion. Hence, a homogeneous study, with consistent data quality and analysis techniques for a sample gathered across a broad redshift range is necessary to draw robust conclusions. One way to investigate the mass distribution of galaxies is to

combine spatially resolved stellar kinematics information with dynamical modeling methods (e.g. Cappellari, 2008; Derkenne et al., 2021; Zhu et al., 2023). By modeling the velocity distribution of stars, we can infer the underlying gravitational potential and the contributions of different mass components. Stellar kinematics also help to determine whether a galaxy is primarily supported by rotation or by random stellar motions (dispersion), which is crucial for understanding the evolution of rotational support in ETGs—another key question in galaxy evolution (Bezanson et al., 2018). Differences in the rotational support between local and high-redshift ETGs can reveal how processes such as mergers, gas accretion, star formation, feedback, and environmental interactions have influenced the assembly history of mass and angular momentum in these galaxies. To address these questions comprehensively, it is essential to gather a statistically significant sample of ETGs at intermediate redshifts with data quality comparable to that of local ETGs. Such a sample would enable consistent and accurate comparisons, enhancing our understanding of the evolutionary processes shaping ETGs across cosmic time.

In addition to aiding in the comprehension of galaxy evolution and their halos, the stellar kinematics of massive ETGs at intermediate redshift are important for cosmological studies. A key question in astrophysics is the 5σ difference in the measured Hubble constant (H_0) using local Universe data, especially Type-Ia supernova, and the inference from cosmic microwave background radiation (CMB) data assuming a standard cosmological model (cold dark matter with a cosmological constant, ΛCDM), otherwise known as the Hubble tension (e.g. Abdalla et al., 2022; Verde et al., 2019). One independent way to measure H_0 is to use the time-delay strong lensing method (Refsdal, 1964). In this method, one can infer H_0 by combining time-delay and spectroscopic data (e.g. redshifts, stellar kinematics) from a gravitational lens system with a time-varying source and modeling the mass distribution within the lensing galaxy (deflector) using high-resolution images.(e.g., Wong et al., 2020; Millon et al., 2020b; Birrer et al., 2020). Though the mass-sheet degeneracy (MSD; Falco et al., 1985; Schneider & Sluse, 2013) and mass-anisotropy degeneracy (MAD) pose significant uncertainty in the inferred H_0 using this method, applying spatially resolved kinematics of the deflector is the key to breaking these degeneracies (Suyu et al., 2014; Birrer et al., 2020; Shajib et al., 2023). However, extracting uncontaminated and high signal-to-noise ratio (SNR) deflector spectra, and thus trustworthy stellar kinematics (both integrated and resolved), is

a challenging job due to blending of deflector and background source emission by seeing during ground-based observations, the compact nature of the lens systems, and contamination from bright lensed images (e.g., Mozumdar et al., 2023; Shajib et al., 2023). Thus, we can approach the problem differently. One can gather a sample of non-lensed galaxies, thus eliminating the above challenge, from the same redshift and integral velocity dispersion range as the time-delay cosmography grade lensing galaxies. The extracted resolved kinematics data from these galaxies can be used to understand the global anisotropy in this sample at the population level. This acquired knowledge can be incorporated as an informed prior in the Bayesian hierarchical framework of H_0 inference and thus utilized to break mass-anisotropy degeneracy indirectly.

To accomplish these goals, one requires a sample of massive ETGs with high-quality data favorable to extracting resolved stellar kinematics up to a few effective radii. The ESO archival data observed with the Multi-Unit Spectroscopic Explorer (MUSE) provides a significant source of integral field unit (IFU) data with high signal-to-noise ratios (SNRs) for non-lensed massive ETGs. The MUSE-DEEP[1] collection combines observed data from single or multiple MUSE programs at specific sky locations into a single IFU datacube, achieving very high effective exposure such as $\sim$ 80 hr (Table 3.1). Utilizing this high-SNR data, I compiled a sample of ETGs within the redshift range of 0.25-0.75 with resolved stellar kinematics extending to several effective radii. In this chapter, I have introduced this sample, described the data extraction process, and presented measurements of their kinematic, morphological, and stellar population properties. In subsequent chapters, I used this data, along with Hubble Space Telescope (HST) observations, to probe the degree of rotational support in high-redshift ETGs and compare it with their local counterparts. I also performed Jeans dynamical modeling to understand galaxy properties, especially the total density slope and anisotropy, their evolution, and possible environmental effects. Additionally, I will conduct a Bayesian hierarchical analysis to derive a posterior of the anisotropic parameter. Throughout this work, I assume a flat ΛCDM cosmology with $H_0 = 70.0$ km s^{-1} Mpc^{-1}and $\Omega_{\rm m} = 0.3$ when necessary. These parameters are quite close to the values derived by the Planck satellite (Planck Collaboration et al., 2020), within the systematic uncertainties discussed later.

[1]https://doi.org/10.18727/archive/42

This chapter is organized as follows. In section 3.2, I described how the sample was selected from the archival MUSE-DEEP datacubes. I presented the kinematics extraction process in section 3.3.1, and photometry in section 3.3.2. In section 3.4, I discussed the data analysis methods used in this work to measure the structural, kinematic, and global population properties of individual galaxies. I reported trends observed in the measured galaxy properties of the sample, compared them with the respective observations from the local Universe, and discussed implications in section 3.5. Finally, I summarised the chapter in section 3.6.

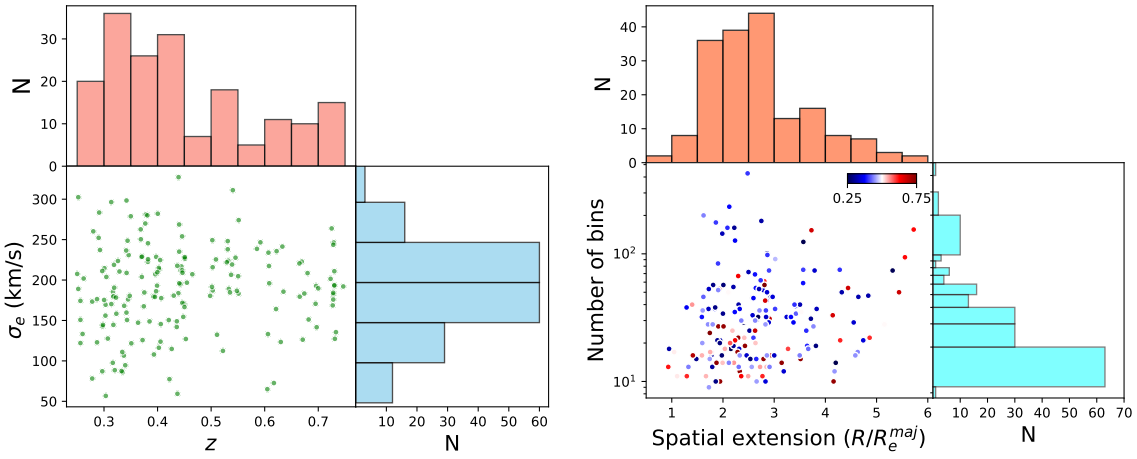


Figure 3.1: Distribution of MUSE sample properties. Left: Distribution of galaxies in the (σ, z) plane. The redshifts and integrated velocity dispersion, σ, were measured using the corresponding central spectra of the galaxies. Individual central spectrum was created by co-adding all the spectra from spaxels within approximately one effective radius, R_e. Right: Distribution of galaxies in the plane of the spatial extension of the extracted resolved stellar kinematics data in units of R_e^{maj}, and number of Voronoi bins with a target SNR 12. R_e^{maj} is the semi-major axis of the elliptical half-light isophote of the galaxy. The number of bins and the associated histogram are plotted in a log scale and the color map shows the galaxy redshifts.

3.2 MUSE sample selection

MUSE is an integral-field spectrograph located at the Very Large Telescope (VLT) of the European Southern Observatory (ESO). This spectrograph provides a spatial resolution of 0.2″ over a 1′× 1′ field-of-view (FOV) in the wide-field mode (Bacon et al., 2010). The covered wavelength range is 4800-9300 Å with 1.25 Å spectral pixel. To gather a comprehensive sample of massive ETGs at intermediate redshift ($0.25 < z < 0.8$) observed by MUSE, I started by manually checking all MUSE-DEEP IFU datacubes publicly accessible in the ESO Science Archive Facility[2] (European

[2]https://archive.eso.org/scienceportal/home

Southern Observatory (ESO), 2017). The datacubes with at least 4-6 early-type galaxies at $z > 0.25$ were chosen for further inspection, narrowing the number of potential datacubes of interest to 40. From these datacubes, I selected 264 individual galaxies after a detailed examination. While manually selecting those galaxies by eye, I emphasized two criteria. First, a galaxy should be sufficiently isolated, and if it is part of a galaxy cluster or group it should be further away from the center to ensure the measured stellar kinematics and surface brightnesses would have minimum contamination from surrounding galaxies at similar redshift. A galaxy was considered sufficiently isolated if no other galaxy lies within a radius of 2-3 arcseconds. Second, the projected image of the galaxy in the sky plane must be spatially big enough ($> 2''$along the major axis) to extract resolved stellar kinematics up to a few effective radii. Whenever possible, the selected galaxies in a cluster or field were identified using redshifts from published catalogs (see Table 3.2).

From these 264 galaxies, I further excluded 84 galaxies because either they did not have publicly available images collected by the HST, and/or had fewer than 10 Voronoi bins at our chosen SNR. I described the latter criterion in the next section. Table 3.1 contains relevant information about the datacubes from which the final 180 galaxies were selected, and Table 3.2 provides information about the publicly available archival HST images and relevant catalogs used for this sample. The coordinates of these 180 galaxies, IDs associated with them, redshifts, and other relevant information are listed in Table 3.3. For almost all galaxies, I used images taken using the F814W filter, except for a few cases where the F555W or F606W filters were used. In Fig. 3.1, the distribution of the galaxies in the integral velocity dispersion-redshift plane is shown. This figure also shows the kinematic extension of the galaxies along with the number of bins at a chosen high SNR. Though the redshift bin from 0.3-0.35 has the maximum number of galaxies, other redshift bins still have a statistically comparable number of galaxies.

3.3 Data reduction

The following section describes how 2D stellar kinematics maps for individual galaxies were extracted from the MUSE-DEEP datacubes. It also includes a brief overview of how HST images were used to model the surface brightness of each galaxy. These surface brightness models were used to measure the structural properties of the galaxies.

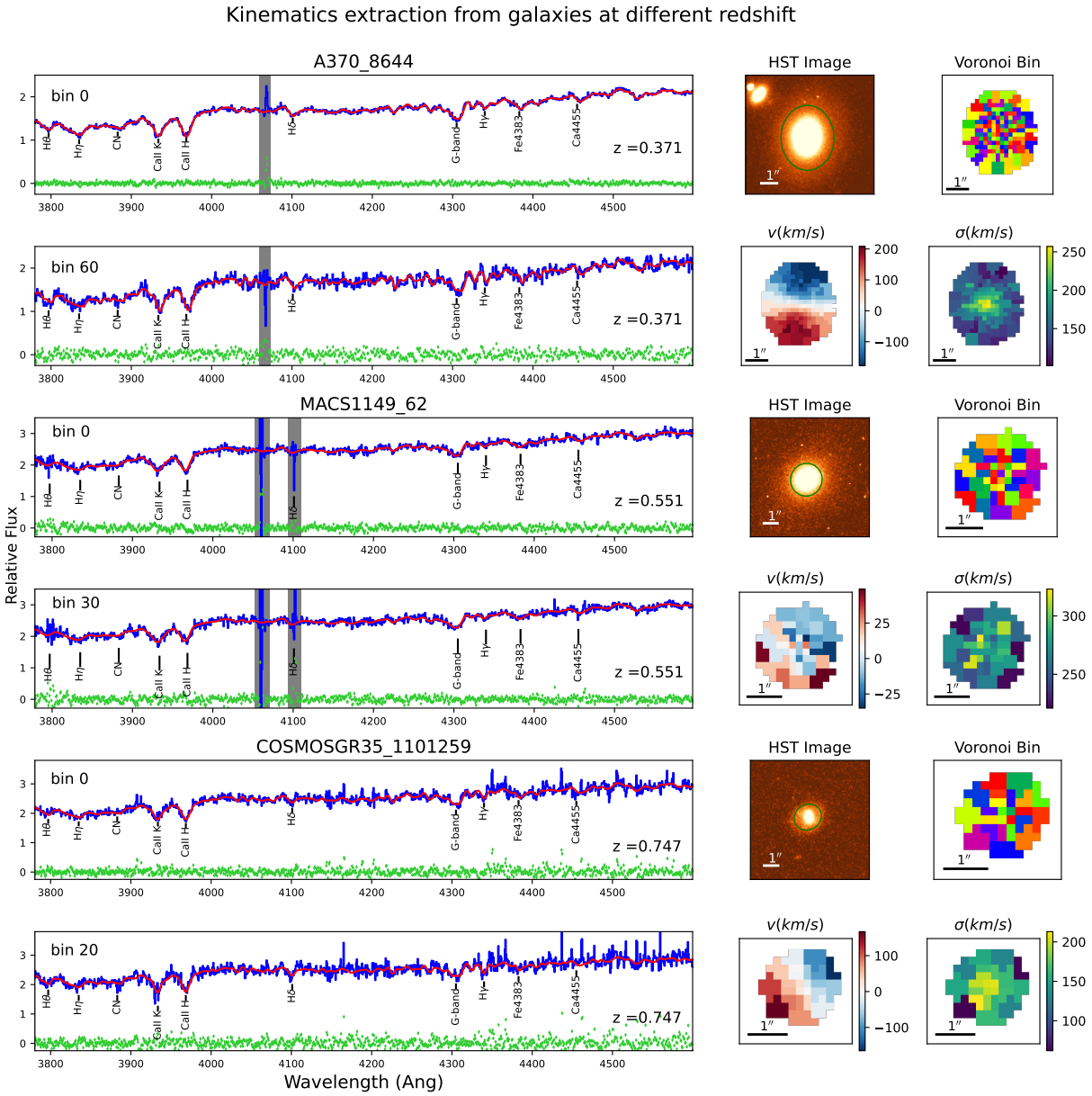


Figure 3.2: Example of kinematics extraction from galaxies at different redshifts. The galaxies are A370_8644 ($z = 0.371$, top), MACS1149_62 ($z = 0.551$, middle) and COSMOSGR35_1101259 ($z = 0.747$, bottom). In each case, two extracted spectra (blue) from two different Voronoi bins, one close to the galaxy center and the other close to the edge, are shown with kinematic fitting from PPXF (red). The green markers are residuals between data and the fitted model at each wavelength and the gray regions mark the excluded wavelength range from fitting. Additionally, for each galaxy, the HST image, 2D map of the Voronoi binning of the spaxels at target SNR 12, and extracted velocity (median subtracted) and velocity dispersion maps are also depicted. The green circle in each HST image shows the extension of the extracted kinematic data relative to the observed surface brightness.

Table 3.1: Information related to the data cubes used in this work such as ESO archive ID, program ID, effective exposure, galaxy cluster or field within the cube, and number of galaxies collected from the cube are listed in the table.

Cluster/Field	ESO data ID	MUSE Program ID	Effective exp. (sec)	Num. of galaxies
AS1063	ADP.2017-03-28T12:46:01.331	095.A-0653(A)	15885.0	6
A1835	ADP.2019-01-02T09:51:36.335	097.A-0909(A)	11178.0	9
A2744	ADP.2017-03-24T12:14:09.100	MULTI	16345.0	13
A2895	ADP.2019-10-18T09:34:16.487	MULTI	16134.0	1
A370	ADP.2017-06-06T13:13:38.674	MULTI	13655.0	17
BULLET	ADP.2017-03-24T12:23:57.159	094.A-0115(B)	6766.0	5
CLJ1449	ADP.2022-08-31T14:19:53.687	105.20C9.001	27780.0	2
COSMOSGR28	ADP.2017-03-24T15:17:56.787	MULTI	22709.0	3
COSMOSGR32	ADP.2018-04-13T08:06:56.375	MULTI	13650.0	7
COSMOSGR32	ADP.2019-01-02T10:06:51.914	0101.A-0282(A)	10645.0	2
COSMOSGR35	ADP.2019-10-07T09:42:38.927	MULTI	14503.0	3
COSMOSGR83	ADP.2017-03-24T15:17:56.840	MULTI	20413.0	3
COSMOSGR84	ADP.2019-09-02T08:03:16.118	0102.A-0327(A)	12302.0	3
COSMOSGR172	ADP.2019-10-07T09:42:38.959	0103.A-0563(A)	14553.0	1
HE0238	ADP.2017-03-24T13:24:09.645	MULTI	24675.0	3
HUDF	ADP.2017-03-24T13:59:14.977	MULTI	31844.0	2
HUDF	ADP.2017-03-24T13:59:14.871	MULTI	29993.0	1
HUDF	ADP.2019-11-20T14:57:13.894	1101.A-0127(A)	321693.0	4
LAB1	ADP.2017-03-28T12:26:19.431	095.A-0570(A)	12417.0	1
MACS0257	ADP.2019-11-25T09:40:00.922	MULTI	21304.0	7
MACS0416	ADP.2019-10-09T11:36:01.797	0100.A-0763(A)	39545.0	11
MACS0416	ADP.2017-03-24T16:19:17.624	094.A-0525(A)	36113.0	5
MACS0940	ADP.2019-01-02T09:02:39.474	MULTI	21695.0	10
MACS1149	ADP.2017-03-24T16:26:09.634	294.A-5032(A)	15282.0	8
MACS1206	ADP.2017-06-19T11:32:26.411	MULTI	17478.0	16
MACS2129	ADP.2017-03-27T15:26:07.717	095.A-0525(A)	8802.0	3
MACS2214	ADP.2020-03-30T10:35:44.574	MULTI	23976.0	5
MS0451	ADP.2017-06-07T07:24:11.988	096.A-0105(A)	8478.0	6
NGC1052	ADP.2018-12-20T09:53:26.537	MULTI	16138.0	1
RXJ1347	ADP.2019-01-02T09:51:36.307	097.A-0909(A)	8526.0	8
RXJ2129	ADP.2017-12-14T12:30:03.217	097.A-0909(A)	11444.0	1
RXS0437	ADP.2021-04-29T08:02:29.347	106.21AD.001	7711.0	7
SDSSJ1029	ADP.2019-08-30T07:41:35.874	0102.A-0642(A)	13387.0	2
SMACS2131	ADP.2019-11-25T09:40:00.887	MULTI	22784.0	6

Table 3.2: Information about archival HST images and the catalogs used in this work. All images are available at the Mikulski Archive for Space Telescopes (MAST). The catalogs were used to identify galaxies in the MUSE IFU white and HST images.

Cluster/ Field	Proposal ID	PI	Observation date	Total Exp. (sec)	Filter	Catalog ref.
A1835	11591	J. R. Kneib	2010-06-26	4840.0	F814W	
A1835	15661	A. M. McDonald	2019-05-08	2430.0	F555W	
A2744	13495	J. Lotz	2014-07-01	5044.0	F814W	Mahler et al. (2018)
A2895	10881	G. Smith	2006-08-23	1200.0	F606W	
A370	14038	J. Lotz	2016-01-20	5146.0	F814W	Lagattuta et al. (2019)
A1063	14037	J. Lotz	2015-10-18	5046.0	F814W	Tortorelli et al. (2018)
Bullet	11591	J. R. Kneib	2011-02-18	4480.0	F814W	Richard et al. (2021)
CLJ1449	12991	V. Strazzullo	2013-05-20	700.0	F606W	
COSMOSGR28	9822	N. Z. Scoville	2004-04-18	2028.0	F814W	Weaver et al. (2022)
COSMOSGR32	9822	N. Z. Scoville	2004-05-03	2028.0	F814W	Weaver et al. (2022)
COSMOSGR35	9822	N. Z. Scoville	2004-05-09	2028.0	F814W	Weaver et al. (2022)
COSMOSGR83	9822	N. Z. Scoville	2003-11-25	2028.0	F814W	Weaver et al. (2022)
COSMOSGR84	9822	N. Z. Scoville	2004-05-08	2028.0	F814W	Weaver et al. (2022)
COSMOSGR172	9822	N. Z. Scoville	2004-04-16	2028.0	F814W	Weaver et al. (2022)
HE0238	14660	L. Straka	2017-06-19	2182.0	F814W	
HUDF	11563	G. D. Illingworth	2010-02-09	5332.0	F814W	Inami et al. (2017)
MACS0257	12166	H. Ebeling	2011-06-16	1440.0	F814W	Richard et al. (2021)
MACS0416	13496	J. Lotz	2014-01-07	5246.0	F814W	Vanzella et al. (2021)
MACS0940	15696	D. Carton	2019-05-18	7526.0	F814W	Richard et al. (2021)
MACS1149	13790	S. Rodney	2014-12-22	5308.0	F814W	Tortorelli et al. (2018)
MACS1206	12069	M. Postman	2011-05-25	1091.0	F814W	Richard et al. (2021)
MACS2129	9722	H. Ebeling	2003-09-11	4530.0	F814W	Jauzac et al. (2021)
MACS2214	9722	H. Ebeling	2003-10-29	4560.0	F814W	Richard et al. (2021)
MACS0451	11591	J. R. Kneib	2011-02-07	4880.0	F814W	Jauzac et al. (2021)
NGC1052	15851	P. V. Dokkum	2020-09-15	2080.0	F814W	
RXJ1347	10492	T. Erben	2006-03-10	5280.0	F814W	Richard et al. (2021)
RXS0437	16670	H. Ebeling	2021-11-21	1200.0	F814W	
SDSSJ1029	12195	M. Oguri	2011-05-15	5276.0	F814W	
SGASJ2111	11974	S. S. Allam	2009-04-14	1100.0	F814W	
SMACS2131	12166	H. Ebeling	2011-05-03	1440.0	F814W	Richard et al. (2021)

3.3.1 Stellar kinematics

The MUSE-DEEP collection provides reduced 3D data and associated variance data cubes. The data are reduced using the MUSE data reduction pipeline (Weilbacher et al., 2020). This pipeline[3] removes the instrument signature, performs sky-correction and then resamples and combines all the relevant data into a single cube. From the original deep datacubes, I extracted a smaller individual cube for each galaxy using the MUSE Python Data Analysis Framework (MPDAF) (Bacon et al., 2016). Next, I executed the following steps on the individual datacube of each galaxy. A central spectrum was created by co-adding the spectra from all spaxels within 1 effective radius (R_e). The R_e was measured using the white image comprised from the datacube utilizing the 'FLUX_RADIUS' function available at the python implementation for Source Extraction and Photometry (SEP) (Barbary, 2016) package. In this work, I adopted a single rest-frame wavelength range from 3780-4600 Å for all kinematic analysis to ensure that galaxies from different redshifts contain the same absorption features such as CN, Ca II K and H, and G band, etc while avoiding overlapping with strong skylines after 8000 Å. Thus, all spectra were trimmed to this rest-frame wavelength range. The central spectrum was then used to check redshift and measure integrated line-of-sight (LOS) stellar velocity,V, and velocity dispersion σ_e.

To accomplish this task and subsequent kinematic analysis, I used a penalized pixel fitting method implemented through the pPXF package[4] (Cappellari & Emsellem, 2004; Cappellari, 2017, 2023). This method measures stellar kinematics by fitting a model to the observed galaxy spectrum in pixel space. The models are created using a weighted linear combination of the broadened stellar templates to which a sum of orthogonal polynomials is added. The additive polynomials are used to adjust the continuum shape of the templates during the fit. We have included an additive polynomial of degree 2 in the models for all kinematic extractions. The Indo-US stellar library[5] (Valdes et al., 2004), which consists of 1273 stellar spectra covering a wavelength range of 3460 – 9464 Å with a constant spectral scale of 0.4 Å/pixel and FWHM resolution ~ 1.35 Å (Beifiori et al., 2011) was used for the templates. The wavelengths and instrumental FWHM resolutions of the galaxies have been shifted to the rest frame as prescribed in Cappellari (2017). Though the

[3]For more details check https://www.eso.org/rm/api/v1/public/releaseDescriptions/102

[4]I used pPXF Python package v9.2 from https://pypi.org/project/ppxf/

[5]Avaliable from https://noirlab.edu/science/observing-noirlab/observing-kitt-peak/telescope-and-instrument-documentation/cflib

FWHM resolution of MUSE depends on wavelength, it does not vary enough within the adopted wavelength range to affect the kinematic measurements. Therefore, I used a constant FWHM resolution of 2.5 Å (Guérou et al., 2017). As the rest framed instrumental FWHM resolution of all the galaxies was higher than that of the templates, a Gaussian smoothing was carried out on the template spectra. The FWHM of the Gaussian kernel used to broaden the templates was set to $\mathrm{FWHM}^2_{\mathrm{diff}} = \mathrm{FWHM}^2_{\mathrm{MUSE}} - \mathrm{FWHM}^2_{\mathrm{temp}}$, the quadratic difference between the redshift-corrected FWHM resolution of MUSE for the respective galaxy and the template.

I masked skylines, emission features, and gap regions in the spectra, if present, to exclude them from the fit. The same regions were also masked while measuring resolved kinematics. The global template set for each galaxy was created by comprising the templates used while fitting the central spectrum to measure integrated velocity dispersion. Fig. 3.1 shows the measured integrated velocity dispersions of the MUSE galaxies with associated redshifts. This central spectrum was also used to study global stellar population properties such as age, chemical composition, mass-to-light ratio, etc., and the global template set was later used to measure resolved kinematics.

Next, I created a 2D SNR map of the galaxy by measuring the median SNR of the spectrum in each spaxel of the cube within the restframe wavelength range 3990-4090 Å. Using this SNR map, a region was selected around the center of a galaxy, where the median SNR is 2.5 or above. However, in some cases, this SNR threshold was set below 2.5, otherwise the selected region would have been too small for extracting resolved kinematics. This selected region was then Voronoi binned[6] (Cappellari & Copin, 2003) at a target SNR of 12 per bin. This ensures the spaxels within the selected region would be grouped spatially so that the SNR in each bin would be close to or higher than the chosen target SNR. At this point, those galaxies with fewer than 10 bins were excluded from the sample. I implemented the criteria of target SNR and minimum bin number to enhance the reliability of the constraints on the model parameters derived using resolved kinematics data.

The distribution of the MUSE sample in terms of the number of Voronoi bins and spatial extension (in units of R_e^{maj}) is also shown in the right subplot of Fig. 3.1. The associated color map in this plot provides redshifts of the galaxies. The resolved kinematics of the galaxies were measured up to these spatial extensions. From the associated histograms in this plot, it is apparent that around two-thirds of the total sample has more than 20 bins and a kinematic extension between

[6]We used the VorBin Python package v3.1 from https://pypi.org/project/vorbin/

1 R_e^{maj} and 3 R_e^{maj}. The data in the spaxels were coadded according to the derived Voronoi binned map into a single spectrum per bin. Then the above-mentioned setting was used to measure stellar velocity and velocity dispersion from each Voronoi binned spectrum, resulting in a velocity and velocity dispersion map for each galaxy. However, this time the global template set, measured before, was used instead of the total template library. This makes the measured kinematics more robust in the lower-S/N bins of a galaxy. Examples of pPXF fitting to spectra from three galaxies at different redshifts and the resulting kinematics map are shown in Fig 3.2. This figure also shows fits to spectra from different bins of the same galaxy.

3.3.2 Photometry

From the HST images covering the same sky location as the MUSE-DEEP cubes, individual images were cut out for the target galaxies. These cut-out images typically cover a FOV of 100–225 arcsec^2 with target galaxies at the center and ample background region to measure sky contribution. I estimated the background level by fitting a Gaussian to the histogram of the photon count in the image, excluding the target galaxy and other luminous objects. The mean of the fitted Gaussian was adopted as the background level and the standard deviation was used as a criterion to differentiate the galaxy contribution from that of the background. The sky-subtracted images were then used to model the surface brightness of the galaxies using a series of 2D Gaussian profiles implemented by the python package Multi-Gaussian Expansion fitting of galactic images (MgeFit[7]) (Cappellari, 2002). The MGE models were used to measure structural properties such as ellipticities, ϵ, semimajor axes, R_e^{maj}, and effective radii, R_e, etc., within the elliptical half-light isophotes of the galaxies.

3.4 Data analysis

This section discusses the measurement methods of different structural, kinematic, and morphological galaxy properties using the extracted stellar kinematics and photometry data. First, I describe how the galaxy ellipticity, effective radii, and a proxy for angular momentum, λ_R, etc., were measured. After that, I explain the stellar population synthesis methods used to determine the age, metallicity, mass-to-light ratio, and stellar mass of each galaxy.

[7]We used the MgeFit Python package v5.0 from https://pypi.org/project/mgefit/

3.4.1 Measuring size and ellipticity

I used the MGE models of the galaxy surface brightness to measure ellipticity, defined as $\epsilon = 1-b/a$, semi-major axis, R_e^{maj} and circularized effective radius, R_e. These quantities were measured within the elliptical isophote covering half of the total observed light. Here, the circularized effective radius satisfies $\pi R_e^2 = A$, where A is the area of the elliptical half-light isophote. The 'MGE_HALF_LIGHT_ISOPHOTE' function from the python package[8] Jeans Anisotropic Modelling (JAM) for Galactic Dynamics (Cappellari, 2008) has been used for this purpose. This function creates a synthetic galaxy image using the MGE model (only for one quadrant due to symmetry) and measures the light enclosed within a grid of isophotes along the MGE major axis. Then it finds the isophote containing half of the analytic MGE total light using linear interpolation. The structural properties were measured within this isophote (for details see Cappellari et al., 2013b, sec. 3.3.1). Throughout the paper, I used R_e^{maj} as the physical size estimate of a galaxy as it follows the light profile of the galaxy more accurately than R_e.

The photometric position angle (PA) of a galaxy was measured directly from the sky-subtracted HST image using the FIND_GALAXY routine in the MGEFIT package. This function uses the weighted first and second moments of the intensity distribution of a region of connected pixels to compute the galaxy center and PA. However, the measured PA may vary based on the number of pixels used because the galaxy shape may change from rounder to flatter going outwards. Here we utilized all the pixels employed in measuring the kinematic maps of each galaxy. The number of pixels was provided to the routine as a fraction of the total pixels in the image using the 'fraction' keyword.

3.4.2 Measuring kinematic properties

The resolved stellar kinematics enable us to measure important galaxy properties such as the angular momentum and position angle of the major axis. These properties are essential to distinguish between regular and non-regular rotators. Regular rotators are those galaxies that exhibit ordered rotational motion with a well-defined rotational axis and their velocity fields typically resemble a "butterfly pattern" when mapped (e.g. galaxy A370_8644 in Fig. 3.2). Contrarily, non-regular rotators do not exhibit a smooth, ordered rotational motion, and their velocity fields show more

[8] I used JamPy Python package v7.2 from https://pypi.org/project/jampy/

complex and disordered kinematic features (e.g. galaxy MACS1149_62 in Fig. 3.2). Such kinematic classification improves our understanding of galaxy formation pathways, merger, and assembly history, and the environmental effects on redshift evolution (see review in Cappellari, 2016). Here I present the methods employed to measure these kinematic parameters.

3.4.2.1 Proxy for galaxy angular momentum

As an approximation to galaxy angular momentum, I used a luminosity-weighted quantity λ_R (Emsellem et al., 2007) defined as

$$\lambda_R = \frac{\langle R|V|\rangle}{\left\langle R\sqrt{V^2+\sigma^2}\right\rangle} = \frac{\sum_{i=0}^{N} F_i R_i \,|V_i|}{\sum_{i=0}^{N} F_i R_i \sqrt{V_i^2+\sigma_i^2}}, \tag{3.1}$$

where V_i is the stellar velocity, σ_i is the velocity dispersion, R_i is the distance from the galaxy center, and F_i is the total flux of a spaxel within the adopted aperture. For V_i and σ_i, I used the velocity and velocity dispersion of the Voronoi bin to which the spaxel belongs. I summed over all the spaxels within an ellipse with a semi-major axis of 2 R_e^{maj} and ellipticity, ϵ (measured at 1 R_e^{maj}). I found that an elliptical aperture with a semi-major axis of 1 R_e^{maj} contains less than 20% of the total spaxels within the 2D kinematics map, for 70% of our sample galaxies. However, for the adopted bigger aperture, this happens only for 10% of the total galaxies. Note that for the galaxies that do not extend beyond 2 R_e^{maj}, all the spaxels have been used in measuring λ_R. An in-depth comparison between λ_R measurements within 1 and $2R_e$, from high-quality CALIFA IFS data, was presented in Falcón-Barroso et al. (2019). They found that, for fast rotator galaxies, $\lambda_{2Re} \approx 1.19\lambda_{Re}$. I also observed that λ_R increases with a bigger aperture. On average λ_R increased by 0.07 with a standard deviation of 0.06, when I used a $2R_e^{maj}$ aperture compared to 1 R_e^{maj} aperture.

3.4.2.2 Kinematic major axis

We measured the global kinematic PA of each MUSE galaxy using 2D velocity maps of the stars using the FIT_KINEMATIC_PA function from the PAFIT package[9]. This function implements the algorithm described in Appendix C of Krajnović et al. (2006). Briefly, the routine generates a number of bi(anti)-symmetric velocity maps with different angles. In these models, the velocity of the light-weighted centroid coordinate of a Voronoi bin is set to the weighted average of the data

[9]We used the PaFit Python package v2.0 from `https://pypi.org/project/pafit/`

from four quadrants such that

$$V'(x,y) = \frac{V(x,y) + V(x,-y) - V(-x,y) - V(-x,-y)}{4} \tag{3.2}$$

where V′ is the model velocity field, V is the observed velocity field and the x-axis is along the chosen angle. The best-fitting position angle, PA_{kin} is determined by minimizing the χ^2 difference between the model and the observed velocity field. The kinematic misalignment is then defined as, $PA_{kin} - PA_{phot}$.

3.4.3 Measuring stellar population

The mass assembly and chemical enrichment histories are a key part of the galaxy evolution process, and stellar population synthesis (SPS) could help decode this information about a galaxy. One way to conduct this stellar population synthesis is to perform full spectral fitting using templates from different SPS models. In this section, I discuss how the global stellar population properties were extracted from integrated spectra within 1 R_e using PPXF.

3.4.3.1 SPS models

I used two independent SPS models to check the sensitivity of the results to the adopted model assumptions. These two models were selected because they include templates down to a young age of 1 Myr which are needed to reproduce actively star-forming galaxies if present in our sample. The SPS models used in this work are - (i) **Flexible Stellar Population Synthesis (FSPS)** [10](Conroy et al., 2009; Conroy & Gunn, 2010), and (ii) **GaLAXEV**[11] (Bruzual & Charlot, 2003).

In all cases, the same age grid was used where each element in the grid was logarithmically spaced by 0.1 dex from 1 Myr to 15.85 Gyr, defined as

$$\lg(\mathrm{Age/yr}) = 6, 6.1, 6.2, \ldots, 10.2$$

In our adopted standard cosmology the age of the Universe is 6.9 − 10.5 Gyr between $z = 0.75$ and 0.25. However, the models were allowed to extend beyond this physical age range, to check the ability of the data to retrieve the galaxy ages. Also, no constraint was imposed on metallicity. Following Cappellari (2023), I used the below setups for the two SPS models:

[10]https://github.com/cconroy20/fsps
[11]http://www.bruzual.org/bc03/

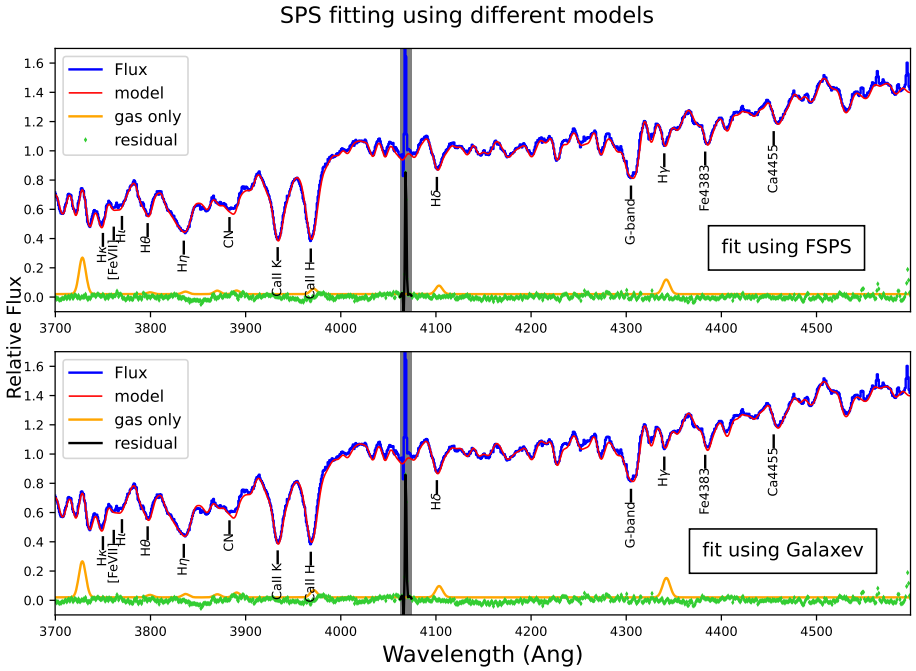


Figure 3.3: SPS fitting from PPXF. Top: Fitting was done using FSPS templates. Bottom: Fitting was performed using GaLAXEV templates. In both cases, the blue curve shows the observed galaxy spectrum from A370_8644 (z=0.371), the red curve is the best-fitting model (stellar continuum + gas) from PPXF, the orange curve is the best-fitting gas-only spectrum, and the green diamonds are the residuals. The grey-shaded regions were masked and excluded from fitting.

(i) Using the FSPS model, a total of 387 SPS templates was created with the above age grid and 9 equally-spaced metallicities $[Z/H] = [-1.75, -1.5, -1.25, -1.0, -0.75, -0.5, -0.25, 0.0, 0.25]$. A Salpeter (1955) IMF with a mass range of 0.08 - 100 $M_\odot$ was adopted along with MIST isochrones (Choi et al., 2016) and default values for the other parameters. The effect of gas or dust was excluded while computing the spectra. The model produces SPS spectra using the MILES stellar library (Sánchez-Blázquez et al., 2006; Falcón-Barroso et al., 2011) in the optical region.

(ii) The GALAXEV model was used to generate a set of 215 template spectra with the same age grid as above and 5 metallicities $[Z/H] = [-1.74, -0.73, -0.42, 0.0, 0.47]$. A Salpeter IMF and Padova isochrones (Girardi et al., 2000; Marigo et al., 2008) were used. This model also uses the MILES library to produce the templates at the optical region.

3.4.3.2 Fitting procedure

To analyze the global properties of the stellar population of a galaxy, I fitted the SPS templates to the integrated central spectrum within the half-light ellipse of the galaxy using PPXF. I performed the SPS fitting separately from the kinematic one, as a different setup was used for each. However,

I used the same central spectra (described in subsection 3.3.1) covering rest-frame wavelength range 3700-4800 Å. The fitting procedure consists of several steps. First, the galaxy spectrum was log-rebinned along with the noise. The SPS templates were also log-rebinned at the same velocity scale as the galaxy spectra and smoothed to account for the lower instrumental resolution of the galaxy spectra. The FWHM of the Gaussian kernel used to smooth the templates was set to the difference between the rest-framed FWHM of the galaxy and that of templates as described in subsection 3.3.1. The template spectra were then normalized using the total bolometric flux of the corresponding template spectra measured over the adopted rest-frame wavelength range. Next, a set of gas emission lines was prepared to fit with the stellar continuum. The emission lines that fall within the chosen rest-frame wavelength range are: Balmer series bluer than Hβ, the [OII] $\lambda\lambda$3726, 29 and [NeIII] $\lambda\lambda$3868, 69 doublets. Additionally, the Balmer series were tied to be fitted as a single gas template and the ratio of the [OII] doublets was set as per atomic physics.

Finally, the PPXF fitting was performed in two steps. Initially, an unregularized fit ('regul'= 0) was done to rescale the log-rebinned noise spectrum such that the reduced χ^2 value became 1. Then another fitting was conducted with the rescaled noise spectrum and a smaller amount of regularization ('regul'= 10) applicable only to stellar components. This small amount of regularization was introduced to reduce the noise present in the SPS models[12]. During both fittings, the kinematics of all the gas lines were constrained to be the same and reddening was imposed on gas templates using the extinction curve of Calzetti et al. (2000). In contrast to kinematic fitting, I used multiplicative polynomials ('mdegree' = 2) instead of additive ones as they account for spectral flux calibration issues and reddening effects. Additionally, I masked skylines, emission features, and gap regions in the spectra, if present, to exclude them from the fit. An example of SPS fittings to a galaxy spectrum with two different template sets was illustrated in Fig. 3.3.

3.4.3.3 Measuring average stellar population

The PPXF fitting for each galaxy with the SPS templates described above provides the weights of best-fitting stellar and gas templates over the 2D age-metallicity grid. Considering only the weights of the stellar templates the luminosity weighted (as the templates were already normalized by their total bolometric luminosity) population quantities, e.g. age and metallicity, can be calculated by

[12]See Cappellari (2023) for more discussion on the effects of regularization on SPS fitting.

summing the best-fitting template weights such that

$$\begin{aligned} \langle \lg \ \mathrm{Age} \rangle &= \frac{\sum_j w_j \times \lg \mathrm{Age}_j}{\sum_j w_j} \\ \langle [Z/H] \rangle &= \frac{\sum_j w_j \times [Z/H]_j}{\sum_j w_j} \end{aligned} \tag{3.3}$$

where w_j is the best-fitting weight at the j th grid point. These equations were implemented using the 'MEAN_AGE_METAL' function of the 'SPS_UTIL' module of PPXF. The stellar mass-to-light ratio is defined as

$$M_*/L = \frac{\sum_j m_j M_{*,j}}{\sum_j m_j L_j}, \tag{3.4}$$

where $M_{*,j}$ is the stellar mass and m_j is the corresponding mass-weight and L_j is the corresponding luminosity measured in the observed HST band at the redshift of the galaxy. The mass weights are calculated from the best-fitting template weights. This calculation of the stellar mass-to-light ratio, M_*/L, was done by the PPXF.SPS_UTIL.MASS_TO_LIGHT routine with the 'redshift' keyword set to the galaxy redshift. This M_*/L only includes the mass of living stars and stellar remnants, but excludes the gas lost during stellar evolution.

To measure the stellar mass, M_*, I first computed the total luminosity of the galaxy and then multiplied it by previously estimated M_*/L. Note that the $M_{*,j}$ and L_j quantities in the previous paragraph (see equation 3.4) are the mass and luminosity of the jth stellar population template. I computed the total luminosity of each galaxy from the corrected surface brightness. The corrections were applied in the following way. First, the surface brightness of the MGE models was converted to AB magnitudes and treated for extinction effects. Then the surface brightness was multiplied by $(1+z)^3$, with z being the galaxy redshift, to account for both the $(1+z)^4$ bolometric cosmological dimming and the redshifting of the bandpass in the AB system. As the MUSE galaxies are at significant redshift, I also applied K-correction (see Hogg et al., 2002, for details). The K-correction relates the observed photometry at a particular bandpass to its intrinsic value at the rest-frame bandpass. For the K-correction, I used the luminosity measured from the redshifted solar spectrum in the same HST band as the observed galaxy. The 'MAG_SUN' function from the 'SPS_UTIL' module of the PPXF package was utilized for this step where the redshift was set to the galaxy z.

Table 3.3: This table presents the galaxy ID, coordinates, redshift, and other measured kinematic, structural, and stellar population properties for a subset of MUSE galaxies.

Cluster/ Field	ID	RA (J2000)	Dec (J2000)	z	σ_e km s^{-1}	R_e (kpc)	R_e^{maj} (kpc)	ϵ	λ_R	$\lg(\frac{M_*}{M_\odot})$	$\lg(\frac{(M_*/L)}{M_\odot/L_\odot})$	$< lgAge >$ (yr)	$[Z/H]$
A1063	39	342.18417	-44.52633	0.351	122.0	1.35	1.67	0.33	0.25	10.66	0.63	9.66	-0.4
A1063	45	342.18553	-44.51814	0.344	249.0	1.39	2.03	0.5	0.2	11.1	0.67	9.62	0.21
A1063	58	342.18822	-44.52539	0.35	279.0	0.86	1.25	0.52	0.19	11.0	0.73	9.54	0.24
A1063	78	342.19344	-44.51728	0.342	298.0	0.89	1.32	0.54	0.17	11.01	0.68	9.67	0.22
A1063	79	342.1934	-44.52586	0.345	176.0	0.97	1.47	0.5	0.19	10.73	0.66	9.65	-0.19
A1063	85	342.19562	-44.52544	0.346	231.0	2.28	2.62	0.25	0.05	11.24	0.67	9.69	0.1
A1835	1	210.26795	2.8916	0.262	202.0	2.08	2.31	0.19	0.13	10.47	0.65	9.63	0.08
A1835	10	210.25743	2.86452	0.256	122.0	2.15	3.64	0.63	0.48	10.84	0.5	9.56	-0.3
A1835	11	210.25496	2.87005	0.26	133.0	2.25	2.75	0.32	0.33	10.87	0.63	9.82	-0.23
A1835	12	210.25549	2.86174	0.252	189.0	2.17	2.42	0.19	0.3	11.03	0.69	9.81	0.05
A1835	3	210.26261	2.87913	0.252	302.0	2.3	3.33	0.41	0.36	11.4	0.66	9.66	0.25
A1835	4	210.25226	2.8823	0.25	208.0	0.52	0.88	0.65	0.33	10.55	0.68	9.78	0.17
A1835	7	210.26308	2.87182	0.256	174.0	2.07	2.34	0.2	0.15	10.77	0.58	9.51	0.01
A1835	9	210.25949	2.87613	0.256	151.0	1.34	1.59	0.27	0.2	10.6	0.7	9.24	-0.38
A2744	10314	3.59038	-30.39099	0.297	143.0	1.18	1.45	0.35	0.3	10.81	0.7	9.9	-0.28
A2744	10478	3.57154	-30.39046	0.297	87.0	3.02	3.39	0.21	0.25	10.73	0.55	9.66	-0.06
A2744	10689	3.59489	-30.39171	0.301	215.0	4.96	5.55	0.2	0.1	11.51	0.64	9.73	-0.05

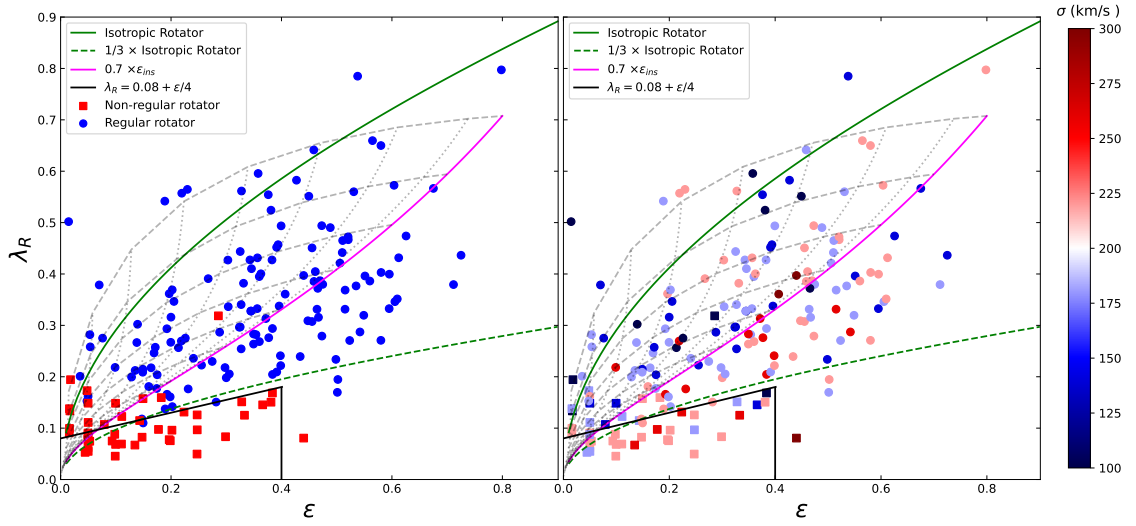


Figure 3.4: 2D distribution in (λ_R, ϵ). λ_R was measured using equation 1 and and ϵ is the observed ellipticity derived from MGE models. The circle and square markers correspond to visually classified (using V map) regular and non-regular rotators. The solid green line is the predicted theoretical relation for an edge-on ($i = 90°$) isotropic rotator (Cappellari, 2016, equation 14) and the dashed green line represents one-third of that (Emsellem et al. (2007) used this line to differentiate between regular and non-regular rotators). The magenta line shows a theoretical upper limit on global anisotropy, $\beta = 0.7\epsilon_{\rm ins}$, provided the intrinsic shape of the galaxy from an edge-on view (Cappellari, 2016, equation 11), and the grey dotted lines show how the magenta line changes with different inclinations ($\Delta i = 10°$), while the grey dashed lines show how the galaxies move across the diagram with changing inclination, ($\Delta i = 10°$), and for a set of given intrinsic ellipticity values ($\Delta\epsilon_{\rm ins} = 0.1$). The black solid lines defined by $\lambda_{R_e} < 0.08 + \varepsilon/4$ and $\varepsilon < 0.4$ (Cappellari, 2016, equation 19) separates non-regular rotators from regular rotators. Left Panel: The red and blue colors denote non-regular and regular rotators respectively, and in general confirm our visual classification. Right Panel: The galaxies are plotted in (ϵ, λ_R) plane with their integrated velocity dispersion indicated by the color map.

3.5 Results and discussions

3.5.1 λ_R confirms visual kinematic classification

In Fig. 3.4, I plot the measured λ_R vs ϵ with the corresponding visual kinematic classification of the galaxies (regular or non-regular rotators). When mapped, the observed velocity fields of regular rotators typically resemble a 'butterfly pattern'. In contrast, the velocity fields of non-regular rotators lack this pattern and display disordered kinematic features. I observed that regular rotators have higher λ_R values than the non-regular ones. This trend was also found in low redshift galaxies, (Cappellari, 2016; Graham et al., 2018). This confirms that regular rotators at intermediate redshifts are also predominately supported by ordered rotational motion while

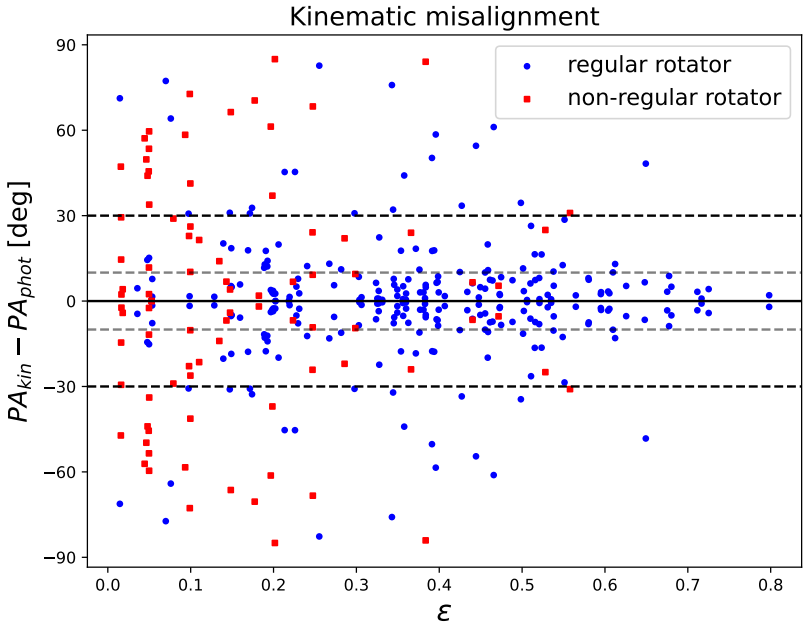


Figure 3.5: Misalignment between kinematic and photometric PAs as a function of ϵ. PAs of the photometric major axis, $PA_{\rm phot}$, were measured using the sky-subtracted HST images, and PAs of the kinematic major axis, $PA_{\rm kin}$ were measured from the observed velocity maps. The blue circles denote visually identified regular rotators and the red squares show the non-regular rotators. The plot is symmetrized about the black solid line along 0° to eliminate any indication of bias towards positive or negative misalignments. The dashed lines show ±10°, 30° misalignments. Similar to local Universe (see Fig. 6 in Cappellari, 2016), most of the fast rotators in MUSE sample also show < 10° misalignment between $PA_{\rm phot}$ and $PA_{\rm kin}$.

the non-regular ones are with random motions. Cappellari (2016) proposed the black solid line defined by $\left(\lambda_{R_{\rm e}} < 0.08 + \varepsilon/4, \varepsilon < 0.4\right)$ to separate non-regular rotators from regular rotators while Emsellem et al. (2007) used the green dashed line. Except in a few cases, my visual classification is in concordance with these two classification schemes. The majority of galaxies that are visually classified as regular rotators stay above the green dashed line and black solid line while the non-regular rotators lie below those two lines. In most cases, the regular rotators that are below the green dashed line, were from those 10% galaxies for which the selected 2 R_e^{maj} aperture contains less than 20% of the total spaxels used to measure the 2D kinematics map. This emphasizes our choice of aperture to measure reliable λ_R.

Fig. 3.4 also shows the position of the MUSE galaxies in the (ϵ, λ_R) plane with their respective velocity dispersion, σ. As expected, non-regular rotators in general have higher σ than the regular rotators. I found that $\sim$ 60% of the visually classified non-regular rotators have $\sigma > 200$ km s^{-1}

while only ∼ 40% of the regular rotators have such high σ.

3.5.2 Kinematic misalignment

The misalignment between kinematic and photometric PA for galaxies in the MUSE sample is illustrated in Fig. 3.5. The plot is symmetrized about the horizontal line along 0° to eliminate any indication of bias towards positive or negative misalignment. There is a strong presence of visually classified regular galaxies centered around 0° (black solid line). This relatively small misalignment has also been observed for low redshift regular ETGs (Cappellari, 2016; Graham et al., 2018, e.g.). Using a sample from MANGA survey Graham et al. (2018) found that 70.0% of regular ETGs and 56.3 % of spiral galaxies are aligned within ±10°. However, I found that only 60.0% of the regular galaxies have misalignment below |10°|. Given the small sample size, it is hard to evaluate whether this discrepancy happened due to poor accuracy, as I am dealing with objects from comparably larger distances, or it is a feature of high-redshift regular galaxies. If I only consider regular galaxies with misalignment within ±30°, then ∼ 71% of the regular galaxies were found aligned within ±10°.

3.5.3 Global stellar population properties

In Fig. 3.6, I present the distribution of global stellar population properties such as age, metallicity, [Z/H] and the stellar mass-to-light ratio, (M_*/L) on the mass-size (M_* - R_e^{maj}) plane derived from analysis with two different SPS models. The galaxy semi-major axis within half-light elliptical isophote, R_e^{maj} was measured from MGE models (see section 3.4.1), and stellar mass, M_* was measured by multiplying the estimated M_*/L with total luminosity (see section 3.4.3.3). For Fig. 3.6 and 3.7, the measured properties were LOESS smoothed to achieve color-coded values using the 2D 'Locally Weighted Regression' algorithm by Cleveland & Devlin 1988 implemented in the LOESS package (Cappellari et al., 2013a). A smoothing parameter frac = 0.5 was used for these plots. The LOESS-smoothed plots help to illustrate the overall trend present in the sample rather than showing the exact distribution of the measured quantities. This figure shows the well-known fact that stellar ages, metallicities, and mass-to-light ratios approximately follow lines of constant stellar velocity dispersion. This trend is observed in galaxies both in the local Universe (see Fig. 8 in Lu et al. (2023) for the MaNGA sample) and at intermediate redshift (see Fig. 11 in Cappellari (2023) for the LEGA-C sample). For our sample, this trend is most clearly visible for the mass-

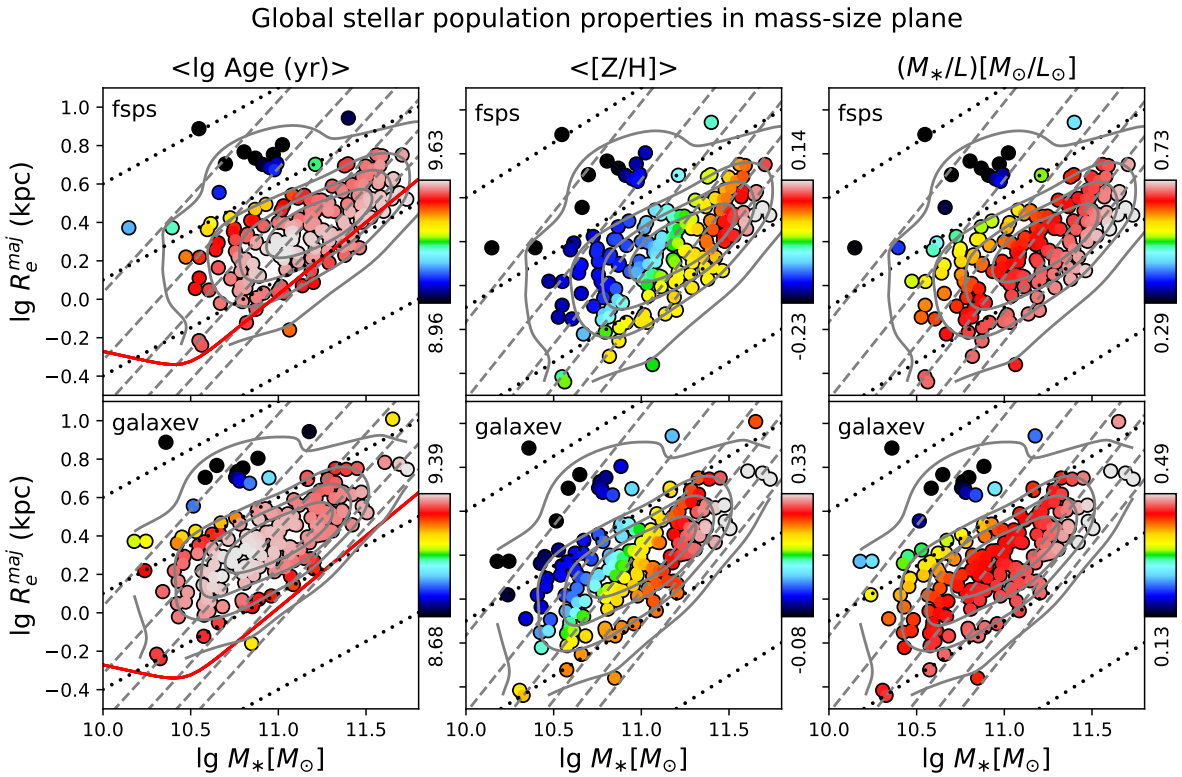


Figure 3.6: Age, metallicity and (M_*/L) estimates from SPS models in the mass-size plane. Distributions of luminosity-weighted and LOESS-smoothed age (left panel), metallicity, [Z/H] (middle panel), and stellar mass-to-light ratio, (M_*/L) (right panel) on the mass–size plane (lg R_e^{maj} vs lg M_*). The galaxy semi-major axis within half-light elliptical isophote, R_e^{maj} was measured from MGE models (see section 3.4.1), and stellar mass, M_* was measured by multiplying estimated M_*/L with total luminosity (see section 3.4.3.3). The top panel shows results from SPS analysis with FSPS templates and the bottom with GALAXEV templates. In each panel, the gray dashed lines indicate the lines of constant σ_e for 100, 150, 200, 250, 300 and 350 kms^{-1} from left to right and the black dotted lines are for constant surface mass density, $\Sigma_e = 10^8, 10^9, 10^{10}, 10^{11}$ M$_\odot$ kpc^{-2} from top to bottom. A kernel density estimate of the galaxy number density is also indicated by the grey contour lines.

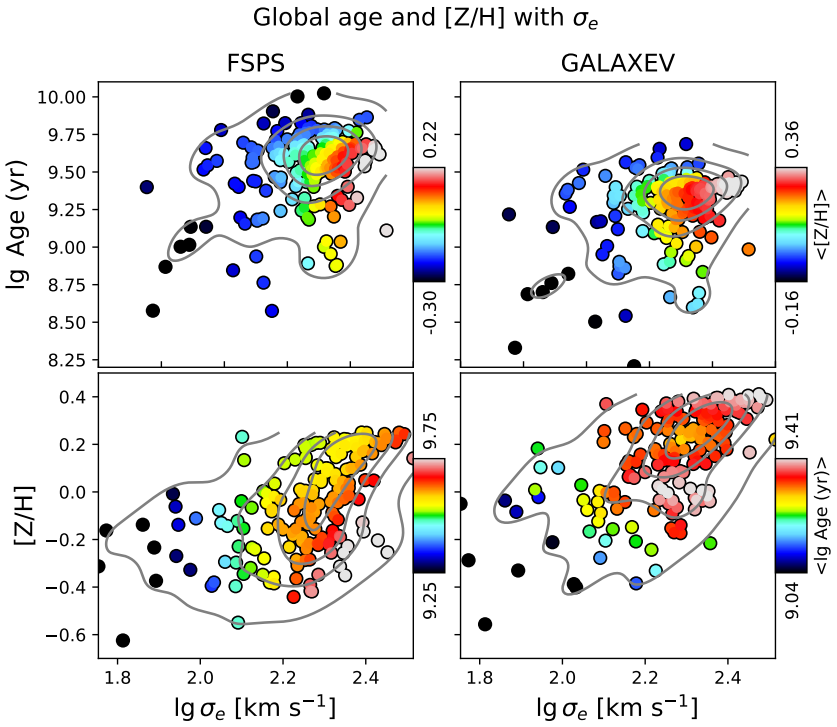


Figure 3.7: Age and metallicity from different SPS models with σ_e. The top panel shows the distribution of luminosity-weighted and LOESS-smoothed age on the (σ_e, [Z/H]) plane, and the bottom panel shows the distribution of the luminosity-weighted and LOESS-smoothed global metallicity, [Z/H] on the (σ_e, age) plane, from SPS analysis with two different template sets. In both rows, the left column shows results from fitting with FSPS templates and the right from GALAXEV templates. In each plot, a kernel density estimation of the galaxy number density is indicated by the grey contours.

to-light ratios, where the M_*/L increases with increasing σ_e for both SPS models, with almost negligible dependence on stellar mass or size. Similarly, a galaxy with higher (lower) σ_e is more metal-rich (metal-poor). However, for $\sigma_e > 200$ km/s, the mass and size also seem to play a role in determining [Z/H] for both of our models. This is also true for the LEGA-C sample at a median redshift of 0.8. The expected dependency of stellar ages on σ_e seems to be washed out for both models. This could happen due to over-smoothing or small sample size and not representative of the actual distribution of the measured ages.

Fig. 3.7 again illustrates the dependence of luminosity-weighted age and metallicity on σ_e in our sample. For both models, galaxies with an older population are more metal-rich than galaxies containing a younger population at constant σ_e, with overall lower metallicities for galaxies with smaller σ_e. However, this trend is more prominently recovered in the FSPS model than in the GalAXEV. Both the MaNGA galaxies at lower redshift (see fig. 6 in Lu et al. (2023)) and the

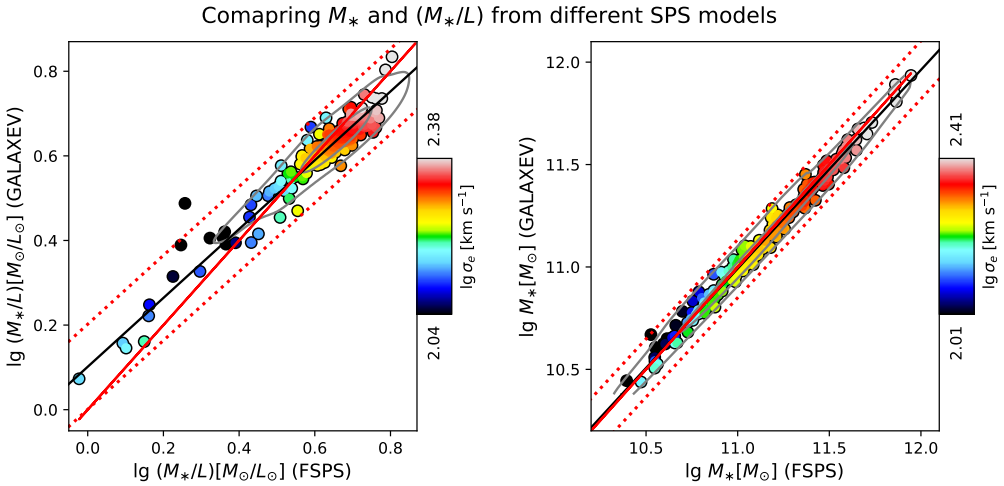


Figure 3.8: Comparing LOESS-smoothed stellar mass, M_* (right panel) and mass-to-light ratio, M_*/L (left panel) from two different SPS models with color-coded velocity dispersion, σ_e. In both plots, the black line denotes the best-fit line and the red dotted lines show the selection region of galaxies for fitting. The coefficients of the best-fit lines were measured using the LtsFit python package (Cappellari et al., 2013b). The red line shows the one-to-one relation between the measurements from different SPS models. A kernel density estimate of the galaxy number density is also indicated by the grey contour lines. In the case of M_*/L, the one-to-one line deviates significantly from the best-fit line. We have to shift the estimates from the Galaxev model, both M_* and M_*/L, by 0.2 dex to bring them close to the one-to-one relation. As expected, both M_* and M_*/L estimates from each model increase with σ_e.

LEGA-C sample at high redshift also show this trend (see fig. 12 in Cappellari (2023)).

In Fig. 3.8, I compare LOESS-smoothed stellar mass, M_* (right panel), and mass-to-light ratio, M_*/L (left panel) from two different SPS models color-coded with corresponding velocity dispersion. As expected, both M_* and M_*/L from each model increase with σ_e. The stellar mass estimates exhibit a tighter correlation than the mass-to-light ratios. However, we have to add a shift of 0.2 dex to the estimates from the Galaxev model, for both M_* and M_*/L, to bring them close to the one-to-one relation (red lines in the plot). I have not investigated the source of this systematic bias as it is out of the scope of this paper.

In general, the patterns in the results are consistent between the FSPS and GALAXEV models with more galaxies with slightly younger ages and higher metallicities from the GaLAXEV model than FSPS. The SPS analysis using these two models on both the LEGA-C and MaNGA samples has also demonstrated similar patterns in age and metallicity. This highlights the importance of not relying on a single SPS model. Further studies would be required to investigate the reason for the different behavior of the two models. Overall, Fig. 3.7 and 3.6 confirm the quality of these global

results.

3.6 Conclusion

Galaxy evolution is an active field of study with many open questions, such as the assembly history of mass and angular momentum in early-type galaxies over cosmic time. While large surveys have provided valuable insights into local early-type galaxies, similar studies are still needed for galaxies at intermediate redshifts. One key limitation is the availability of a statistically large sample with high-quality data. In this work, I aimed to overcome this challenge by gathering a sample of 180 galaxies at redshifts $0.25 < z < 0.75$. Utilizing MUSE-DEEP cubes, I extracted resolved kinematics of these galaxies up to a few effective radii. This high signal-to-noise ratio data enabled us to measure various kinematic, morphological, and stellar population properties of the galaxies. From these measurements, I observed global trends in early-type galaxies at intermediate redshifts and compared them with their local counterparts.

I found that regular rotators have higher λ_R values than non-regular ones, confirming that regular rotators at intermediate redshifts are supported by ordered motion, while non-regular rotators are supported by random motions. A similar trend has also been observed in the low redshift galaxies. For most galaxies, the measured λ_R was in concordance with the visual classification from the extracted kinematics map. I also observed that non-regular rotators generally have higher velocity dispersion, σ, with $\sim 60\%$ having $\sigma > 200$ km s^{-1} compared to $\sim 40\%$ of regular rotators.

I also evaluated the kinematic misalignment of these galaxies by measuring the kinematic PA from the extracted velocity map and comparing it with the photometric PA measured using HST images. I observed that 60.0% of visually classified regular galaxies have kinematic-photometric position angle misalignment below $|10^\circ|$, which is lower than the 70.0% observed for regular ETGs in the MANGA survey. However, it is hard to distinguish whether this discrepancy is due to our small sample size or the greater distances of our objects.

This study also illustrates that stellar population properties of this sample such as age, metallicity ([Z/H]), and mass-to-light ratio (M_*/L) have a strong correlation with stellar velocity dispersion (σ_e). As is the case for early-type galaxies from the local Universe, the age, [Z/H], and M_*/L of these galaxies also follow lines of constant σ_e on the mass-size plane. For our sample, this trend is most evident in the mass-to-light ratios, where M_*/L increases with rising σ_e and shows

almost no dependence on stellar mass or size. I observed that for both models, galaxies with an older population are more metal-rich than galaxies containing a younger population at constant σ_e and overall metallicities increase with higher σ_e. Both MaNGA at low-redshift and LEGA-C sample at intermediate redshift have shown similar results. Similarly, M_*/L and M_* increase with σ_e. Though in most cases the two SPS models (FSPS and GalAXEV), qualitatively produced consistent patterns, the stellar mass from the GalAXEV model showed a systematic shift. Overall, these results, consistent with previous studies, emphasize the reliability of our findings and highlight the need for continued use of diverse SPS models to account for systematic biases.

The measured galaxy properties and extracted kinematics of this sample will be used to explore two key questions in galaxy evolution. First, by using λ_R, I will evaluate the degree of rotational support in early-type galaxies at intermediate redshifts relative to local galaxies. Second, utilizing kinematic maps and MGE models from HST photometry, I will measure the total density slope of the underlying mass distribution in this sample and investigate whether there is any evolution in the total density slope as a function of redshift. Additionally, the results from this sample can help address other key questions in galaxy formation and large-scale cosmology.

Chapter 4

Early-type galaxies exhibit increased rotational support at intermediate redshift

4.1 Introduction

Galaxies are primarily supported by either rotation (V) or by random stellar motions, also known as dispersion (σ). Understanding which of these processes is dominant, and whether or how this dominance has shifted over cosmic time, provides critical insights into the formation histories and subsequent evolution of galaxies. Investigating these questions involves comparing the rotational support in galaxies from both the local and distant Universe (e.g. Bezanson et al., 2018). In this context, early-type galaxies (ETGs) are of particular interest as they are usually massive and bright, contain old, passive stellar populations, and are typically free of dust. These characteristics allow the collection of high-quality data even at high redshift, facilitating the study of their rotational support despite their lack of emission lines. Although emission-line spectra can be obtained relatively quickly, making spirals easier to study as well.

Observations from local massive galaxies, predominantly ETGs, suggest that even the so-called "fast-rotators" exhibit significant dispersion support (e.g. Emsellem et al., 2007, 2011). In contrast, various studies at high redshift (z $\sim$ 2) found that massive galaxies show significant rotational support (e.g. van Dokkum et al., 2015; Wisnioski et al., 2015; Belli et al., 2017) . This discrepancy demands a substantial change in rotational support over cosmic time, but the mechanisms driving this evolution remain unclear. Bezanson et al. (2018) compared the V/σ ratio, a proxy for measuring rotational support, of 104 quiescent galaxies ($0.6 < z < 1.0$) from the Large Early Galaxy Astrophysics Census (LEGA-C) spectroscopic survey (van der Wel et al.,

2016) to a sample of 91 low-redshift ETGs ($0.005 < z < 0.03$) from the Calar Alto Legacy Integral Field Area (CALIFA) survey (Sánchez et al., 2012), and found evidence of decrease in rotational support at low redshift. However, they used slit spectroscopy to measure the velocity and velocity dispersion profiles for the LEGA-C galaxies, while for the CALIFA sample, they processed the integral-field-unit (IFU) data by rebinning and smoothing it to estimate comparable 1D profiles. With the advent of high-quality IFU data for a substantial sample of ETGs at intermediate redshifts, it is now imperative to revisit this question.

The ESO archival data obtained using the Multi-Unit Spectroscopic Explorer (MUSE) provides a substantial source of IFU data with high signal-to-noise ratios (SNRs) for non-lensed massive ETGs. The MUSE-DEEP collection[1] consolidates observations from single or multiple MUSE programs at specific sky locations into a single IFU datacube, achieving very high effective exposure times. This setup maximizes data depth and SNR, enabling the extraction of resolved stellar kinematics up to several effective radii. Leveraging this high-quality dataset, I assembled a sample of massive ETGs spanning a redshift range of $z = 0.25$-0.75. In this work, I used this sample to understand the level of rotational support in ETGs at intermediate redshifts and compared them with local ETGs to reassess the decline in rotational support over cosmic time. For comparison, I utilized a set of ETGs from the Mapping Nearby Galaxies at Apache Point Observatory (MaNGA) survey (Bundy et al., 2015) as a reference sample from the local Universe. Galaxy properties pertinent to this analysis such as a proxy for angular momentum λ_R (Emsellem et al., 2011) for the MaNGA sample have been previously documented in the literature (Zhu et al., 2023; Lu et al., 2023, hereafter DynPop I and II respectively). I used the same tools and techniques to measure similar galaxy properties as in DynPop I and II, thereby minimizing the potential for systematic biases in one set of measurements or the other.

In this chapter, I briefly describe the MUSE sample and relevant data products in section 4.2. In section 4.3, I introduce the MaNGA survey and data products, detailing the methodology used to measure the galaxy properties of the MaNGA sample, and discussing how a MaNGA ETG sample was selected to statistically match the MUSE ETG sample. The methodology for correcting the observed λ_R of the MUSE sample is explained in section 4.4. I present the results, highlighting the differences in rotational support between intermediate-redshift and local ETGs in section 4.5.

[1] https://doi.org/10.18727/archive/42

In section 4.6, I discuss several tests performed to reinforce this analysis. Finally, I summarize the conclusions in section 4.7. Throughout this study, I assume a flat ΛCDM cosmology with $H_0 = 70.0$ km s^{-1} Mpc^{-1}and $\Omega_m = 0.3$ when necessary.

4.2 MUSE sample and data products

The selection of the MUSE sample, the data extraction process, and the measurement of various kinematic and morphological properties have been discussed extensively in Chapter 3. Here, I provide a summary of those detailed descriptions.

4.2.1 MUSE sample selection and kinematics extraction

MUSE, an integral-field spectrograph, situated at the Very Large Telescope (VLT) of the European Southern Observatory (ESO), provides a spatial sampling of 0.2″across a $1'^2$ field-of-view (FOV) in its wide-field mode(Bacon et al., 2010). It operates within a wavelength range of λ = 4800-9300 Å with a spectral resolution of 1.25 Å per pixel. Utilizing MUSE-DEEP datacubes from the ESO Science Archive, we identified 264 galaxies and extracted individual data cubes for each of them. We selected galaxies based on criteria such as isolation to minimize contamination and adequate size for extracting resolved stellar kinematics up to several effective radii. Isolation was determined by ensuring no other galaxies were within a few arcseconds of the target galaxy, which could affect measurements. From the initial sample of 264 galaxies, 84 were excluded either because a publicly available Hubble Space Telescope (HST) image of the galaxy was lacking or because the kinematics map did not have sufficient Voronoi bins at the desired SNR. This process resulted in a final sample of 180 galaxies for analysis.

The MUSE-DEEP dataset, processed using the MUSE data reduction pipeline (Weilbacher et al., 2020), provides reduced 3D data and variance cubes for each galaxy. From these IFU data, integrated stellar kinematics were derived by fitting central spectra within an aperture of one effective radius (R_e). All kinematic fittings were performed utilizing the pPXF package (Cappellari, 2017) with templates from the Indo-US stellar library (Valdes et al., 2004). A fixed restframe wavelength range of λ = 3990-4090 Å was used across different redshifts for consistent absorption feature analysis. To extract resolved kinematics, first, a 2D SNR map was created for each galaxy. These SNR maps were used to select a coherent central region for each galaxy which is Voronoi binned to ensure a target SNR of 12 per bin. At this step, I excluded galaxies with fewer

than 10 bins for reliable kinematic measurements. HST images were utilized to model the surface brightness of the galaxies using Multi-Gaussian Expansion fitting (MgeFit) (Cappellari, 2002).

4.2.2 MUSE data products

In Chapter 3, I provided a catalog of the MUSE sample containing several morphological, kinematic, and stellar population properties. However, for this analysis, only four of them: integrated velocity dispersion $\sigma_{\rm e}$, ellipticity ϵ, a proxy for stellar angular momentum λ_R and stellar mass M_*, are required. For the details of the measurement process please check Chapter 3. Note that the measurement process of the above-mentioned properties of the MUSE sample are same as the MaNGA sample, and both employed the same tools and techniques.

4.3 Reference MaNGA local sample

In the following sections, I first describe the MaNGA survey and data products, and the methodology to measure the galaxy properties of the MaNGA sample used in this analysis. Then I discuss how a MaNGA ETG sample was selected to statistically match the MUSE ETG sample.

4.3.1 MaNGA survey and kinematics data

The MaNGA survey (Bundy et al., 2015) offers spatially resolved spectral measurements for around 10000 nearby galaxies in the redshift range $0.01 < z < 0.15$. The observation covers a spatial range of up to 1.5 R_e for the primary sample (66% of total galaxies) and 2.5 R_e for the secondary sample (33% of the total galaxies) which are at higher redshift (Wake et al., 2017). The MaNGA spectra cover a wavelength range of λ = 3600-10000 Å with a spectral resolution of $R \approx 2000$ that corresponds to σ = 72 km s^{-1} (Law et al., 2016). The data cubes were extracted from spectrophotometrically calibrated raw data using the MaNGA data reduction pipeline (Law et al., 2016). To measure stellar kinematic maps of the galaxies, the data cubes were Voronoi binned at a target SNR of 10 and fitted using the pPXF python package. These steps were performed with the official MaNGA data analysis pipeline (Westfall et al., 2019, DAP).

4.3.2 Structural and stellar properties of MaNGA sample

The comprehensive dataset provided by the MaNGA survey has been extensively studied in the MaNGA Dynamics and Stellar Population (DynPop) series papers. The first paper of this series (DynPop I) provides catalogs of dynamical and structural properties for 10296 galaxies from the

MaNGA survey (Zhu et al., 2023) and the second paper (DynPop II) provides stellar populations properties of this sample (Lu et al., 2023). For the MaNGA sample, I used the measured galaxy properties from these two papers. I collected the integrated velocity dispersion σ_{Re}, a proxy for stellar angular momentum λ_{R_e} and the ellipticity ϵ from DynPop I[2], and gathered stellar mass M_* from DynPop II[3]. Here I briefly describe the measurement process for the above-mentioned galaxy properties:

(i) The integrated velocity dispersion $\sigma_{\rm e}$ was calculated as the square root of the luminosity-weighted average of the line-of-sight (LOS) velocity and velocity dispersion of the Voronoi bins within an elliptical aperture of area $A = \pi R_e^2$ such that

$$\sigma_{\rm e} = \sqrt{\frac{\sum_i F_i (V_i^2 + \sigma_i^2)}{\sum_i F_i}} \tag{4.1}$$

where V_i and σ_i are the velocity and velocity dispersion in the i th Voronoi bin, respectively, and F_i is the total flux in that bin. R_e is the circularized effective radius of the elliptical half-light isophote. The V_i, σ_i, and F_i are products of the MaNGA DAP.

(ii) The ellipticities ϵ of the galaxies within the half-light isophote were measured similarly as in this paper. The SDSS r-band images were used to create MGE models with the MGEfit software and then fitted with the 'MGE_HALF_LIGHT_ISOPHOTE' function from the JAMPY software. This fitting also returned the R_e mentioned above.

(iii) The proxy for stellar angular momentum λ_{R_e} within the half-light ellipse was calculated following equation 3.1. The observed values were then corrected for PSF effects to obtain intrinsic ones following equation 5 of Graham et al. (2018). For this purpose, the SDSS r-band PSF FWHM values were adopted from the catalogue[4] provided by the MaNGA collaboration. This necessitates a similar treatment to the observed λ_R of the MUSE galaxies. I applied such a PSF correction to the MUSE sample in section 4.4.

(iv) The global stellar mass M_* was measured following

$$M_* = (M_*/L)_{SPS}(< R_e) \times L \tag{4.2}$$

where $(M_*/L)_{SPS}(< R_e)$ is the SDSS r-band stellar mass-to-light ratio derived by fitting an integrated spectrum from all spaxels within the elliptical half-light isophote, and L is the r-band total

[2]https://zenodo.org/records/8381999

[3]https://github.com/manga-dynpop/manga-dynpop.github.io/tree/main/catalogs/JAM

[4]https://www.sdss.org/dr17/manga/manga-data/data-access/

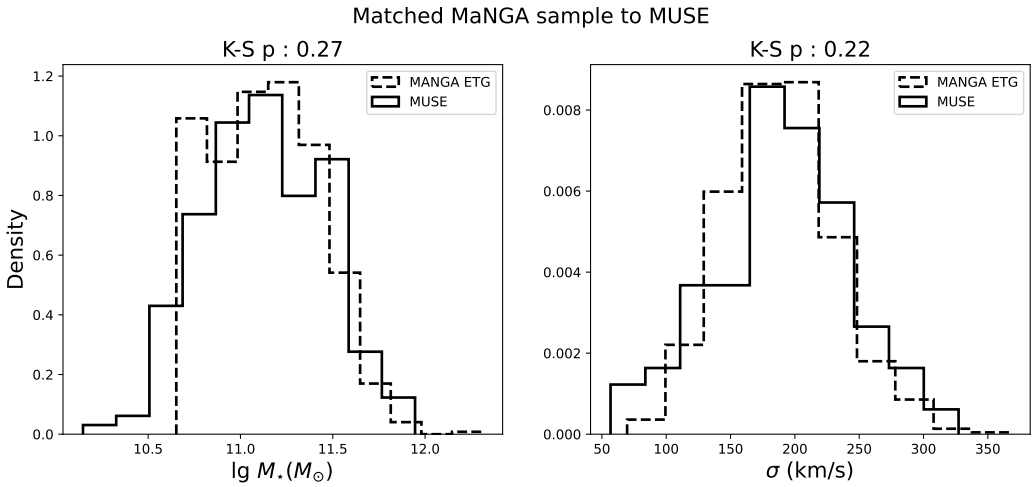


Figure 4.1: The number density histograms of the statistically matched MaNGA ETG sample (dashed line) and MUSE sample (solid line). Left: Histograms for stellar mass, log M_*. For both samples, the stellar mass was measured from SPS fitting using pPXF with templates from the FSPS model (check section 3.4.3.3 and 4.3.2). A mass cut of log $M_*(M_\odot) \geq 10.65$ was applied to the original MaNGA ETG sample. Right: Histograms for integrated velocity dispersion, σ. The p-values of the corresponding K-S tests are shown in the title of the respective plots.

luminosity calculated from MGE model. The MGE surface brightness was converted to the AB magnitude system and corrected for cosmological dimming effects. However, the K-correction (Hogg et al., 2002) was not applied as most of the MaNGA galaxies are located at low redshift. The SPS fitting was performed using the pPXF package with the FSPS stellar population synthesis models on a grid of age and metallicity. A Salpeter IMF was adopted along with the MIST isochrones. Dust attenuation effect was also considered for the Milky Way and the target galaxy.

4.3.3 MaNGA sample selection

In DynPop I, the whole MaNGA sample was graded according to the modeling quality, which strongly depends on the data quality, as -1, 0, 1, 2, 3 (from worst to best). In this work, I considered only those galaxies with $Qual \geq 0$ because, below this quality flag, no kinematic measurements are reliable. Among these galaxies, the ETGs consist of elliptical (E) and lenticular (S0) galaxies, and the LTGs contain spiral (S) galaxies. To obtain this morphological classification, I used the MaNGA Deep Learning (DL) morphological catalog (Domínguez Sánchez et al., 2022) and the most restrictive selection criteria recommended in that paper (see their section 3.4.1). Applying this prescribed morphological selection formula with the above quality constraint, I found 2183 elliptical (E) and 807 lenticular (S0) galaxies among 10128 unique MaNGA galaxies. However,

for a few galaxies the stellar mass data were missing and I had to exclude them, resulting in a final MaNGA ETG sample of 2928 galaxies. However, 51% of the MaNGA ETGs are from $z > 0.05$. To have a sample that truly represents the low-redshift Universe, thus, I selected only those MaNGA ETGs located at $z \leq 0.05$. I further restricted the MaNGA galaxies to have a stellar mass of $\log M_*(M_\odot) \geq 10.65$. If I include galaxies with stellar mass below this level, then the resulting MaNGA sample with the applied redshift cut does not match the MUSE sample in terms of stellar mass or velocity dispersion. I performed two-sample Kolmogorov–Smirnov (K-S) tests on the MaNGA and MUSE samples to check whether they were drawn from the same underlying distribution in terms of integrated velocity dispersion and stellar mass. I found that the samples' velocity dispersion and stellar mass distributions are statistically consistent with p-values 0.22 and 0.27 respectively. Fig. 4.1 depicts the number density histograms of the two samples for $\log M_*$ and σ with respective p-values from K-S tests. After applying the above cuts, I have a MaNGA ETG sample of 746 galaxies and among them, 573 are 'E' type galaxies and 173 are 'S0' galaxies.

4.4 Correction of the observed λ_R for the MUSE sample

The apparent sizes of galaxies and spatial resolution decrease with distance, making atmospheric seeing effects significant. It is essential to account for these effects, especially for quantities derived from line-of-sight (LOS) kinematic maps such as λ_R. van de Sande et al. (2017) found that λ_R decreases with increasing PSF (FWHM) and that galaxies with higher λ_R are more strongly affected by seeing than galaxies with relatively lower values. This impact is strongest for small galaxies where R_e is comparable to the PSF. The λ_R quantities of MaNGA galaxies obtained from DynPop I were already PSF corrected. To compare with MaNGA, I also corrected the measured λ_R of MUSE galaxies for PSF effects by following an analytic recipe developed by Graham et al. (2018) with a python implementation[5]. This method requires the effective semi-major axis R_e^{maj} and Sérsic index of the galaxies in addition to the FWHM of the PSF and the observed λ_R. In Chapter 3, I described how the R_e^{maj} and λ_R of the MUSE sample were measured. We have used the PSF (FWHM) values provided as ancillary data in the FITS file of the respective MUSE data cubes, measured in the sky location of the target galaxy. If a PSF was not available for a specific sky location, I used the overall PSF of the FOV (also provided in the FITS file). I verified the reliability of these

[5]https://github.com/marktgraham/lambdaR_e_calc

PSF measurements by comparing the surface brightness data of a galaxy with the PSF-convolved surface brightness models of the same galaxy derived using JAMPY (Cappellari, 2008). For an accurate PSF value, the JAMPY model should match the observed surface brightness reasonably well. This check was conducted on a randomly chosen set of galaxies by visually comparing the surface brightness contours. In all cases, the provided PSFs produced models that fit the data well. Next, I describe how the Sérsic indexes were measured.

4.4.1 Fitting for Sérsic index

I measured the Sérsic index of each MUSE galaxy by fitting a PSF convolved 2D Sérsic surface brightness model to the HST image of the galaxy employing a Bayesian MCMC approach. The Sérsic profile contains seven free parameters and is defined as

$$I(x,y) = I_e \exp\left\{-b_n\left[\left(\frac{r(x,y)}{R_e}\right)^{(1/n)} - 1\right]\right\}$$

$$r(x,y)^2 = A^2 + \left(\frac{B}{1-\epsilon}\right)^2$$

$$A = (x - x_0)\cos(\theta) + (y - y_0)\sin(\theta)$$

$$B = -(x - x_0)\sin(\theta) + (y - y_0)\cos(\theta)$$

where $I(x, y)$ is the surface brightness at image position (x, y), I_e is the amplitude, R_e is the effective radius, n is the Sérsic index, ϵ is the ellipticity, (x_0, y_0) is the coordinate of the galaxy center and θ is the rotation angle of the major axis measured counter-clockwise from positive x-axis. The Sérsic model is then PSF convolved with a Gaussian kernel and fitted to the sky-subtracted HST image of the target galaxy. To keep the fitting restricted only to the region containing the observed galaxy, I used an elliptical mask. The elliptical mask is created for each target galaxy using the initial estimate of its structural parameters such as ellipticity, semi-major axis length, position angle of the major axis, coordinates of the center, etc. The initial estimate of these parameters except the semi-major axis length is determined using the 'FIND_GALAXY' function of the MgeFit package. The semi-major axis length is set to the maximum radius returned by the 'SECTORS_PHOTOMETRY' function of the MgeFit software with the constraint that the allowed minimum level of photon counts in the image has to be 2σ above the background level. The background level is initially estimated by fitting a Gaussian to the histogram of the photon count in the pixels of the image,

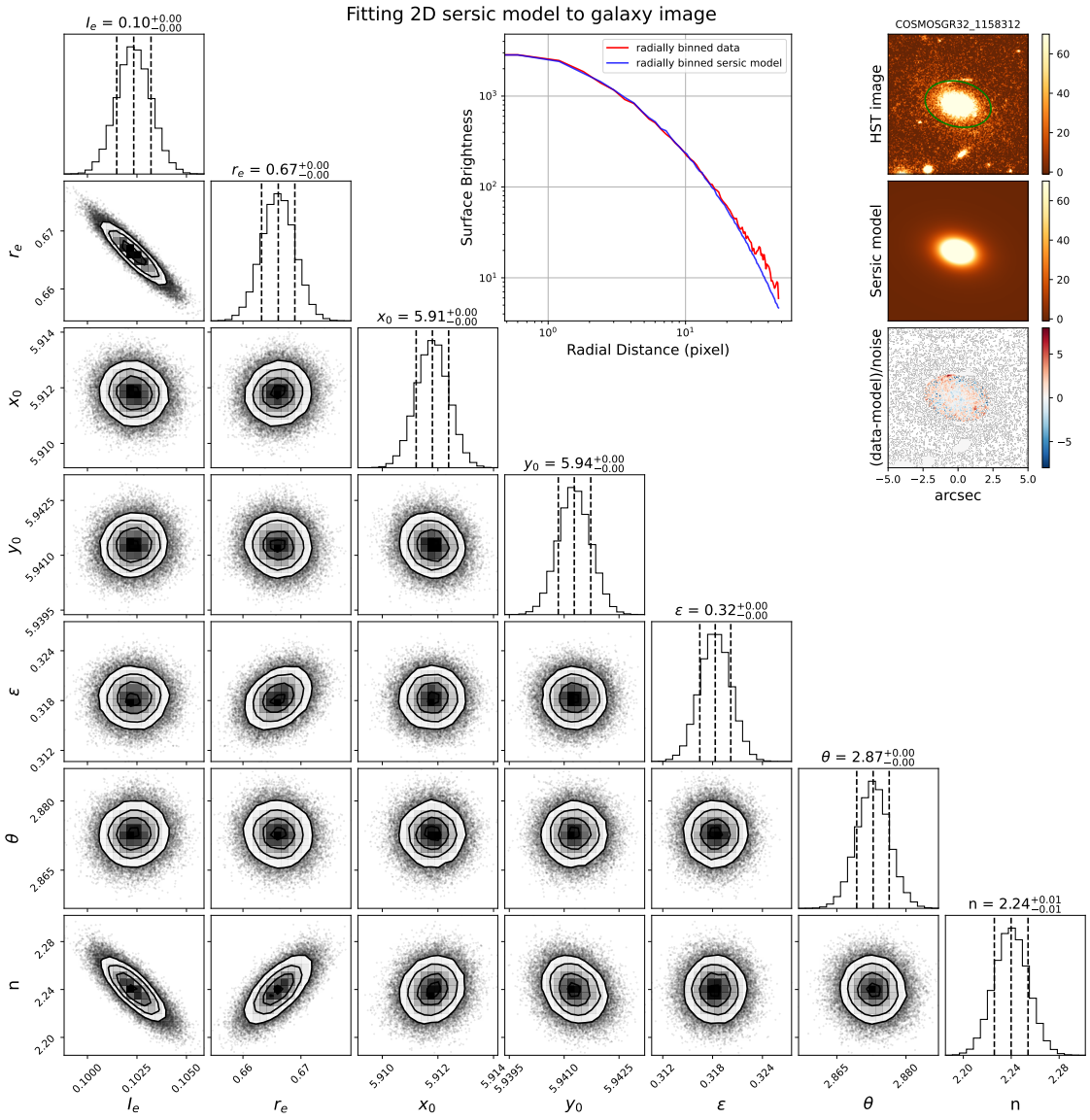


Figure 4.2: An example of a 2D Sérsic model fitting to the HST image of a galaxy. Left triangular panel: A corner plot showing the probability distributions and associated pairwise covariances of the seven free parameters of the fitted 2D Sérsic model using a Bayesian MCMC method. The fit was performed to the HST image of the galaxy COSMOSGR32_1158312 (z=0.725). The median of the chain for each parameter with the 1 σ uncertainty, measured using the 16th and 84th percentile values, was shown on top of each probability distribution plot. Middle top panel: Comparison of the 1D radial profile of the surface brightness created from the best-fit Sérsic model (blue) with the 1D radial profile from data of the galaxy (red). Right top panel: The top plot shows the HST image of the galaxy and the edge of the adopted elliptical mask (green solid line), the middle plot is the synthetic image created from the best-fitting 2D Sérsic model and the bottom plot shows the noise-weighted residuals.

excluding the target galaxy and other luminous objects. The mean of the fitted Gaussian is adopted as the background level and subtracted from the image.

The seven free parameters in the Sérsic profile model were fitted simultaneously in a Bayesian MCMC approach implemented by using the EMCEE python package (Foreman-Mackey et al., 2013). Before fitting, the effective radius and galaxy center coordinates were converted from pixel units to arcseconds, and the position angle θ was converted to radians. Flat priors were set for each parameter with the following ranges - $0 < x_0, y_0, r_e <$ image length (arsec), $0 < \epsilon < 1$, $0 < \theta < 2\pi$, $I_e > 0$ and $0 < n < 10$. Each MCMC chain was allowed to run for a maximum of 10,000 steps with 50 independent walkers. A run was allowed to terminate earlier if the chain exceeded 50 times the estimated combined autocorrelation time of all seven parameters. A certain number of initial steps were discarded from each chain as burn-in steps and then thinned by a factor of 10. The burn-in period was defined as either twice the autocorrelation time or 2000 steps, whichever was shorter. After that, the median of a chain was used as an estimate of the most likely parameter value, as it provides a straightforward way of measuring uncertainty. The 1σ uncertainty was determined as the 16th and 84th percentiles values of the chain. The best-fitting model was constructed using the most likely parameter set. Figure 4.2 presents a corner plot of the parameter distributions, the resulting best-fit model with the noise-weighted residuals, and a comparison of the 1D radial profile from the best-fit Sérsic model with the 1D radial profile from the data, using 400 radial bins. To check for potential biases introduced by the elliptical mask, the fitting was also performed using a square mask. The parameter medians did not vary significantly between the two cases. However, I adopted the Sérsic indexes from the elliptical masks as my final result. As a sanity check, I also compared ϵ and r_e from this fitting with the corresponding values from MGE fits described in Chapter 3. These comparisons also did not exhibit significant scatters which reinforces the reliability of the Sérsic fits. Further details of these tests are provided in a later section.

4.4.2 Applying correction for PSF effects

In general, the observed values of λ_R are lower than their intrinsic values due to PSF effects (Graham et al., 2018). Therefore, as the reported λ_{R_e} values of MaNGA galaxies already include a correction for PSF effects, a similar correction should be performed on the MUSE sample for fair comparison. As mentioned above, I used the code in Graham et al. (2018) for this task. However, a correction was not applied to a galaxy if the Sérsic index, n, was beyond the range of $0.5 < n < 6.5$

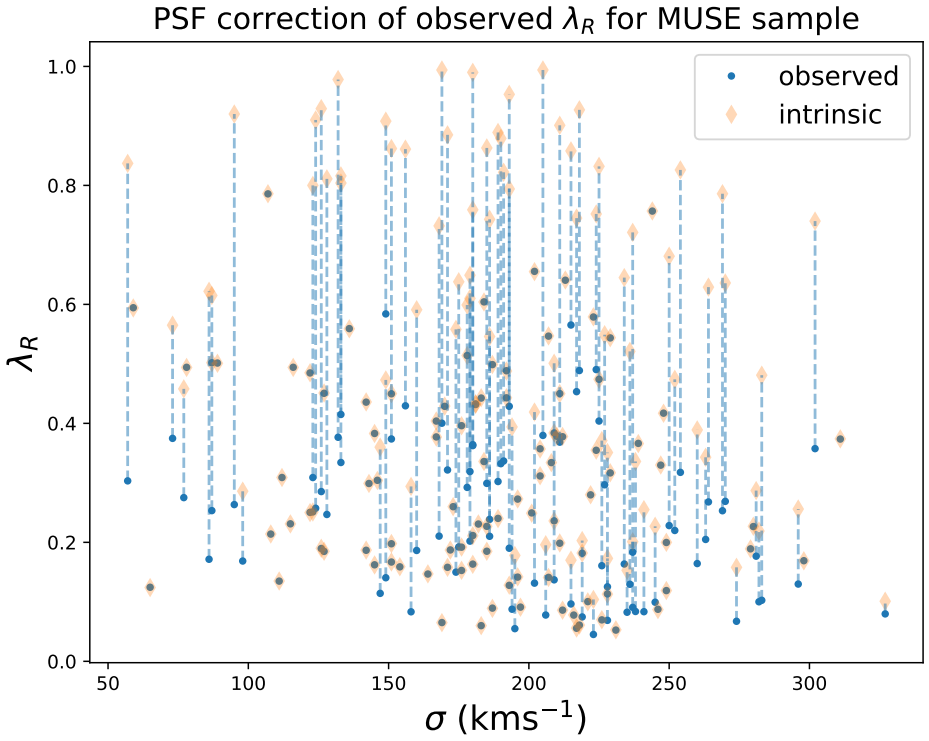


Figure 4.3: λ_R values of the MUSE sample before and after applying the PSF correction. The circles represent the observed λ_R and the diamonds represent the PSF corrected or intrinsic values. The dashed line connects a galaxy's observed and intrinsic λ_R. The galaxies for which a PSF correction was not applicable, kept to their original observed values. A correction was not applied to a galaxy if the Sérsic index, n, was beyond the range of $0.5 < n < 6.5$ or $R_e^{maj} < \sigma_{PSF}$ or corrected $\lambda_R = \frac{\mathrm{R|V|}}{\mathrm{R}\sqrt{\mathrm{V}^2+\sigma^2}} > 1$, as in these cases the correction is not reliable.

or $R_e^{maj} < \sigma_{PSF}$, as in these cases the correction is not reliable. Additionally, if the corrected λ_R goes above 1 ($\lambda_R = \frac{\mathrm{R|V|}}{\mathrm{R}\sqrt{\mathrm{V}^2+\sigma^2}}$), then the λ_R of that galaxy was kept to its observed value. Note that the same code and restrictions were also used in DynPop I to correct the observed λ_R of the MaNGA sample. In Fig 4.3, I show the λ_R values of the whole MUSE sample before and after applying the PSF correction. I found that for around 55% of the MUSE sample, the correction was not applicable due to the above-mentioned criteria and those galaxies were dropped from the sample before further analysis. Finally, I have 81 MUSE galaxies with corrected λ_R. In Fig. 4.4, I illustrate the overall impact of PSF correction on the MUSE sample by comparing the trend of running medians in the observed and intrinsic λ_R values. I only plot the observed (marked by circles) and intrinsic (marked by diamonds) values of the 81 galaxies that were PSF-corrected. The observed and corrected λ_Rs are sorted according to their velocity dispersion or stellar mass and

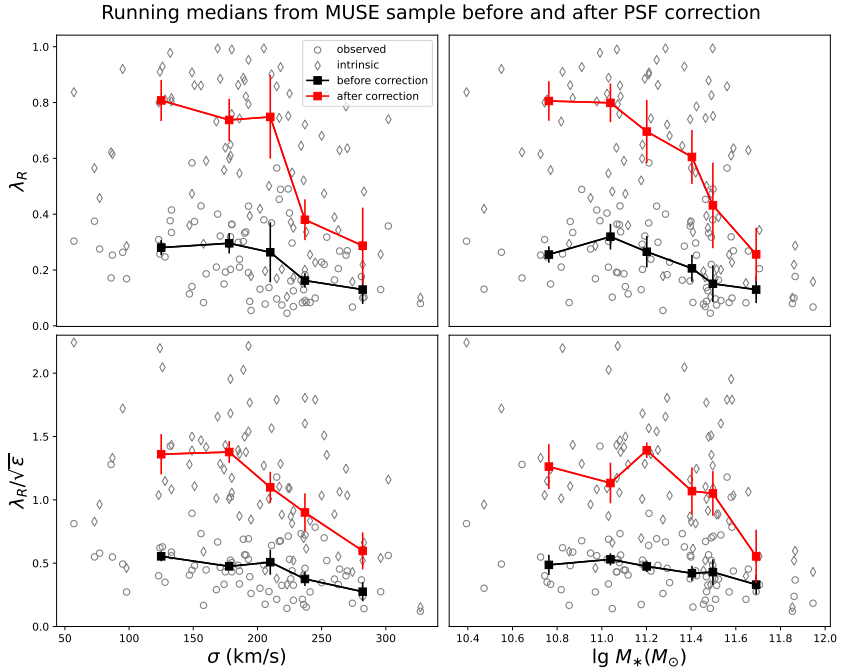


Figure 4.4: Comparison of the running medians in the observed and intrinsic λ_R and $\lambda_R/\sqrt{\epsilon}$ values of the MUSE sample. In each plot, we only show the observed (marked by circles) and intrinsic (marked by diamonds) values of the 81 galaxies that were PSF-corrected. The observed and corrected values are sorted according to their velocity dispersion or stellar mass and allocated in bins with equal numbers of galaxies. The square boxes represent the medians in the bins and the uncertainty of the medians in each bin was estimated using a bootstrap resampling method. Left panel: The top plot shows the running medians of the observed λ_R (black line) which were not PSF corrected and intrinsic or PSF corrected (red line), and the bottom plot shows the running medians for $\lambda_R/\sqrt{\epsilon}$. In these two plots, the galaxies were sorted according to their velocity dispersion σ. Right panel: Same as left panel, but this time the galaxies were sorted according to their stellar mass, M_*

allocated in bins with equal numbers of galaxies. The square boxes represent the medians in the bins and the uncertainty of the medians in each bin was estimated using a bootstrap resampling method.

To account for the projection effect in measured λ_R I used another quantity, $\lambda_R/\sqrt{\epsilon}$. I derived this quantity for both MUSE and MaNGA galaxies by using respective intrinsic or observed λ_R and ϵ. In Fig. 4.4, I also plotted the running medians in the observed and intrinsic $\lambda_R/\sqrt{\epsilon}$ values for the PSF corrected MUSE galaxies using the same procedure just mentioned above. In both cases, the intrinsic values are higher than the observed ones as expected. For the 81 galaxies in Fig. 4.4, on average, the PSF-corrected values have increased by 165% ± 76%. However, the effect of

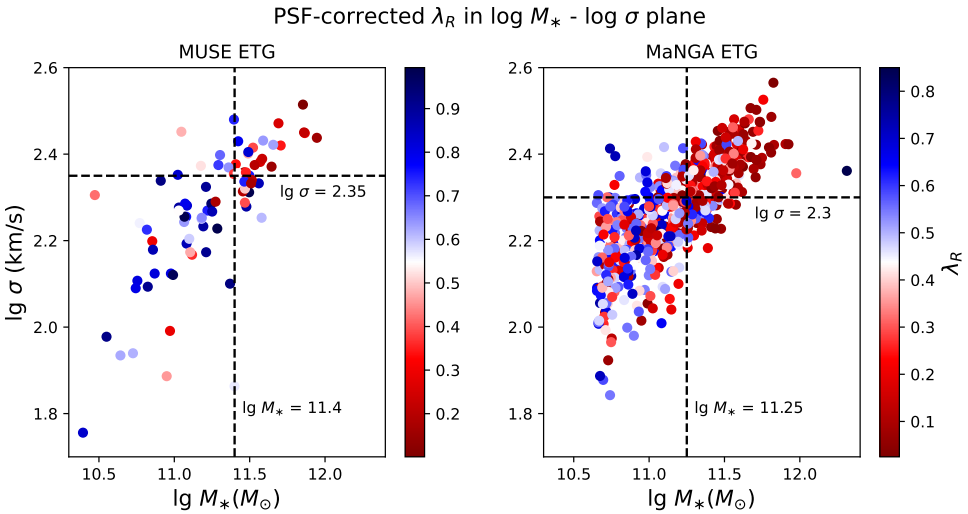


Figure 4.5: PSF-corrected λ_R in the M_* - σ_e plane. Left: This plot shows the intrinsic λ_R of 81 MUSE galaxies to which PSF correction was applied. Right: Intrinsic λ_{R_e} of the matched MaNGA sample containing 746 ETG galaxies. In both plots, the black dashed lines divide the corresponding sample into four parts where the top-right part is dominated by galaxies with high M_* and σ_e but lower λ_R. Contrarily, the bottom-left part is dominated by galaxies with low M_* and σ_e but higher λ_R. The first group represents mostly non-regular rotators and the second group represents regular rotators.

correction is higher for galaxies with lower mass and smaller velocity dispersion. These galaxies were mostly regular rotators with higher observed λ_R values and in general, a higher observed λ_R would change more from a PSF correction. The medians of the bins containing the most massive or least rotation-supported galaxies in both samples are within the measured uncertainties of each other. However, for the MUSE sample, the highest bins contain fewer galaxies than the other bins. As I only know the intrinsic λ_{R_e} values for the MaNGA sample, I can not quantify the effect of PSF correction on those galaxies. However, the $\lambda_{R_e}/\sqrt{\epsilon}$ of the MaNGA sample is on average 176% higher than the λ_{R_e}, and for the MUSE sample, the similar quantity is 165%. This ensures that if the PSF-corrected values were biased from systematic effects, they were biased in the same direction for both samples and confirms the robustness of this analysis.

4.5 Results and discussion

4.5.1 λ_R in M_* - σ plane

In Fig. 4.5, I color coded the PSF-corrected λ_R of both samples in M_* - σ plane. It is clear from the figure that for both MUSE and MaNGA samples, galaxies exhibit a trend of decreasing rotational support with increasing stellar mass and/or velocity dispersion. This pattern was also previously

observed in both local early-type galaxies (e.g., Cappellari et al., 2007; Emsellem et al., 2011) and quiescent galaxies at intermediate redshift (Bezanson et al., 2018). This observation confirms that both stellar mass and velocity dispersion are overall good predictors of angular momentum and thus rotational support in ETG galaxies located at z < 1 on a population level, and implies that ETG galaxies at low- and high-redshift have qualitatively similar dynamical structures. The black dashed lines in the plots visually divide the respective samples into four groups. Galaxies with high λ_R dominate the bottom-left group and the top-right group contains predominately low λ_R galaxies. However, the samples' horizontal and vertical separator lines are slightly different. For MUSE, the vertical and horizontal separators are log $M_* = 11.4$ and log $\sigma = 2.35$ while for the MaNGA sample, they are log $M_* = 11.25$ and log $\sigma = 2.3$ respectively. I found that for both samples while going from the bottom-left group to the top-right group, the respective means of λ_R of the groups have decreased by $\sim 47\%$. If I take this result at face value, that would suggest that the ETGs with higher λ_R have lost more rotational support compared to the galaxies with low λ_R. However, the small sample size of these high-redshift galaxies prohibits any strong interpretation of this result.

4.5.2 Measuring redshift evolution of rotational support

With the PSF corrected λ_R for the MUSE sample, I can evaluate the redshift evolution of rotational support by comparing them with the matched MaNGA sample. I have already discussed the measurement of the required galaxy properties for this analysis for both samples. I calculated the running medians and associated uncertainties of λ_{R_e} and $\lambda_{R_e}/\sqrt{\epsilon}$ of MaNGA galaxies using the same method as MUSE galaxies. The galaxies were sorted according to their velocity dispersion or stellar mass and allocated in bins with equal numbers of galaxies in each bin. The number of galaxies in each bin for the MaNGA sample was around eight times higher than the MUSE sample. I choose to use medians rather than means to have robust statistics by minimizing the effects of the outliers. In Fig 4.6, I show the λ_R of the MUSE sample using diamond shape markers and of the MaNGA sample using contour lines from a kernel density estimate (KDE) of the galaxy number density. The correlation between λ_R and velocity dispersion, where galaxies with lower velocity dispersions tend to have higher λ_R values and vice versa, is also reflected in the bimodal nature of the λ_R distribution for the MaNGA sample. The running medians from the MUSE and MaNGA samples are depicted by red and blue lines respectively with associated uncertainties. In all four cases, the medians from the MUSE sample are higher than the MaNGA ones which is a concrete

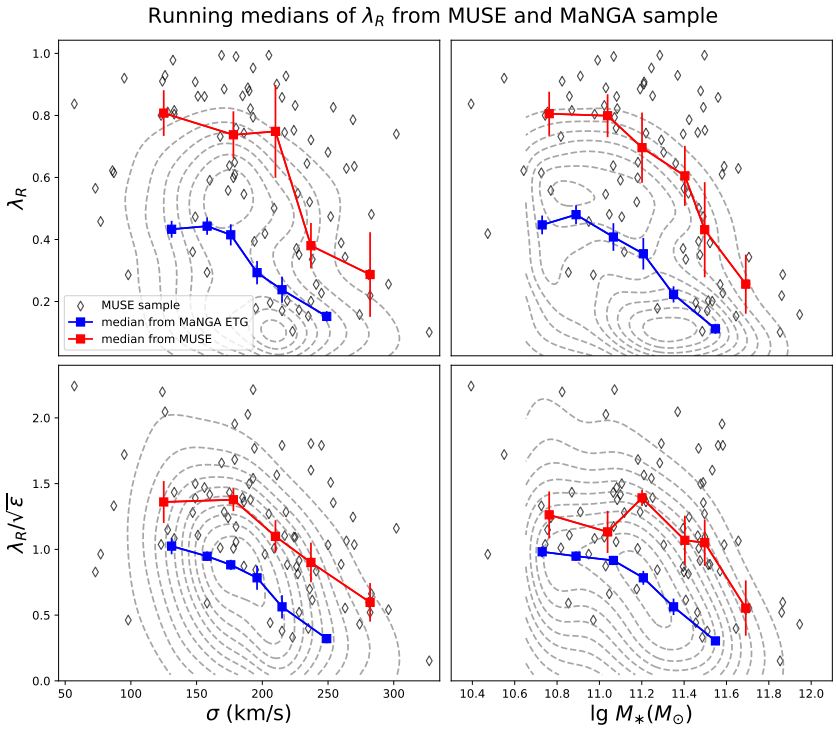


Figure 4.6: Evidence of increased rotational support in high-redshift galaxies. In each plot, the diamond markers point to the PSF-corrected values of the MUSE galaxies. The corresponding PSF-corrected values from MaNGA galaxies are shown as a kernel density estimate (KDE) of the galaxy number density using grey contour lines. The red squares denote the running medians from the PSF-corrected values of MUSE galaxies and the blue squares are for similar quantities from MaNGA galaxies. Each set of medians and uncertainties was measured in the bins of an equal number of galaxies sorted by their velocity dispersion or stellar mass. Left panel: The top plot shows the running medians of the intrinsic λ_R and the bottom plot shows the running medians for $\lambda_R/\sqrt{\epsilon}$. In these two plots, the galaxies were sorted according to their velocity dispersion σ. Right panel: Same as left panel, but this time the galaxies were sorted according to their stellar mass, M_*.

proof of increased rotational support at high redshift ETG galaxies. However, the difference in rotational support is more prominent for λ_R either sorted by velocity dispersion or stellar mass. The median values of λ_R in high-redshift galaxies are around 80% higher than their low-redshift counterparts when sorted either by velocity dispersions or stellar mass. However, for $\lambda_{R_e}/\sqrt{\epsilon}$, the medians at high-redshift are only higher by around 50% in both cases.

Bezanson et al. (2018) also observed evidence of increased rotational support at high redshift galaxies using the V/σ ratio and its projection corrected counterpart $(V/\sigma)/\sqrt{\epsilon/(1-\epsilon)}$. They found that at a fixed σ_e, on average, ETGs at $z \sim 0.8$ show around 90% more rotation within an aperture of radius 5 kpc than in the present-day Universe. In this analysis, instead of the V/σ ratio, I used another proxy for angular momentum, λ_R to quantify rotational vs random motion in a galaxy both in high and low redshift samples. I also used a projected aperture rather than a physical aperture.

The observed λ_{R_e} for MaNGA galaxies were measured in DynPop I using a circular aperture with a radius of 1 R_e. As λ_R values usually increase with a bigger aperture, it may be that the evidence of increased rotational support from MUSE galaxies is due to our adopted 2 R_e^{maj} elliptical aperture. To check this hypothesis, I measured λ_R using two other apertures and found that although aperture size affects observed λ_R values, my conclusion does not change based on aperture size. I have described these consistency checks in the next section. In section 4.6.3, I compare the observed λ_R values coming from different sizes of apertures and found that the aperture size doesn't affect the galaxies with $\lambda_R < 0.1$. I then show in section 4.6.4 that the medians in the PSF-corrected λ_R and $\lambda_{R_e}/\sqrt{\epsilon}$ values from all three apertures were relatively higher than the local measurements, indicating that the ETGs have lost their rotational support over cosmic time.

The galaxy properties used in reaching this conclusion were measured using the same techniques and model assumptions for both MUSE and MaNGA samples. Thus I have removed the possibility of systematic effects related to analysis choices. The estimated Sérsic index values for the MUSE galaxies reside within the range observed for ETGs at intermediate redshift (see Fig 4.8). Although a larger Sérsic index may play a role in magnifying the PSF-corrected value, the likelihood of this affecting the results was minimized through robust Sérsic fittings. (check section 4.6.1 and 4.6.2).

In addition to evaluating change in rotational support by comparing the MUSE and MaNGA samples, I also investigated whether there is any trend of evolution in rotational support with

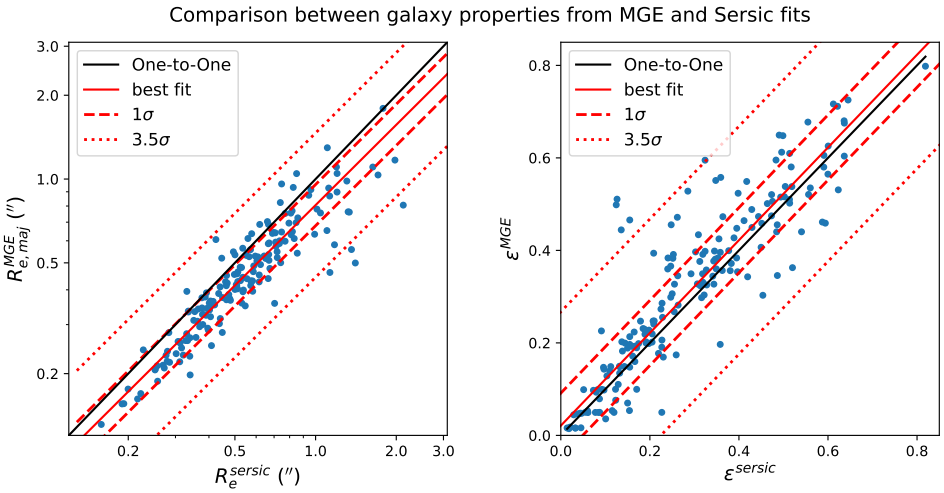


Figure 4.7: Comparison of estimates of effective radius and ellipticity from MGE and Sérsic fits. Left: Comparison between semi-major axis within elliptical half-light isophote, $R_{e,maj}^{MGE}$ and effective radius, R_e^{sersic}. The black line is the one-to-one line, the red line denotes the best-fit line and the red dashed and red dotted lines show 1σ and 3.5σ intrinsic scatter. The coefficients of the best-fit lines and intrinsic scatters were measured using the LtsFit python package (Cappellari et al., 2013b). Right: Comparison of ellipticities. The description of lines are same as the left plot. The one-to-one line in the left plot shows that the size estimates from the Sérsic fitting are usually higher than the ones from the MGE method. However, for ellipticity measurements, there is no such obvious bias.

redshift within the MUSE sample. Due to the small sample size, it is not meaningful to conduct this analysis in the above way by dividing the MUSE sample into two redshift groups and comparing running medians in the bins of velocity dispersion or mass of each group. Rather, I performed this analysis in two other ways. First, using a bootstrap resampling method and then fitting a line to the PSF-corrected λ_R values as a function of redshift. I divided the 81 MUSE galaxies into two groups: one group having $0.25 < z < 0.45$ and the other with $0.45 < z < 0.75$. Then I performed bootstrap resampling 1000 times. Each time, I collected a sample of 100 galaxies with replacements from each redshift group and computed their medians. The medians of these derived distributions are 0.62 ± 0.02 and 0.64 ± 0.01, corresponding to the lower and higher redshift groups respectively. The estimated uncertainties are the median standard deviations of these distributions. I also measured the trend of evolution in the λ_R as a function of redshift by conducting a linear fit using the LtsFit package (Cappellari et al., 2013b) and found that $\mathrm{d}\lambda_R/\mathrm{d}z = -0.08 \pm 0.23$. Though none of these tests show any trend of redshift evolution within the MUSE sample, a bigger sample is required to reach a definite conclusion.

4.6 Robustness of results

To emphasize the reliability and robustness of our results, I conducted a series of comparisons and additional tests. In the following subsections, I present the outcomes of these consistency checks.

4.6.1 Comparing structural properties from MGE and Sérsic fit

I measured the structural properties of the MUSE galaxies such as semi-major axis and ellipticity within an elliptical half-light isophote using MGE surface brightness models of HST images. I also estimated these two quantities while fitting a 2D Sérsic model to the HST image using a Bayesian approach. Although I adopted the estimates from the MGE models as our primary result, a comparison between the measurements from these two diverse methods based on the same underlying data shows the robustness of the methods. In Fig. 4.7, I plot similar quantities derived from MGE and Sérsic fitting along with the one-to-one (black) and the best-fit lines (red), and 1σ (red dashed)and 3.5σ (red dotted) intrinsic scatter lines. The coefficients of the best-fit lines and intrinsic scatters were measured using the LtsFit python package (Cappellari et al., 2013b). The one-to-one line in the left plot shows that the radii measurements from the Sérsic fitting tend to overestimate from the MGE method. However, for ellipticity measurements, there is no such obvious bias. This discrepancy may arise from the fact that the Sérsic fitting method assumes a uniform radial light profile, which can exaggerate the extent of the galaxy's surface brightness distribution. In contrast, the MGE fitting method, which models the surface brightness as a sum of multiple Gaussian components, can more accurately capture variations in the galaxy's light profile. The difference in these estimates may also arise from differences in the apertures used in those two methods. However, I tried to minimize this effect by creating the elliptical masks used in the Sérsic fittings from the parameters determining apertures for the MGE method. Regardless, the low intrinsic scatters between the measurements indicate the robustness of both MGE and Sérsic fitting methods.

4.6.2 Comparing Sérsic index from different apertures

I measured the Sérsic index of the MUSE galaxies by fitting a 2D Sérsic model with seven free parameters to the HST images of the galaxies using a Bayesian approach (see section 4.4.1). To check the dependence of the estimated Sérsic index on the choice of apertures, I performed the fitting two times, once with an elliptical aperture and then with a square aperture. In Fig. 4.8,

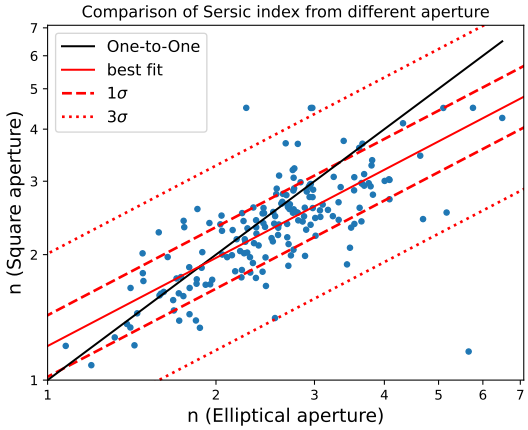


Figure 4.8: Comparison of Sérsic index estimates from 2D Sérsic fitting with elliptical and square aperture. The black line denotes the one-to-one line, the red line is the best-fit line and the red dashed and red dotted lines show 1σ and 3.5σ intrinsic scatter. The coefficients of the best-fit lines and intrinsic scatters were measured using the LtsFit python package (Cappellari et al., 2013b). The one-to-one line shows that, in general, the Sérsic index measured using an elliptical aperture is higher than the square aperture. A square aperture by including more background light and thus flattening the galaxy's light profile, may lead to a lower Sérsic index value.

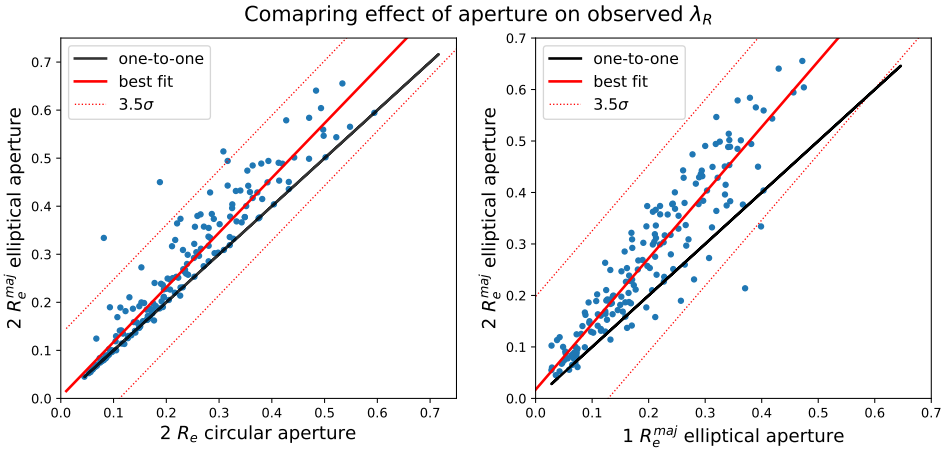


Figure 4.9: Comapring measured λ_R of MUSE galaxies from different aperture sizes. Left: Comparison between an elliptical aperture with a semi-major axis of 2 R_e^{maj} and a circular aperture of radius 2 R_e. The red is the best-fit line and the red dotted line shows the 3.5σ intrinsic scatter. The black line is the one-to-one line. Right: Comparison between elliptical apertures with semi-major axes of 2 R_e^{maj} and 1 R_e^{maj}. The description of the lines is the same as the left plot. The one-to-one line is closer to the best-fit line when the λ_R value is small in both cases. The intrinsic scatter and deviation of the one-to-one line from the best-fit line are more significant in the right plot as in this case, the aperture sizes are significantly different. However, aperture size does not affect the galaxies with $\lambda_R < 0.1$, which are predominantly rounder and kinematically classified as non-regular rotators.

I plot the Sérsic index measurements from the fitting with two different apertures along with the one-to-one line (black), the best-fit line (black) and 1σ (red dashed) and 3.5σ (red dotted) intrinsic scatter lines. The coefficients of the best-fit lines and intrinsic scatters were measured using the LtsFit python package (Cappellari et al., 2013b). From the one-to-one line it is evident that, in most cases, the Sérsic index measured using an elliptical aperture is higher than the square aperture. An elliptical aperture, which is more closely aligned with the shape of the galaxy, tends to exclude more of the background light whereas the square aperture is more likely to include additional background light from the sky or nearby sources. As the Sérsic index describes how the intensity of a galaxy's light decreases from its center, the extra background light may flatten this decrease, resulting in a lower estimated value. This comparison suggests that the choice of an elliptical mask is more reasonable, and in this work, I used the results from the elliptical apertures as our official estimates.

4.6.3 Effects of aperture size on λ_R

The aperture size affects the measured λ_R. In Fig. 4.9, we show the effect of different aperture sizes on the measured λ_R of the MUSE galaxies. I adopted λ_R values measured using an elliptical aperture with a semi-major axis of 2 R_e^{maj} as our default result. I compared these λ_R values with the ones from a circular aperture of radius 2 R_e and an elliptical aperture with a semi-major axis of 1 R_e^{maj}. As expected, the λ_R measured from these two apertures are lower than the adopted results. However, the λ_R from the circular aperture shows less deviation than the 1 R_e^{maj} aperture. The divergence between the one-to-one lines and the best-fit lines confirms this. Again, this divergence and the intrinsic scatter is higher for λ_R from 1 R_e^{maj} aperture. The one-to-one line is closer to the best-fit line when the λ_R value is small. The galaxies with lower λ_R values are predominantly rounder and classified as non-regular rotators. As a result, the difference between the radius and semi-major axis is less significant, and the circular aperture of R_e radius and the elliptical aperture with 2 R_e^{maj} contains almost the same information regarding angular momentum. However, for galaxies with higher λ_R, which are predominantly flat and regular rotators, the differences between circular and elliptical apertures may not be negligible. The elliptical aperture contains more information along the major axis and thus produces a higher λ_R than a circular aperture of almost the same area. Similarly, an elliptical aperture with a semi-major axis of 1 R_e^{maj} certainly provides less information about angular momentum and yields a lower λ_R. Again, this effect is more significant

for flatter regular rotators than rounder non-regular rotating galaxies.

4.6.4 Comparing λ_R from different apertures of MUSE galaxies to MaNGA

I described the effect of aperture size on observed λ_R of MUSE galaxies in section 4.6.3 and argued that the effect is more significant for flatter galaxies than the rounder ones. Usually, the flatter galaxies are regular rotators and have more rotational support and higher λ_R (see Fig. 3.4). I applied the PSF correction, as described in section 4.4, to the measured λ_R values from the circular aperture of radius 2 R_e and elliptical aperture with a semi-major axis of 1 R_e^{maj}. During this process, each set of observed λ_R was varied, and other required quantities such as PSF, Sérsic index, and semi-major axis length remained the same. That means the effect of correction is only dependent on observed λ_R. A PSF correction was applied to a galaxy if the Sérsic index, n, is within the range of $0.5 < n < 6.5$ or $R_e^{maj} < \sigma_{PSF}$ or the corrected $\lambda_R = \frac{\mathrm{R|V|}}{\mathrm{R}\sqrt{\mathrm{V}^2+\sigma^2}} \leq 1$, as in these cases the correction is reliable. For 2 R_e^{maj} case, the PSF correction was applied to 120 galaxies, and for 2 R_e aperture, the correction was applied to 104 galaxies. Compared to this, PSF correction was applied to 81 galaxies for 2 R_e^{maj} aperture. This also confirms that the higher observed λ_R was affected more by the correction. After that, I measured the running medians and uncertainties from each set of PSF-corrected λ_R and $\lambda_R/\sqrt{\epsilon}$ values following the same method as before (see section 4.5.2). In Fig. 4.10, I plot each set of running medians of the MUSE sample derived from different apertures with the MaNGA galaxies sorted by stellar mass. This plot illustrates that although the choice of different apertures affects λ_R and $\lambda_R/\sqrt{\epsilon}$, it does not undermine our conclusion that the ETG galaxies at high-redshift have more rotational support than their local counterparts. I observed the same scenario if the galaxies were sorted by their velocity dispersion. Except in a few cases, in each bin, the running medians were within the statistical uncertainties of one another. One should note that in a bin of low-mass galaxies (M_* <11.3), the median from a smaller aperture becomes lower. However, the difference becomes almost negligible in a bin of high-mass galaxies (M_* > 11.3). This is because the high-mass galaxies mostly have low observed λ_R values and are thus less affected by the choice of aperture. These are the group of galaxies located in the top-right part in Fig. 4.5 which have high M_* and σ. Contrarily, the group of galaxies that are affected more by aperture choice have higher λ_R and lower M_* and σ and located in the bottom-left part in Fig. 4.5. The running medians from $\lambda_R/\sqrt{\epsilon}$ values show similar patterns as the λ_R ones, however, the overall

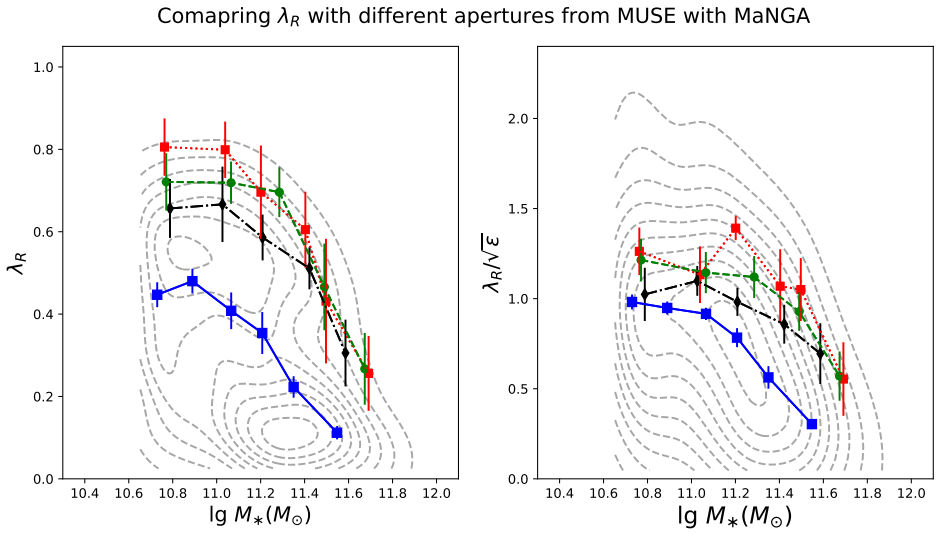


Figure 4.10: Comparing PSF-corrected λ_R and $\lambda_R/\sqrt{\epsilon}$ of the MUSE sample from different apertures with MaNGA galaxies. Left: Running medians from three sets of PSF-corrected λ_R values of MUSE galaxies from three different sizes of apertures, an elliptical aperture with a semi-major axis of 2 R_e^{maj} (red squares with dotted line), a circular aperture of radius 2 R_e (green circles with dashed line), and an elliptical aperture with a semi-major axis of 1 R_e^{maj} (black diamonds with dashed-dot line), are plotted along with the ones from the MaNGA sample (blue squares with solid line). Each set of markers represents the medians in the bins of galaxies sorted by their stellar mass and the lines display the decreasing trends in medians with increased mass. A kernel density estimate of the number density of MaNGA galaxies is shown using grey contour lines. Except in a few cases, in each bin, the running medians were within statistical uncertainties of one another. The effect of aperture size is prominent in bins of low-mass galaxies ($M_* < 11.3$), however, almost disappears in the bins of high-mass galaxies ($M_* > 11.3$). Right: Running medians from three sets of PSF-corrected $\lambda_R/\sqrt{\epsilon}$ values of MUSE galaxies along with the MaNGA sample. The description of different markers and lines remains the same as the left plot. We see a similar pattern as the left, however, the overall difference between medians has decreased.

difference among each set of medians of MUSE and MaNGA has decreased. This is expected, as dividing λ_R with ellipticity minimizes the intrinsic scatter in λ_R.

4.7 Conclusion

In this work, I investigated the degree of rotational support in early-type galaxies (ETGs) at different cosmic epochs, comparing high-redshift ETGs with their local counterparts. My analysis revealed clear evidence of a decrease in rotational support over cosmic time. For our local reference, we used a sample of ETGs from the MaNGA survey, focusing on galaxies with redshifts below 0.05 and stellar masses of $\log M_*(M_\odot) \geq 10.65$. The required galaxy properties for this analysis such as a proxy for angular momentum, λ_R are already available in the literature for this sample. I compared

this local sample with higher-redshift ETGs ($0.25 < z < 0.75$) collected using MUSE-DEEP datacubes. The selection, kinematic extraction, and measurements for these high-redshift galaxies were detailed in Chapter 3. In this chapter, we corrected the observed λ_R values of MUSE galaxies for PSF effects following the same method applied to MaNGA ETGs. The required Sérsic indices for MUSE galaxies were estimated using HST photometry and a Bayesian approach. Although the apertures used to measure λ_R differed between MUSE and MaNGA, 1 R_e circular aperture for MaNGA and 2 R_e^{maj} elliptical for MUSE, I verified that this did not alter my conclusions. I measured λ_R for the MUSE sample using various aperture sizes and found that while aperture size influences λ_R values, it does not affect the overall trend.

This study also showed that galaxies in both MUSE and MaNGA samples exhibit less rotational support with increasing stellar mass and/or velocity dispersion. This pattern aligns with previous observations of local ETGs and intermediate redshift quiescent galaxies, confirming that stellar mass and velocity dispersion are reliable predictors of angular momentum and rotational support in ETGs at $z < 1$. From this observation, I can conclude that, at fixed mass or velocity dispersion, ETGs have similar dynamical structures ((e.g. less or more rotational support) across different redshifts.

The galaxy properties for both MUSE and MaNGA samples were measured using the same techniques and assumptions, minimizing the risk of systematic biases. I also conducted several comparisons and additional tests to validate our results. These tests checked the consistency of the galaxy properties measured by different methods and assessed the impact of factors like aperture size. I note that this analysis employed high-quality IFU data to derive λ_R and used a larger sample of both local and high-redshift galaxies compared to previous studies. In conclusion, my comprehensive analysis confirms a significant decrease in rotational support in ETGs over cosmic time. However, the physical processes driving this change in ordered motion remain a topic of ongoing debate. This study enhances our understanding of the dynamical evolution of ETGs from high to low redshift, highlighting the importance of detailed kinematic studies in unraveling the complexities of galaxy evolution.

Chapter 5

Evolution in the total mass density slopes of early-type galaxies at intermediate redshift

5.1 Introduction

Galaxies form within dark matter (DM) halos as baryonic matter condenses at their centers (e.g. White & Frenk, 1991). Consequently, the combined distribution of baryonic matter and DM determines the mass distribution within a galaxy and can be described by a radial density profile, $\rho(r) \propto r^{-\gamma}$, where γ represents the total density slope. The spatial distribution of baryonic and DM components is crucial for shaping galaxies and evolves due to various processes like mergers, gas accretion, and environmental interactions. Therefore, understanding the total density slope is essential for gaining insights into the mechanisms of galaxy formation and evolution.

In the local Universe, several studies have been conducted to measure the total density slopes of galaxies and have converged to a concentration of values around or slightly steeper than $\gamma = 2$ (e.g. Cappellari et al., 2015; Poci et al., 2017; Bellstedt et al., 2018; Li et al., 2019). These studies predominantly relied on dynamical modeling techniques, either the comprehensive Schwarzschild orbit superposition technique (Schwarzschild, 1979) or the simpler Jeans approach (Jeans, 1922). Both of these techniques require high-quality 2D kinematic information for the galaxies. At low redshifts, cosmological simulations have also produced similar results, with the total density slope being close to isothermal ($\gamma = 2$) at $z = 0$ (Wang et al., 2019).

At intermediate redshifts, there is still no consensus on the evolution of mass distribution in massive early-type galaxies (ETGs). Some cosmological simulations indicate that the total density slope was steeper in the past and has become shallower over time. For instance, the IllustrisTNG,

a set of magnetohydrodynamical simulations (Pillepich et al., 2018), suggests little or almost no evolution in γ below $z \sim 1$ (Wang et al., 2019). In contrast, the Magneticum simulations (Dolag, 2015) show an evolution in the density slope from $\gamma \sim 2.3$ to $\gamma \sim 2.0$ between $z = 1$ and $z = 0$ (Remus et al., 2017). From the observational side, the constraints are primarily based on either gravitational lensing or dynamical modeling. However, measurements from gravitational lensing up to $z \sim 0.8$ contradict the results from the simulations. These lensing-based studies, which may be biased toward the most massive ETGs in the Universe, suggest that density slopes are shallower at earlier times compared to the local Universe. For example, the Lenses Structures and Dynamics (LSD) survey (Koopmans & Treu, 2004) found $\gamma \sim 1.75$ at a median $z \sim 0.8$ (Treu & Koopmans, 2004; Koopmans et al., 2006). Other studies using the Sloan Lens ACS Survey (SLACS), Strong Lenses in the Legacy Survey (SL2S), and BOSS Emission-Line Lens Survey (BELLS) also found that total density slopes were systematically steeper at lower redshifts with mild to significant trends with redshift (Auger et al., 2010; Ruff et al., 2011; Bolton et al., 2012; Sonnenfeld et al., 2013; Li et al., 2018). This trend still exists even after considering changes in total density slope with other galaxy parameters such as the effective radius, R_e or the surface mass density Σ (Bolton et al., 2012; Sonnenfeld et al., 2013; Li et al., 2018, e.g.). From the dynamical modeling side, Derkenne et al. (2021) measured the total density slope from 90 ETGs using axis-symmetric Jeans anisotropic modeling. These Frontier Field galaxies span from around $0.3 < z < 0.55$ with only around 15% of the total sample above $z > 0.4$, thus constraining the utility of this sample in estimating the evolution of $\overline{\gamma}$ at intermediate redshifts. Using a similar Jeans anisotropic modeling approach, the MAGPI survey, which aims to investigate the role of the galaxy host environment in determining its mass distribution and evolution, measured the total density slope of a sample of 30 galaxies with a median redshift of 0.3. However, this sample also covers too narrow a range to evaluate correlation with redshift.

To resolve this discord between observation and simulation, I aim to measure the total density slope of a sample of galaxies up to a redshift of 0.75 using Jeans anisotropic modeling (JAM). This dynamical modeling method has been extensively used in several studies both in local and intermediate redshift (e.g. Derkenne et al., 2021, 2023; Zhu et al., 2023). Recently, Zhu et al. (2023) used this technique to measure the total density slope of around 10000 nearby galaxies based on resolved stellar kinematics from the MaNGA survey. To determine systematic uncertainties in the

measurements, they employed eight dynamical models with varied assumptions. These models are a combination of four different mass profiles with two different velocity ellipsoid orientations (spherical or cylindrical). However, they found no statistically significant scatter between the measured quantities from various models highlighting the robustness of the technique. In this work, I will extend this dynamical modeling technique up to $z = 0.75$ for the first time and provide a complementary perspective to the gravitational lensing-based findings.

To understand the redshift evolution, one requires an evenly distributed and statistically definitive sample with similar data quality gathered over a long redshift baseline and analyzed using a homogeneous process. Though one can compare studies done at different redshift ranges, the difference in data quality and analysis methods in these studies may undermine the conclusion. In this work, I provided a homogeneous analysis from 108 early-type galaxies collected from MUSE-DEEP datacubes. I measured the total density slope of these galaxies by modeling their resolved kinematics in an axis-symmetric JAM modeling framework. To account for possible systematics, I used several models varied in the assumptions of mass distribution and alignment of the velocity ellipsoids. I also compared the measurements from this work with other samples in the literature to improve the reliability of the results.

This chapter is organized as follows. In the next section, I briefly describe the sample selection and data extraction process (see Chapter 3 for more details). In section 5.3, I provide the theoretical background of the Jeans anisotropic modeling and the mathematical basis of the multi-Gaussian expansion (MGE) modeling of the surface brightness. I also describe the four mass models adopted in this work along with assumptions for kinematic anisotropy. Then I explain the parameter design and fitting procedure, and how the fitted models were employed to measure different dynamical quantities such as total density slope. I present the results, systematic tests, and associated discussions from the MUSE sample in section 5.4. Finally, in section 5.5, I summarize the key results and conclude. Throughout this study, I assume a flat ΛCDM cosmology with $H_0 = 70.0$ km s^{-1} $Mpc^{-1}$and $\Omega_m = 0.3$ when necessary.

5.2 Data

In this work, I used the galaxies from the MUSE sample and associated data described in chapter 3. Here I provide a brief description of the sample selection and data extraction process.

5.2.1 Sample selection

MUSE is an integral-field spectrograph located at the Very Large Telescope (VLT) of the European Southern Observatory (ESO). This spectrograph provides a spatial resolution of 0.2″over a 1′× 1′ field-of-view (FOV) in the wide-field mode (Bacon et al., 2010). The covered wavelength range is 4800–9300 Å with 1.25 Å spectral pixel.

To assemble a comprehensive sample of massive early-type galaxies (ETGs) at intermediate redshifts ($0.25 < z < 0.8$), I manually reviewed all publicly accessible MUSE-DEEP IFU datacubes with exposure times above 7999 seconds in the ESO Science Archive. I selected datacubes containing elliptical galaxies above $z > 0.25$, narrowing down to 80 prospective datacubes. Further inspection reduced this to 40 datacubes of sufficient quality, from which 264 individual galaxies were extracted.

Selection criteria for these galaxies included isolation from other galaxies to minimize contamination and sufficient size (> 2″along the major axis) to extract resolved stellar kinematics up to a few effective radii. I have considered a galaxy as sufficiently isolated if there is no other galaxy within the 2-3 arcsecond radii of the target galaxy, that may contaminate the measurements from the target galaxy. From the initial 264 galaxies, 84 were excluded due to a lack of Hubble Space Telescope (HST) images or insufficient Voronoi bins at the chosen SNR, resulting in a final sample of 180 galaxies. These criteria were necessary because using a mix of HST and ground-based images could introduce systematic issues in surface brightness modeling. HST images ensure consistency across the sample, whereas different ground-based images from various telescopes require different treatments to standardize them. Additionally, without sufficient data points (one Voronoi bin represents one data point for dynamical modeling), the resulting dynamical models would lack reliability.

5.2.2 Stellar kinematics and photometry

The MUSE-DEEP collection provides reduced 3D data and variance cubes, processed using the MUSE data reduction pipeline (Weilbacher et al., 2020). This pipeline removes instrument signatures, performs sky-correction, and combines data into a single cube. Individual cubes for each galaxy were extracted using MPDAF (Bacon et al., 2016) and then for each galaxy, a central spectrum was created by co-adding spectra within 1 effective radius. Integrated stellar kinematics were

extracted using a penalized pixel fitting method implemented through pPXF package (Cappellari & Emsellem, 2004; Cappellari, 2017, 2023) by fitting the central spectra with all templates within the Indo-US stellar library. pPXF fits a model to the observed galaxy spectrum in pixel space where the models are created using a weighted linear combination of the broadened stellar templates to which a sum of orthogonal polynomials is added. The FWHM of the Gaussian kernel used to broaden the templates was set to $\mathrm{FWHM}^2_{\mathrm{diff}} = \mathrm{FWHM}^2_{\mathrm{MUSE}} - \mathrm{FWHM}^2_{\mathrm{temp}}$, the quadratic difference between the redshift-corrected FWHM resolution of MUSE for the respective galaxy and the template. A single rest-frame wavelength range from 3780-4600 Å was adopted for all kinematic analyses to ensure that galaxies from different redshifts contain the same absorption features. After fitting to a central spectrum, a global template set was created for each galaxy by only using the templates selected in the initial fit. This global template set was later used to measure the resolved kinematics of the respective galaxy.

Next, a 2D SNR map was created for each galaxy by measuring the median SNR of the spectrum in each spaxel within the rest-frame wavelength range 3990-4090 Å. After that, regions with a median SNR of 2.5 or higher were selected and Voronoi binned to a target SNR of 12 per bin. However, galaxies with fewer than 10 bins were excluded to ensure reliable kinematic measurements. The spaxel data were coadded according to the Voronoi bins, and using the above setting the stellar velocity and velocity dispersion were measured for each bin, resulting in velocity and dispersion maps. For this, the global template set was used to enhance the robustness of kinematic measurements in lower-SNR bins.

HST images covering the same sky location as the MUSE-DEEP cubes were used to measure the photometry of the galaxies. We fitted a Gaussian to the histogram of the photon count in each pixel of a galaxy image to measure the background level. The mean of the fitted Gaussian was adopted as the background level and the standard deviation was used as a criterion to differentiate the galaxy contribution from that of the background (1σ above the mean or background). The sky-subtracted images were then used to model the surface brightness of the galaxies using a series of 2D Gaussian profiles implemented by the python package Multi-Gaussian Expansion fitting of galactic images (MgeFit[1]) (Cappellari, 2002).

[1]We used the MgeFit Python package v5.0 from https://pypi.org/project/mgefit/

5.3 Analysis method

In this section, I provide the mathematical basis of the Jeans anisotropic modeling that I have used to predict the resolved stellar kinematics of the galaxies. These predictions utilize the multi-Gaussian expansion models of the surface brightness of the galaxies embedded into an intrinsic gravitational potential.

5.3.1 Jeans anisotropic modelling

The steady-state collisionless Boltzmann equation (Binney & Tremaine, 1987, Eq. 4-13 b) encodes the orbital motion of the stars via the distribution function $f(\boldsymbol{x}, \boldsymbol{v})$ of position $\boldsymbol{x}$ and velocity $\boldsymbol{v}$, in the galactic potential Φ is described as

$$\sum_{i=1}^{3} \left(v_i \frac{\partial f}{\partial x_i} - \frac{\partial \Phi}{\partial x_i} \frac{\partial f}{\partial v_i} \right) = 0$$

However, without further assumptions and simplifications, we can not practically use this equation. Assuming an axisymmetric stellar system (i.e., $\partial\Phi/\partial\phi = \partial f/\partial\phi = 0$) with ϕ, we obtain the following Jeans equations in cylindrical coordinates, (R, z, ϕ) (Binney & Tremaine, 1987, eq. 4-29 a,c) as

$$\begin{aligned} \frac{\zeta(\overline{v_R^2} - \overline{v_\phi^2})}{R} + \frac{\partial\left(\zeta \overline{v_R^2}\right)}{\partial R} + \frac{\partial\left(\zeta\, \overline{v_R v_z}\right)}{\partial z} &= -\zeta \frac{\partial \Phi}{\partial R}, \\ \frac{\zeta\, \overline{v_R v_z}}{R} + \frac{\partial\left(\zeta\, \overline{v_z^2}\right)}{\partial z} + \frac{\partial\left(\zeta\, \overline{v_R v_z}\right)}{\partial R} &= -\zeta \frac{\partial \Phi}{\partial z}, \end{aligned} \tag{5.1}$$

where ζ is the number density of the tracer population from which one measures the kinematics such that

$$\zeta\, \overline{v_k v_j} \equiv \int v_k v_j f \, \mathrm{d}^3 v$$

This equation set is fairly general, relying only on the assumptions of axial symmetry and steady-state conditions in the stellar system. However, as there are more unknowns than equations, one has to make further assumptions to yield a unique solution. Now, if one assumes that the velocity ellipsoid is aligned with the cylindrical coordinates then due to axial symmetry $\overline{v_R v_z} = 0$. Additionally, if we further assume that the velocity anisotropy, β_z in the meridional plane is constant, which is quantified as

$$\beta_z \equiv 1 - \frac{\overline{v_z^2}}{\overline{v_R^2}} = 1 - \frac{\sigma_z^2}{\sigma_R^2} = 1 - \frac{1}{b}$$

then the above equation set reduces to (Cappellari, 2008, eq. 8 and 9)

$$\begin{aligned} \frac{\zeta\ (b\overline{v_z^2} - \overline{v_\phi^2})}{R} + \frac{\partial\left(b\zeta\ \overline{v_z^2}\right)}{\partial R} &= -\zeta\ \frac{\partial\Phi}{\partial R} \\ \frac{\partial\left(\zeta\ \overline{v_z^2}\right)}{\partial z} &= -\zeta\ \frac{\partial\Phi}{\partial z}, \end{aligned} \tag{5.2}$$

This equation set can be solved to yield unique solutions for $\overline{v_z^2}$ and $\overline{v_\phi^2}$ under the boundary condition $\zeta\ \overline{v_z^2} = 0$ as $z \to \infty$.

Similarly, if one assumes that the velocity ellipsoid is aligned with the spherical coordinates (r, θ, ϕ) and the velocity anisotropy is defined as

$$\beta_r \equiv 1 - \frac{\overline{v_\theta^2}}{\overline{v_r^2}} = 1 - \frac{\sigma_\theta^2}{\sigma_\gamma^2}$$

then Jeans equations transform to the following equations (Cappellari, 2020, eq. 7)

$$\begin{aligned} \frac{\partial\left(\zeta\ \overline{v_r^2}\right)}{\partial r} + \frac{(1+\beta_r)\ \zeta(\overline{v_r^2} - \overline{v_\phi^2})}{r} &= -\zeta\ \frac{\partial\Phi}{\partial r} \\ (1-\beta_r)\ \frac{\partial\left(\zeta\ \overline{v_r^2}\right)}{\partial\theta} + \frac{(1-\beta_r)\ \zeta\ (\overline{v_r^2} - \overline{v_\phi^2})}{\tan\theta} &= -\zeta\ \frac{\partial\Phi}{\partial\theta} \end{aligned} \tag{5.3}$$

As before these equations could be solved for unique solutions of $\overline{v_r^2}$ and $\overline{v_\phi^2}$ under the boundary condition $\zeta\overline{v_r^2} = 0$ as $\mathrm{r} \to \infty$.

That means for an adopted gravitational potential Φ, with tracer density distribution ζ and velocity anisotropy (β_z or β_r for cylindrical or spherical velocity ellipsoid orientation), the intrinsic second velocity moment, either (v_z^2, v_ϕ^2) or (v_r^2, v_ϕ^2)) can be obtained by solving equation set 5.2 or 5.3 respectively. In practice, we assume a mass density profile and an anisotropy model under a particular velocity ellipsoid orientation, and the tracer density distribution is measured from the surface brightness of the galaxy. The projected LOS second velocity moment can then be estimated as

$$S\left\langle v_{\mathrm{los}}^2\right\rangle(x,y) = \int_{-\infty}^{\infty} \mathrm{d}z\zeta\left\langle v_z^2\right\rangle.$$

where $S(x, y)$ is the surface density of the dynamical tracer. The luminosity-weighted observed LOS velocity dispersion is given by

$$\left[\left\langle v_{\mathrm{los}}^2\right\rangle\right]_{\mathrm{obs}} = \frac{\int_{\mathrm{ap}} \mathrm{d}x\ \mathrm{d}yI\left\langle v_{\mathrm{los}}^2\right\rangle \otimes \mathrm{PSF}}{\int_{\mathrm{ap}} \mathrm{d}x\ \mathrm{d}yI \otimes \mathrm{PSF}},$$

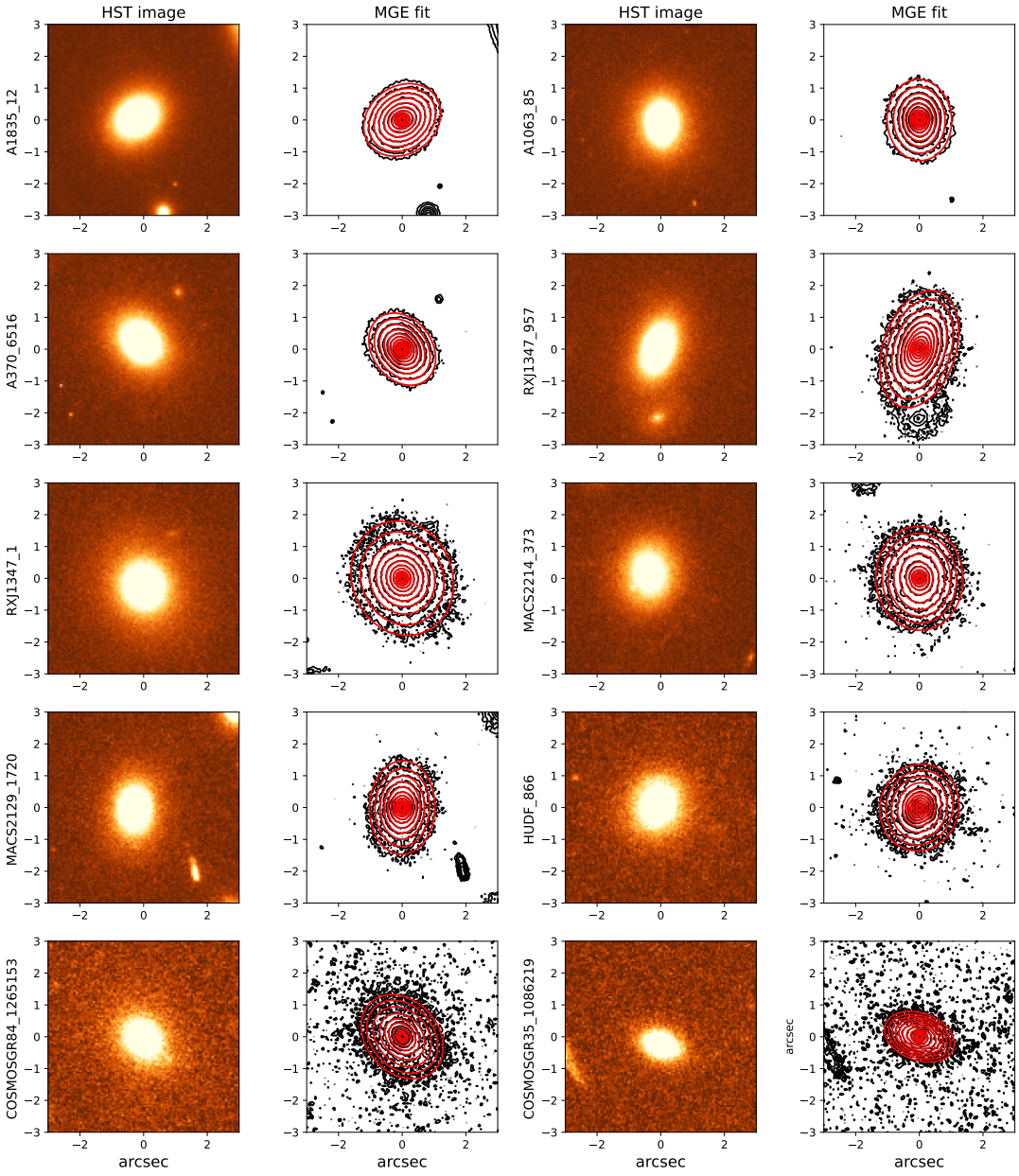


Figure 5.1: Example of MGE fits to HST images of the MUSE galaxies at different redshift. The first and third columns show the HST image and the second and fourth columns show the corresponding MGE model contours (red curves) with observed surface brightness contours (black curves). The galaxy ID and redshifts are marked on the left side of the respective galaxy's HST image. The galaxies were selected randomly from different redshift bins.

where the symbol "⊗ PSF" denotes a convolution with the PSF. The surface brightness profile, $I(x, y)$ of the dynamical tracer works as a substitute for the surface density $S(x, y)$, since they are related only by a constant factor that cancels out in this expression.

We can compare this derived $\left\langle v_{\rm los}^2 \right\rangle_{\rm obs}$ with the observed root-mean-square velocity, $V_{\rm rms}$ defined as $V_{\rm rms} \equiv \sqrt{V^2 + \sigma^2}$, where V represents the stellar velocity and σ the stellar velocity dispersion. From this comparison, we can constrain the model parameters, such as the total density slope of the mass profile, γ, or velocity anisotropy parameter, β. To predict the velocity dispersion, we used the JAMPY package (Cappellari, 2008, 2020) with four different mass profile assumptions and a spatially constant anisotropy model. To ensure the robustness of the derived quantities, we adopted both cylindrically and spherically aligned velocity ellipsoids, as the JAMPY package accommodates both configurations. This technique models the surface brightness of the tracer population using the Multi-Gaussian Expansion (MGE) parameterization (Emsellem et al., 1994; Cappellari, 2002), which we will discuss in the next section.

5.3.2 Multi-Gaussian expansion

The JAM method requires the surface brightness information of a galaxy. We performed MGE fitting to the HST images of the galaxies to model this surface brightness. The MGE formalism of surface brightness can be written as

$$\Sigma\left(x', y'\right) = \sum_{k=1}^{N} \frac{L_k}{2\pi\sigma_k^2 q'_k} \exp\left[-\frac{1}{2\sigma_k^2}\left(x'^2 + \frac{y'^2}{q'^2_k}\right)\right]$$

where L_k, σ_k, and q'_k are the total luminosity, dispersion, and the axial ratio along the major axis of the k th Gaussian component. The advantage of this parameterization is that operations like convolution or deprojection can be carried out separately on each Gaussian component and combined later to obtain the total MGE model. The deprojection of the 2D surface brightness to the 3D intrinsic luminosity density distribution is not unique. Assuming the galaxies are oblate axisymmetric, the 2D MGE surface brightness models can be deprojected to 3D. In cylindrical coordinates the intrinsic luminosity then becomes (Cappellari, 2008, eq. 8)

$$v(R, z) = \sum_{k=1}^{N} \frac{L_k}{\left(\sqrt{2\pi}\sigma_k\right)^3 q_k} \exp\left[-\frac{1}{2\sigma_k^2}\left(R^2 + \frac{z^2}{q_k^2}\right)\right]$$

where L_k and σ_k remain the same as the 2D MGE, while q_k is the 3D intrinsic axial ratio of the k th Gaussian component, written as

$$q_k = \frac{\sqrt{q_k'^2 - \cos^2 i}}{\sin i}.$$

Reversing the above equation, the inclination ($i = 90°$ being edge-on) can then be calculated as

$$\tan^2 i = \frac{1 - q_{\rm min}'^2}{q_{\rm min}'^2 - q_{\rm min}^2},$$

where $q'_{\rm min} = \min\left(q'_k\right)$ and $q_{\rm min} = \min\left(q_k\right)$ is the minimum axial ratio of the projected 2D and intrinsic 3D Gaussian components respectively.

In this work, we utilized the MGEFIT python package (Cappellari, 2002) to generate the MGE models. A series of steps were carried out on each sky-subtracted HST image of the galaxy. First, the FIND_GALAXY routine from this package was used to get the galaxy center, position angle (PA), and ellipticity. Then, we use the SECTORS_PHOTOMETRY function to measure the average surface brightness of the galaxy at various radii and angles from its center. This is performed only up to a region where the photon count is at least 1σ above the background. This is implemented by using the keyword 'minlevel' in the function. The sector-based approach helps to mitigate effects like irregularities and asymmetries due to dust by averaging the brightness over angular sectors, leading to a smoother and more representative profile. After that, we performed a regularised fit to the surface brightness profiles at different sectors using the routine MGE_FIT_SECTORS_REGULARIZED. Regularization ensures that the model uses the fewest number of Gaussian components with a narrower range of axial ratios while maintaining a solution that closely approximates the best-fit model. In this step, we assume that the PA is the same for each Gaussian component. The MGE models were analytically convolved with the corresponding PSFs and the fits were optimized against the observed galaxy surface brightness. The PSF for each galaxy was measured by conducting an MGEfit to a moderately bright (to avoid saturation of detector's pixels) star in the field of the corresponding image.

In general, if one only wants to measure the total density slope then the scaling of the luminous component or the underlying gravitational potential is irrelevant. However, if we want to constrain the dynamical mass-to-light ratios (M/L) of the galaxies then the correction of the MGE models is necessary. In any case, the total count, C of each Gaussian component in image units was

normalized to a peak surface brightness, C_0 following

$$C_0 = \frac{C}{2\pi\sigma^2 q}.$$

The width, σ of each Gaussian component was also converted from pixel to the observed unit (arcsec) by multiplying with the appropriate pixel scale. To apply the correction, the normalized surface brightness of the MGE models was first converted to AB magnitude and then treated for the extinction effects. After that, the surface brightness was multiplied by $(1 + z)^3$, with z being the galaxy redshift, to account for both the $(1 + z)^4$ bolometric cosmological dimming and the redshifting of the bandpass in the AB system. As the MUSE galaxies are at significant redshift, I also applied a K-correction (Hogg et al., 2002). The K-correction relates the observed photometry at a particular bandpass to its intrinsic value at the rest-frame bandpass. For the K-correction, I used the luminosity measured from the redshifted solar spectrum in the same HST band as the observed galaxy.

5.3.3 Mass models and kinematic anisotropy

5.3.3.1 Constant anisotropy

To simplify the dynamical models, we adopted a spatially constant kinematic anisotropy for both cylindrical and spherical alignments of the velocity ellipsoid. For the cylindrical case, the anisotropy is defined as $\beta = 1 - \frac{\sigma_z^2}{\sigma_R^2}$ and parameterized by the ratio $\frac{\sigma_z}{\sigma_R}$ during dynamical analysis. Similarly, in spherical coordinates, the anisotropy is defined as $\beta = 1 - \frac{\sigma_\theta^2}{\sigma_r^2}$ and parameterized by the ratio $\frac{\sigma_\theta}{\sigma_r}$. We found that this simplest anisotropy model could reproduce the observed v_{rms} data quite well. In each dynamical model, the velocity dispersion ratio (σ_z/σ_R or σ_θ/σ_r) was thus treated as a free parameter. Following Zhu et al. (2023), we impose a boundary on this parameter such that $\mathcal{R}(q) < \sigma_z/\sigma_R < 1$ and $\mathcal{R}(q) < \sigma_\theta/\sigma_r < 2$, where $\mathcal{R}(q) = \sqrt{0.3 + 0.7q}$ and q is the intrinsic axial ratio.

The gravitational potential, Φ in the reduced Jeans equations is determined by the assumed mass distribution of the galaxy. This mass profile represents both the stellar and dark matter components of the total mass. We have set the mass of the black hole at the center of the galaxy to zero. Next, we describe the four mass models used in this analysis.

Table 5.1: The eight models with the parameters and parameter boundaries. $\mathrm{JAM_{cyl}}$ denotes a dynamical model with the cylindrical alignment of the velocity ellipsoid and $\mathrm{JAM_{sph}}$ is for spherical orientation. The anisotropy parameter for a $\mathrm{JAM_{cyl}}$ or a $\mathrm{JAM_{sph}}$ model is σ_z/σ_R or σ_θ/σ_r respectively. q'_{min} is the minimum observed axial ratio and $\mathcal{R}(q)$ is the empirical lower limit of the velocity dispersion ratio.

Models	Free parameters					
	q_{min}	$\frac{\sigma_z}{\sigma_R}$ or $\frac{\sigma_\theta}{\sigma_r}$	$\lg\left[\frac{M}{L}\right]\left[\frac{\mathrm{M}_\odot}{\mathrm{L}_\odot}\right]$	ρ_s	f_{DM}	γ
$\mathrm{JAM_{cyl}}$ + MFL	$[0.05, q'_{\mathrm{min}}]$	$[\mathcal{R}(q), 1]$	$[-2, 2]$	-	-	-
$\mathrm{JAM_{sph}}$ + MFL	$[0.05, q'_{\mathrm{min}}]$	$[\mathcal{R}(q), 2]$	$[-2, 2]$	-	-	-
$\mathrm{JAM_{cyl}}$+ power-law	$[0.05, q'_{\mathrm{min}}]$	$[\mathcal{R}(q), 1]$	-	[0, 4]	-	[-0.5, 4]
$\mathrm{JAM_{sph}}$ + power-law	$[0.05, q'_{\mathrm{min}}]$	$[\mathcal{R}(q), 2]$	-	[0, 4]	-	[-0.5, 4]
$\mathrm{JAM_{cyl}}$ + NFW	$[0.05, q'_{\mathrm{min}}]$	$[\mathcal{R}(q), 1]$	$[-2, 2]$	-	[0, 1]	-
$\mathrm{JAM_{sph}}$ + NFW	$[0.05, q'_{\mathrm{min}}]$	$[\mathcal{R}(q), 2]$	$[-2, 2]$	-	[0, 1]	-
$\mathrm{JAM_{cyl}}$ + gNFW	$[0.05, q'_{\mathrm{min}}]$	$[\mathcal{R}(q), 1]$	$[-2, 2]$	-	[0, 1]	[0, 1.6]
$\mathrm{JAM_{sph}}$ + gNFW	$[0.05, q'_{\mathrm{min}}]$	$[\mathcal{R}(q), 2]$	$[-2, 2]$	-	[0, 1]	[0, 1.6]

5.3.3.2 Mass-follows-light model

The mass-follows-light (MFL) model is widely used to estimate the mass distribution within a galaxy. This model assumes that a galaxy's mass distribution closely follows its light distribution, meaning that brighter regions of the galaxy contain more mass than less bright regions. Consequently, the galaxy's mass distribution can be measured by multiplying the total MGE luminosity by a spatially constant mass-to-light ratio, M/L. A dynamical model with MFL mass distribution is described by three free parameters: (1) the velocity dispersion ratio, (2) the minimum intrinsic axial ratio q_{min} to parameterize the inclination, and (3) the dynamical mass-to-light ratio M/L.

5.3.3.3 Power law model

In this model, the total mass density ($\rho(r)$) is described by a simple power-law function of the form

$$\rho(r) = \rho_s \left(\frac{r}{r_s}\right)^{-\gamma}.$$

where r is the radius from the galaxy center, γ is the slope of the density profile, r_s is the 'break' radius and ρ_s is the density at the break radius. This model is particularly useful because it provides a straightforward way to characterize how the total mass density decreases with distance from the center of the galaxy, capturing both the central concentration dominated by the stellar mass and the

extended halo containing mostly DM. The break radius was set to a distance of 20 kpc as it had been observed that this parameter does not affect the dynamical analysis significantly (e.g. Bellstedt et al., 2018; Derkenne et al., 2021). This dynamical model contains four free parameters: (1) the velocity dispersion ratio, (2) the minimum intrinsic axial ratio $q_{\rm min}$, (3) the total density slope, γ and (4) the density at break radius, ρ_s.

5.3.3.4 MFL with NFW dark matter halo

This model provides additional flexibility than the above two models by decomposing the contributions of the stellar mass and DM to the overall mass distribution of the galaxy. Like the MFL model, the stellar mass is measured from surface brightness scaled by a uniform dynamical mass-to-light ratio M/L. However, the DM content is characterized by assuming a spherical dark matter halo described by the Navarro-Frenk-White (NFW) profile (Navarro et al., 1996). The NFW profile is defined as

$$\rho_{\rm DM}(r) = \rho_s \left(\frac{r}{r_s}\right)^{-1} \left(\frac{1}{2} + \frac{1}{2}\frac{r}{r_s}\right)^{-2}$$

where r is the distance from the center of the galaxy, r_s is the characteristic radius and ρ_s is the characteristic density such that $\rho_{\rm DM}(r) = \rho_s$ at $r = r_s$. The characteristic radius, r_s was fixed at 20 kpc rather than treating it as a free parameter for the reason mentioned above. Additionally, the characteristic density, ρ_s which works as a scaling factor for the NFW profile could be uniquely determined from the M/L and DM fraction f_{DM}. Thus, it is more convenient to sample the DM fraction with the limit $0 < f_{DM} < 1$ rather than choosing an arbitrary limit for ρ_s. Hence, this model depends on four free parameters: (1) the velocity dispersion ratio, (2) the minimum intrinsic axial ratio, (3) the stellar mass-to-light ratio M/L, and (4) the DM fraction f_{DM}.

5.3.3.5 MFL with gNFW dark matter halo

To measure the total density slope with a more flexible model than the power law or MFL plus NFW profile, I adopt a generalized NFW (gNFW; Wyithe et al., 2001) profile. The difference between this model and the previous one is that the inner density slope of the DM halo within the characteristic radius is not fixed and can account for the baryonic effect within the inner region of the halo. The gNFW profile can be described as

$$\rho_{\rm DM}(r) = \rho_s \left(\frac{r}{r_s}\right)^{-\gamma} \left(\frac{1}{2} + \frac{1}{2}\frac{r}{r_s}\right)^{\gamma-3}$$

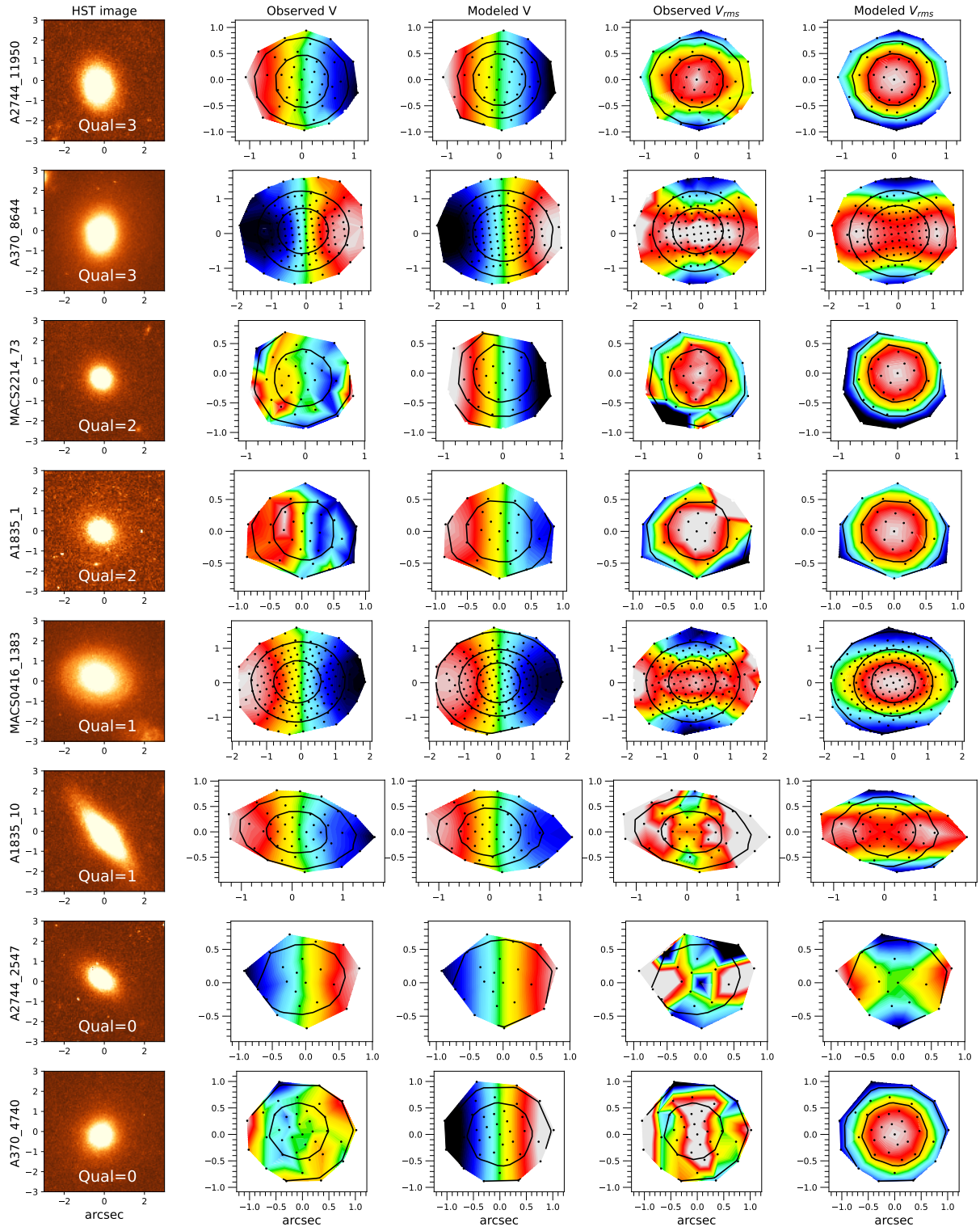
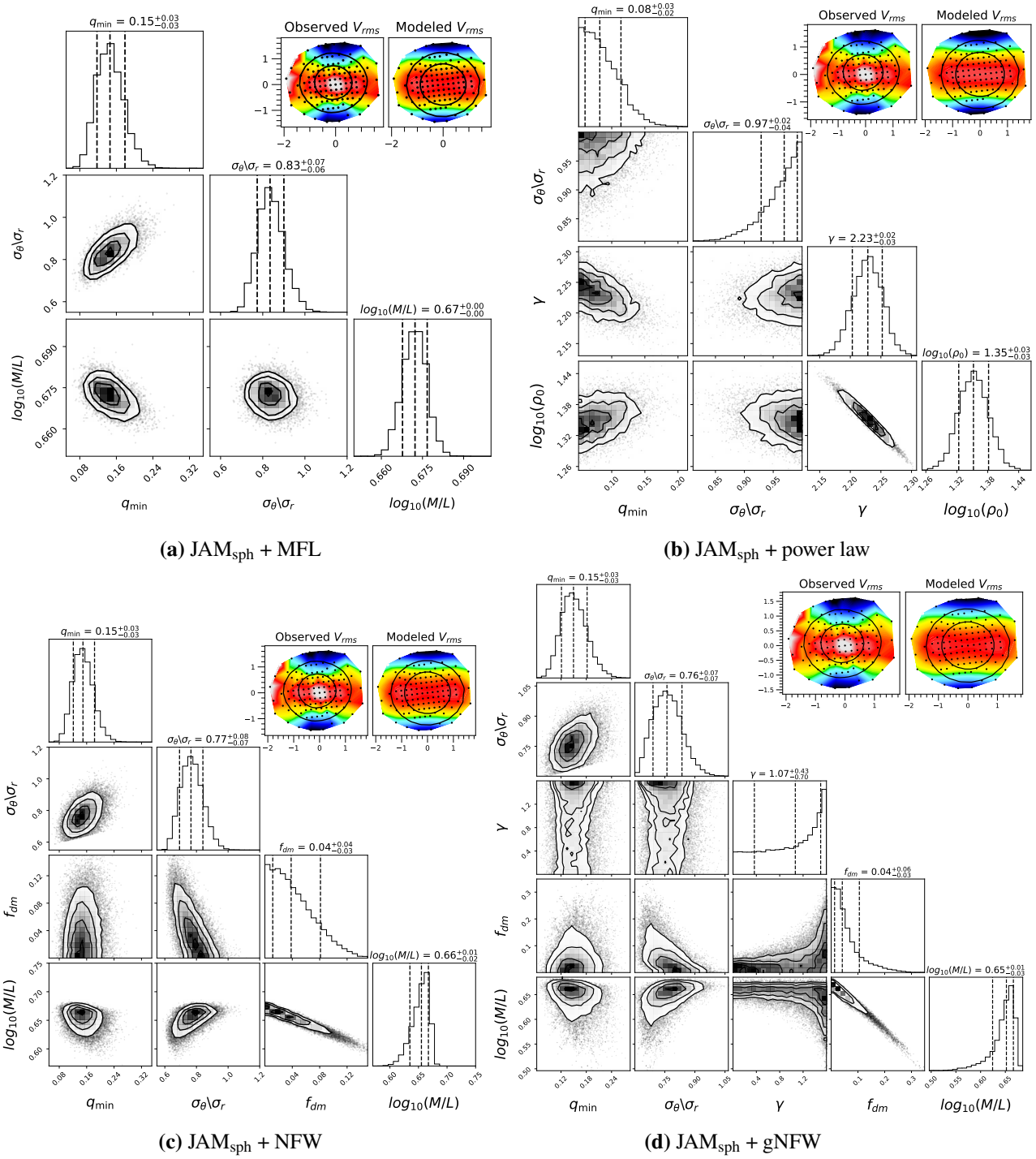


Figure 5.2: Example of galaxies with different qualities of JAM fit (Qual=3, 2, 1, and 0). Each row represents a galaxy and for each galaxy, the HST image, observed and recovered V and V_{rms} fields are presented. The black curves show the observed and modeled surface brightness contours in respective kinematic maps. Both the observed and modeled kinematic maps are rotated such that the major axis of a galaxy aligns with the image's x-axis. Note that the quality of fit decreases from Qual=3 to Qual=0.



(a) JAM_{sph} + MFL

(b) JAM_{sph} + power law

(c) JAM_{sph} + NFW

(d) JAM_{sph} + gNFW

Figure 5.3: Example of corner plots for galaxy A370_8644. Each plot represents a JAM model with one of the four mass profiles (MFL, power law, NFW, and gNFW) and the spherical orientation of the velocity ellipsoid. The black-dashed lines show the 16th, 50th, and 84th percentiles of each posterior distribution. Additionally, the observed and modeled V_{rms}, using the median parameter set of the corresponding model, is also displayed on the right side of the individual corner plot.

where $\gamma = 1$ reduces to an NFW profile. Similar to the NFW model, r_s was set to 20 kpc and ρ_s was measured from the M/L and DM fraction f_{DM}. Therefore, this model contains five free parameters: (1) the velocity dispersion ratio, (2) the minimum intrinsic axial ratio, (3) the stellar mass-to-light ratio M/L, and (4) the DM fraction f_{DM}, and (5) γ.

A summary of the models, including the boundaries on the parameters, is presented in Table 5.1.

5.3.4 Fitting procedure

We constrained the dynamical properties of the MUSE sample, such as M/L and γ, by fitting the observed LOS V_{rms} data of the galaxies. To achieve this, we used eight JAM models (see Table 5.1) to predict the LOS velocity dispersion. The fitting was carried out in two steps. Initially, a JAM_{cyl} plus MFL model was employed to fit the observed kinematics of each galaxy. This step aimed to exclude the problematic Voronoi bins from the kinematic maps and assess the quality of the fit. A least-square method, implemented via `scipy.optimize.least_squares`, was utilized for this purpose. The least-square fitting was performed iteratively with sigma clipping. At each iteration, first, an optimal fit was found, and then the Voronoi bins exceeding 3σ deviations above the noise were clipped. This process was repeated until convergence, defined as no new bins being clipped in subsequent iterations. The noise at each iteration was calculated as a bi-weight estimate (Hoaglin et al., 1983) from the residual of the fit. All bins clipped up to this stage were excluded from further analysis. Additionally, the fitted models from this step were used for a quality-of-fit classification. By visually inspecting the recovered V and V_{rms} maps with the MFL model, we divided the galaxies into four groups based on the fit quality.

I classified the modeling quality into four categories: 0, 1, 2, and 3, according to the following criteria. Galaxies classified as Qual = 3 exhibited well-recovered V and V_{rms} maps and these were typically fast rotators. For Qual = 2 galaxies, the predicted V_{rms} maps were of similar quality to those of Qual = 3, but the fitted V maps were not as accurate. This discrepancy is often because these galaxies are mostly slow rotators, and the dynamical models could not adequately represent their V fields. Qual = 1 fits produced V_{rms} maps that were less accurate than those of Qual = 2 or 3 but still showed some resemblance to the observed V_{rms} maps. In these cases, the recovered V maps typically matched the data well, except when the galaxy was a slow rotator. Lastly, galaxies for which the modeled V_{rms} maps did not closely resemble the observed V_{rms} maps were classified

as Qual = 0 regardless of the quality of modeled V. In Fig. 5.2, I show examples of galaxies with different JAM modeling qualities.

Among the 180 galaxies in our MUSE sample, I found that 108 galaxies had a fit quality of 1 or higher. Galaxies with this level of fit quality can reasonably reproduce the kinematics maps, at least based on visual inspection. Therefore, for the next step, I focused on fitting the observed $V_{\rm rms}$ maps of these 108 galaxies using eight JAM models. At this stage, we used a Bayesian inference method implemented via the `emcee` Python package (Foreman-Mackey et al., 2013). This approach allowed us to estimate covariances among the model parameters and derive uncertainties from their posterior distributions. According to Bayes' theorem, the posterior probability distribution of a parameter, θ under a model H and data D is

$$P(\boldsymbol{\theta} \mid \boldsymbol{D}) \propto P(\boldsymbol{D} \mid \boldsymbol{H}(\boldsymbol{\theta}))P(\boldsymbol{\theta})$$

where $P(\boldsymbol{D} \mid \boldsymbol{H}(\boldsymbol{\theta}))$ is the likelihood of the data, and $P(\boldsymbol{\theta})$ is the prior on the parameter of the model. The likelihood $P(\boldsymbol{d} \mid \boldsymbol{p})$, produced by the JAM package for a particular model, is proportional to $\exp\left(-\frac{\chi^2}{2}\right)$, where χ^2 is defined as

$$\chi^2 = \sum_j \left[\frac{\left(\overline{v^2_{{\rm los},j}}\right)^{1/2} - V_{{\rm rms},j}}{\varepsilon_{V_{{\rm rms},j}}} \right]^2$$

Here $\overline{v_{{\rm los},j}}$ is the modeled LOS velocity dispersion, $V_{{\rm rms},j}$ is the observed RMS velocity and $\varepsilon_{V_{{\rm rms},j}}$ is the measured uncertainty of the observed RMS velocity in the j th Voronoi bin. The summation included all Voronoi bins except those removed in the previous step. To obtain the posterior distributions, I used the Markov Chain Monte Carlo (MCMC) method within the Bayesian framework. I opted to run 30 independent walkers for a maximum of 10,000 steps. However, a chain could terminate earlier if it was deemed converged based on a predetermined auto-correlation time estimate. I employed flat (uninformed) priors for all model parameters, meaning the likelihood of a model was determined solely by the χ^2 statistics. Figure 5.3 presents the corner plots for four different JAM models applied to the same galaxy.

5.3.5 Measuring dynamical quantities

I measured several dynamical quantities using the JAM models, including the mass-weighted total density slope, $\overline{\gamma}$, total dynamical mass, M_T, and stellar mass, M_* and dynamical mass-to-light (M/L)

within 1 R_e. The dynamical mass, M_T, and stellar mass, M_* were calculated analytically using the MGE_RADIAL_MASS routine in the JAMPY package. For these calculations, the median model parameters from the posterior distributions were utilized. The dynamical (M/L) is defined as the ratio between M_T and the total luminosity within a sphere of R_e. I estimated the total density slope,$\overline{\gamma}$ as a mass-weighted quantity (Dutton & Treu, 2014) such that

$$\overline{\gamma} \equiv \frac{1}{M_{\rm T}\,(<R_{\rm e})}\int_0^{R_{\rm e}} -\frac{{\rm d}\lg\rho_{\rm T}}{{\rm d}\lg r}4\pi r^2\rho_{\rm T}(r){\rm d}r = 3 - \frac{4\pi R_{\rm e}^3\rho_{\rm T}\,(R_{\rm e})}{M_{\rm T}\,(<R_{\rm e})}.$$

where $\rho_{\rm T}(r)$ is the radially averaged density and was computed analytically from the median model parameters of the posterior distributions as above using the MGE_RADIAL_DENSITY function within JAMPY. The R_e values were measured from MGE models in chapter 3. Though all eight models were employed to measure the dynamical quantities, the two MFL models were excluded from measuring $\overline{\gamma}$ because, in these cases, the total density slopes are fixed by their luminosity density slopes and do not vary as a model parameter.

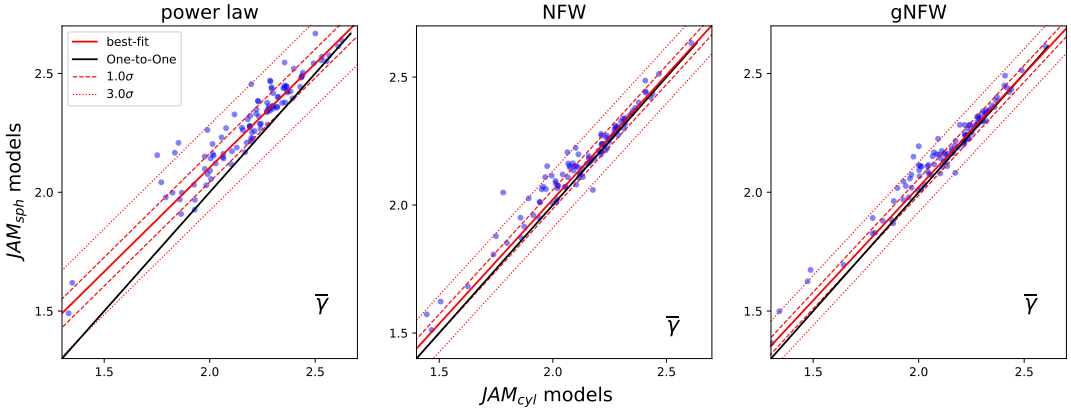


Figure 5.4: Comparison of measured $\overline{\gamma}$ values between the $\rm JAM_{cyl}$ and $\rm JAM_{sph}$ models with three different mass profiles. Left: comparison between JAM models with power-law mass profile, Middle: comparison between JAM models with NFW profile, and Right: comparison between gNFW models with different orientations. In each plot, the black line denotes the one-to-one line, the red solid line represents the best-fit line, while the red dashed and red dotted lines indicate the 1σ and 3σ intrinsic scatter, respectively. The coefficients of the best-fit lines and intrinsic scatters were measured using the LtsFit python package (Cappellari et al., 2013b). In all three cases the one-to-one line shows that the JAM models with spherical velocity ellipsoid orientations tend to yield higher estimates of the total density slope than their cylindrical counterparts with the same mass profile. This discrepancy is more pronounced in the power-law models than in the NFW and gNFW models. The MFL model was excluded because, in this case, the total density slopes are uniquely determined by their luminosity density slopes and do not vary with JAM models.

5.4 Results and discussion

In this work, I primarily focused on studying the probable trend of evolution in the total density slope of ETG galaxies within the MUSE sample over cosmic time. To get a robust estimate of $\overline{\gamma}$ I used two extreme assumptions on the orientation of the velocity ellipsoid, namely $\mathrm{JAM_{cyl}}$ and $\mathrm{JAM_{sph}}$, with three different mass profiles, resulting in six different JAM models (note that two MFL models were not used to measure $\overline{\gamma}$). Each model then yielded an independent estimate of $\overline{\gamma}$ for each sample galaxy. In this section, we first compare measurements from different JAM models to assess the consistency of the derived $\overline{\gamma}$. Previous studies found that the $\overline{\gamma}$ could be correlated to other morphological and structural properties (e.g. Derkenne et al., 2021; Sonnenfeld et al., 2013). I also checked whether such linear relations exist within the MUSE sample between $\overline{\gamma}$ and other properties such as central velocity dispersion, σ_e, effective radius, R_e, total mass, M_{tot}, stellar mass, M_* and surface mass density Σ. I then compared the observed trends in my sample with the ones found in other dynamic and lensing samples. After that, I evaluated the change in total density slopes as a function of redshift, $\mathrm{d}\overline{\gamma}/\mathrm{d}z$, within the MUSE sample and compared it with other works. Previous dynamical studies found no significant change in $\overline{\gamma}$ over redshift by comparing to samples from the local Universe (Derkenne et al., 2021, 2023). However, these dynamical modeling-based works lack a sample over a wide redshift range to evaluate $\mathrm{d}\overline{\gamma}/\mathrm{d}z$ at intermediate redshift. Contrarily, strong lensing-based studies cover a larger redshift range and suggest a non-negligible $\mathrm{d}\overline{\gamma}/\mathrm{d}z$ over cosmic time where the slope becomes steeper at low redshift (Auger et al., 2010; Sonnenfeld et al., 2013; Li et al., 2018). In this work, I found that when the MUSE sample was combined with other dynamical studies, it suggested a picture in discord with the lensing but agreed with the cosmological simulations. However, when the dynamical and lensing samples were combined, the results aligned more closely with those obtained from the lensing data, which is expected, since the lensing sample dominates both ends of the considered redshift range.

5.4.1 Comparing different JAM models

To assess the consistency of measured $\overline{\gamma}$ values, I first compared estimates from the same mass decomposition assumptions, namely power-law, NFW, and gNFW models with different velocity ellipsoid alignments ($\mathrm{JAM_{cyl}}$ vs $\mathrm{JAM_{sph}}$). The comparison is presented in Fig. 5.4. In each plot, the

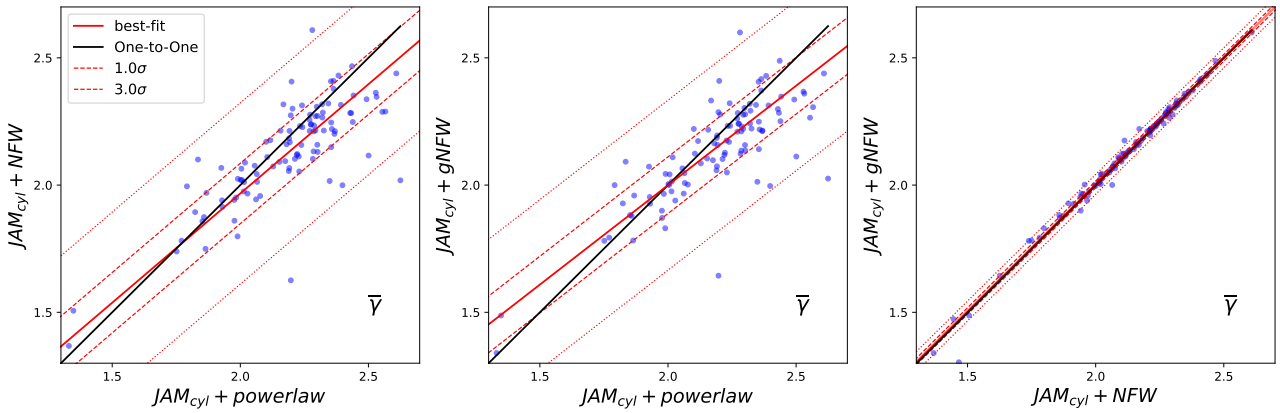


Figure 5.5: Comparison of measured $\overline{\gamma}$ values from three different $\mathrm{JAM_{cyl}}$ models. Left: comparison between $\mathrm{JAM_{cyl}}$ + MFL model and $\mathrm{JAM_{cyl}}$ + power law model, Middle: comparison between $\mathrm{JAM_{cyl}}$ + gNFW model and $\mathrm{JAM_{cyl}}$ + power law model, and Right: comparison between $\mathrm{JAM_{cyl}}$ + gNFW and $\mathrm{JAM_{cyl}}$ + NFW model. The description of the plots is the same as Fig. 5.4. The measurements from the NFW and gNFW models are mostly consistent with each other with observed RMS scatter of 0.01. However, the power-law model shows more deviation from the other two mass profiles and tends to overestimate the $\overline{\gamma}$ values compared to both the NFW and gNFW models.

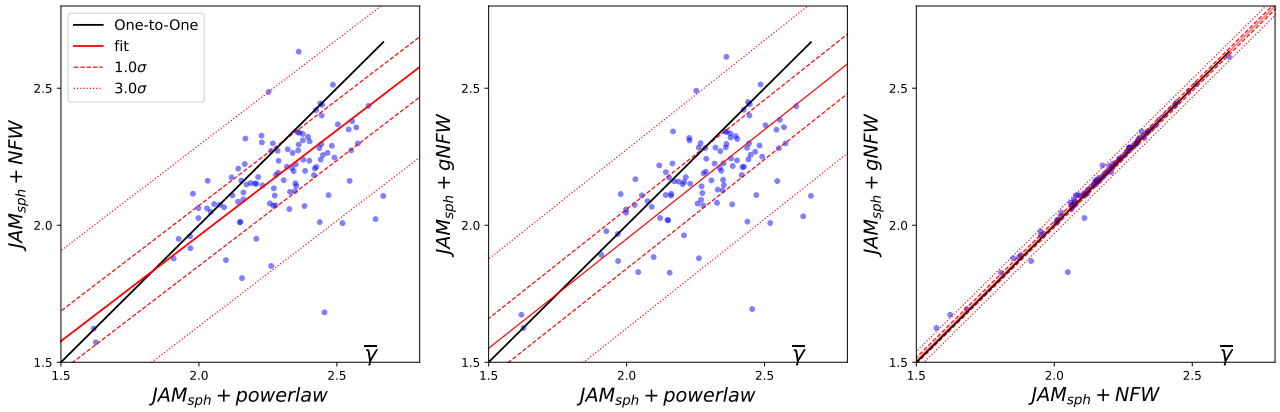


Figure 5.6: Comparison of measured $\overline{\gamma}$ quantities from three different $\mathrm{JAM_{sph}}$ models. Left: comparison between $\mathrm{JAM_{sph}}$ + MFL model and $\mathrm{JAM_{sph}}$ + power law model, Middle: comparison between $\mathrm{JAM_{sph}}$ + gNFW model and $\mathrm{JAM_{sph}}$ + power law model, and Right: comparison between $\mathrm{JAM_{sph}}$ + gNFW and $\mathrm{JAM_{sph}}$ + NFW model. Similar to the cylindrical case, the tightest correlation is observed between the NFW and gNFW models, and the power-law model shows more deviation from the other two mass profiles and tends to overestimate the $\overline{\gamma}$ values compared to both the NFW and gNFW models. The description of the plots is the same as Fig. 5.4.

black line shows the one-to-one line, red solid line represents the best-fit line, and the red dashed and red dotted lines indicate the 1σ and 3σ intrinsic scatter from the best-fit line, respectively. The coefficients of the best-fit lines and intrinsic scatters were measured using the LtsFit python package (Cappellari et al., 2013b). The one-to-one lines show that the JAM models with spherical

velocity ellipsoid orientations tend to yield higher estimates of the total density slope than their cylindrical counterparts with the same mass profile. This discrepancy is more pronounced in the power-law models than in the NFW and gNFW models. The spherical orientation on average provides a 5% higher estimate than the cylindrical orientation for the power-law models. However, for both the NFW and gNFW models, the one-to-one line aligns with the best-fit line above $\overline{\gamma}$= 2.1. The observed RMS scatter between measurements from the NFW and gNFW models with the two orientations are Δ = 0.03 and 0.04 respectively, while the power-law models show a slightly higher scatter of, Δ = 0.07. These comparisons suggest that the measured $\overline{\gamma}$ quantities are largely independent of the assumed velocity ellipsoid orientations except for the power-law models.

Additionally, I also compared outcomes from different mass models with the same velocity ellipsoid orientations. Fig. 5.5 and 5.4 show the comparison among different mass profile assumptions with $\mathrm{JAM_{cyl}}$ and $\mathrm{JAM_{sph}}$ alignment respectively. For both velocity ellipsoid orientations, the NFW and gNFW models are mostly consistent with each other, as in both cases the one-to-one line aligns with the best-fit line. For these two mass models the slope of the best-fit lines is 1 and the measured 1σ scatters for $\mathrm{JAM_{cyl}}$ and $\mathrm{JAM_{sph}}$ case is Δ = 0.011 and 0.013 respectively. The tightest relations among these two models are understandable as one is the modified version of the other. However, it is reassuring to see that as before the results from these two models are highly consistent irrespective of the choice of velocity ellipsoid orientation. In contrast, the power-law model shows more deviation from the other two mass profiles, regardless of the chosen velocity alignment. The power-law models tend to overestimate the $\overline{\gamma}$ values compared to both the NFW and gNFW models, with this tendency being more pronounced in the spherical models than in the cylindrical ones. The intrinsic RMS scatters between the power-law model and the other two models are approximately 0.1 for both velocity orientations. Overall, these comparisons suggest that the power-law models tend to overestimate the $\overline{\gamma}$ values, particularly in the spherical orientation, whereas the measurements from the NFW and gNFW models remain mostly consistent and are not biased toward a specific mass model or velocity ellipsoid orientations.

5.4.2 Correlations of total density slope with galaxy properties

The total density slopes measured from the ETG samples at intermediate redshift, studied both by gravitational lensing and dynamical modeling-based methods, showed some type of correlation with one or more morphological and structural galaxy properties. It is essential to take into account

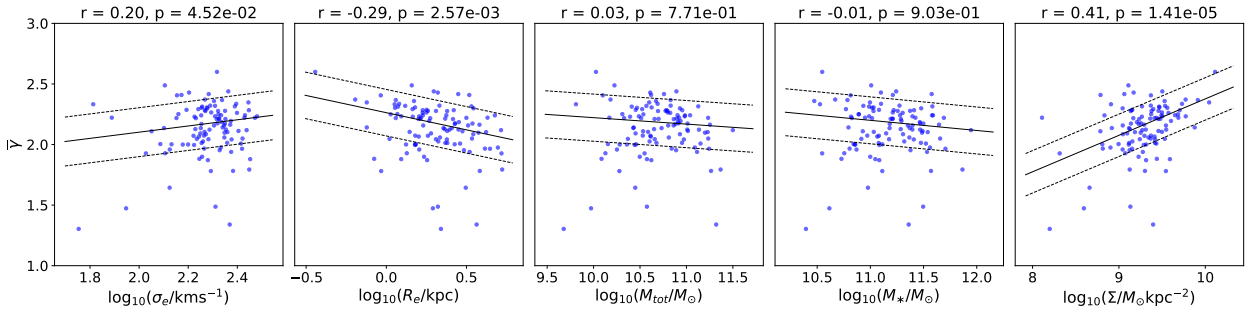


Figure 5.7: Observed linear correlation between the total density slope, $\overline{\gamma}$ and other galaxy properties: central velocity dispersion, σ_e, effective radius, R_e, total mass, M_{tot}, stellar mass, M_* and stellar surface mass density Σ. The best-fitting parameters, corresponding errors, and Pearson coefficients with p-values were measured using the LtsFit package. In each plot, the black solid line represents the best-fit line and the black dashed lines are 1σ observed intrinsic scatter from the best-fit while the outliers were clipped at 3σ level. The resulting Pearson correlation coefficients from the fits and corresponding p-values are printed at the top of each plot. The stellar surface mass density and dynamical total mass were measured in this Chapter while other properties were defined in Chapter 3. Among the five galaxy parameters, only R_e and Σ show significant correlation with $\overline{\gamma}$.

such correlations as they may also affect the observed time evolution of $\overline{\gamma}$. Therefore, I also examined whether such linear relations exist within the MUSE sample between $\overline{\gamma}$ and other galaxy parameters using the LtsFit package. Fig. 5.7 depicts these correlations with galaxy properties such as central velocity dispersion, σ_e, effective radius, R_e, total mass, M_{tot}, stellar mass, M_* and surface mass density Σ. The resulting Pearson correlation coefficients from the fits and corresponding p-values are printed at the top of each plot. The adopted total dynamical mass for this analysis was measured using the $\mathrm{JAM_{cyl}}$ + gNFW model because other dynamical studies that I compared my observations with used a similar model. The galaxy properties, σ_e, R_e, and M_*, were defined in Chapter 3 and the stellar surface mass density was defined as

$$\Sigma = \frac{M_{tot}}{2\pi R_e^2}. \tag{5.4}$$

I observed a slight trend with the stellar velocity dispersion with high dispersion galaxies having steeper observed density slopes ($\mathrm{d}\overline{\gamma}/\mathrm{dlog}_{10}\sigma_e = 0.26 \pm 0.15$). Among the dynamical studies, the Frontier Fields sample showed a steeper relation than the MUSE with $\mathrm{d}\overline{\gamma}/\mathrm{dlog}_{10}\sigma_e = 0.62 \pm 0.16$ while the MAGPI sample showed a similar but weaker relation than MUSE. From the lensing side, the SLACS sample also showed no pronounced trend with $\mathrm{d}\overline{\gamma}/\mathrm{dlog}_{10}\sigma_{e/2} = 0.07 \pm 0.08$ (Auger et al., 2010).

The effective radius showed a statistically significant correlation with $\overline{\gamma}$ where a galaxy with

smaller R_e on average has steeper density slopes ($d\overline{\gamma}/d\log_{10}R_e = -0.28 \pm 0.07$). A similar trend was also found in lensing-based SLACS, SL2S, and other samples. For example, Sonnenfeld et al. (2013) observed that at fixed z and stellar mass, the density slope has a comparatively steeper relation with the effective radius such that $d\overline{\gamma}/d\log_{10}R_e = -0.76 \pm 0.15$ and using only SLACS sample Auger et al. (2010) found a trend of $d\overline{\gamma}/d\log_{10}R_e = -0.41 \pm 0.12$. However, neither the Frontier Field nor MAGPI samples showed any significant correlation with R_e.

Among the five galaxy parameters that I compared, the surface mass density showed the most statistically significant correlation with $\overline{\gamma}$. The other dynamical and lensing samples, except for the MAGPI sample, yielded similar strong trends, indicating objects with more concentrated stellar distributions, and thus higher Σ, also exhibit steeper total density slopes. The gradients observed in different samples are $d\overline{\gamma}/d\log_{10}\Sigma = 0.30 \pm 0.05$ for the MUSE sample, $d\overline{\gamma}/d\log_{10}\Sigma = 0.18 \pm 0.05$ for the Frontier Field sample and at fixed redshift $d\overline{\gamma}/d\log_{10}\Sigma = 0.38 \pm 0.07$ for the SL2S sample.

I found a mild negative to no trend between $\overline{\gamma}$ and mass parameters M_{tot} and M_*, similar to other samples. In all cases, the more massive galaxies tend to have shallower total density slopes. However, Sonnenfeld et al. (2013) showed that the stellar mass is a steep function of redshift and the negative trend seen is the result of the selection effect. I assume this is also the case for MUSE and other samples and did not investigate any further.

To summarize, I found that the MUSE sample exhibits similar trends found in other lensing and dynamical-based samples. The MAGPI sample did not show any particular trend perhaps due to its small sample size. The lensing studies (e.g. Sonnenfeld et al., 2013; Li et al., 2018) took the correlation of $\overline{\gamma}$ with R_e and Σ into account and still found significant evolution with lookback time. In this work, I estimated the redshift evolution of $\overline{\gamma}$ without considering such systematic correlation effects and will investigate these effects further in future works.

5.4.3 Redshift evolution within the MUSE sample

The evolution of the total density slope at intermediate redshift is an open question as the findings from cosmological simulations and strong lensing-based observational studies do not agree (Remus et al., 2017; Wang et al., 2019; Derkenne et al., 2021). To explore this discrepancy, I measured the trend of evolution in the total density slopes as a function of redshift within the MUSE sample. The total density slope, $\overline{\gamma}$ values were measured employing six JAM models that differ in mass distribution and alignment of the velocity ellipsoid assumptions. As above, the coefficients of the

Table 5.2: The coefficients of the best-fit lines to the measured total density slopes ($\overline{\gamma}$) using different JAM models. Each measured set of $\overline{\gamma}$ values was fitted using the relation $\overline{\gamma} = a + b_0(z - z_0)$, where z_0 is the median of the z values and Δ is the RMS deviation between the data and the fitted relation. The fitting was conducted either using galaxies of Qual=3, 2, 1 or only with Qual=3,2. The observed RMS scatters of the fits are also listed in the table. For a graphical representation of all best-fit lines see Fig. 5.8.

Models	Qual=3,2,1			Qual=3,2		
	a	b_0	Δ	a	b_0	Δ
JAM_{cyl} + power-law	2.215 ± 0.020	0.11 ± 0.15	0.25	2.247 ± 0.030	-0.46 ± 0.26	0.23
JAM_{sph} + power-law	2.297 ± 0.018	0.07 ± 0.14	0.23	2.347 ± 0.023	-0.35 ± 0.20	0.14
JAM_{cyl} + NFW	2.170 ± 0.016	-0.10 ± 0.12	0.16	2.170 ± 0.021	-0.56 ± 0.19	0.12
JAM_{sph} + NFW	2.204 ± 0.014	-0.08 ± 0.10	0.14	2.185 ± 0.020	-0.49 ± 0.17	0.12
JAM_{cyl} + gNFW	2.185 ± 0.016	-0.14 ± 0.12	0.20	2.166 ± 0.016	-0.46 ± 0.14	0.15
JAM_{sph} + gNFW	2.211 ± 0.015	-0.10 ± 0.12	0.17	2.191 ± 0.016	-0.46 ± 0.15	0.14

best-fit lines and associated RMS scatters were estimated using the LtsFit package. The uncertainty of the measured $\overline{\gamma}$ quantities for all models was estimated using a Monte Carlo (MC) method. Each MC simulation was allowed to run 100 times and each time the model parameter set to measure $\overline{\gamma}$ was determined by sampling the associated posterior distributions. The fit was initially performed considering all 108 galaxies for which dynamical modeling was carried out regardless of the quality of the fitted model. Additionally, I also conducted another fit considering only high-fit-quality galaxies (Qual=3 and 2). In Fig. 5.9, I show the measured trend of evolution in $\overline{\gamma}$ for JAM_{cyl} + gNFW and JAM_{sph} + gNFW models. I found that for both models, the slopes, $d\overline{\gamma}/dz$, derived from high-fit-quality galaxies alone are steeper than the ones from all galaxies.

The coefficients of the best-fit lines to the measured total density slopes ($\overline{\gamma}$) using different JAM models and observed RMS scatters of the fits are listed in Table 5.2. In general, the slopes, $d\overline{\gamma}/dz$, of the best-fit lines using $\overline{\gamma}$ from all galaxies, are consistent with zero. However, if I only consider the Qual 3 and 2 galaxies, then for all models the slopes to the best-fit lines are negative. The near-zero slopes of the best-fit lines from all galaxies indicate an absence of significant evolution over cosmic time at intermediate redshift ($0.2 < z < 0.8$). This is in line with the observation from the previous dynamical studies (Derkenne et al., 2021). However, these dynamical studies lack a proper sample to estimate redshift evolution at intermediate redshift and compare their measurements with samples from the local Universe. Conversely, the negative slopes from the

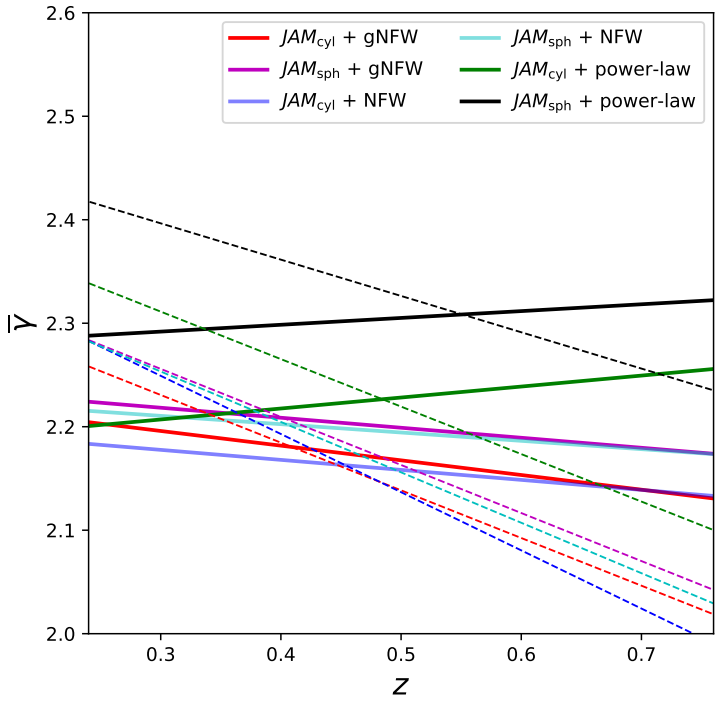


Figure 5.8: Graphical representation of the best-fit lines from the six JAM models listed in Table 5.2. For each model, the solid line shows the best-fit line obtained from fitting conducted using all of 108 galaxies and the dashed line is using galaxies with only Qual=2, 3. The slopes from Qual=2,3 galaxies in all six cases are negative and suggest that the total density slopes have become steeper with cosmic time. However, the slopes from all galaxies with either NFW or gNFW mass models are relatively less negative than ones with high-fit-quality galaxies. The slopes from power-law models with all galaxies are slightly positive. However, the slopes derived fitting all galaxies are within the 1σ uncertainty of each other and thus statistically indistinguishable.

best-fit lines with the high-fit-quality MUSE galaxies suggest that the total density slopes of ETGs have become steeper at lower redshifts, corroborating findings from the lensing studies. However, for each model, the best-fit slopes from the high-fit-quality galaxies differ by around 2σ compared to the larger sample. Therefore, a larger sample of high-fit-quality galaxies is required to make any statistically significant conclusion. It is reassuring that all six JAM models yield consistent results for the case of high-quality-fit galaxies with relatively lower intrinsic scatter. Still, further investigation is required with a bigger sample of ETGs and high-quality IFU data to make any robust conclusion about possible redshift evolution.

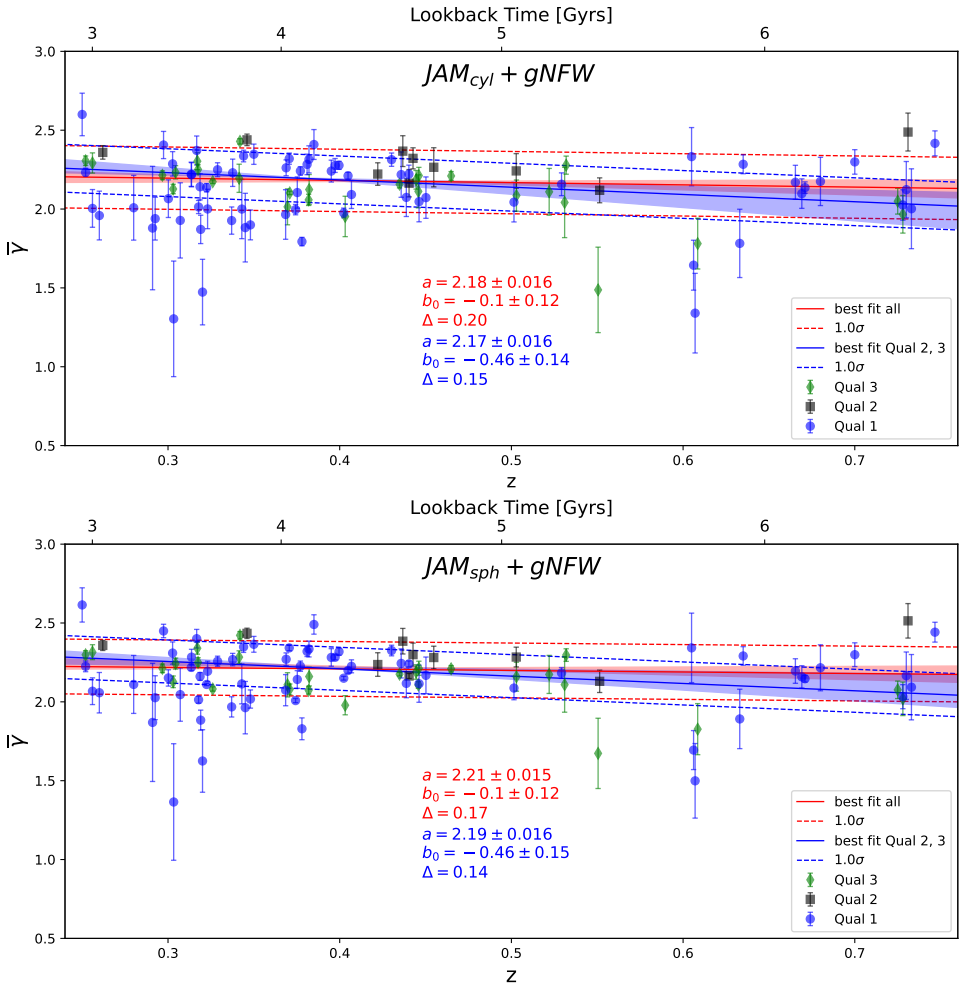


Figure 5.9: The evolution of the total density slope, $\overline{\gamma}$, as a function of redshift is depicted in two plots. The top plot shows $\overline{\gamma}$ values measured using the $\mathrm{JAM_{cyl}}$ + gNFW model, while the bottom plot uses the $\mathrm{JAM_{sph}}$ + gNFW model. In each plot, galaxies are marked based on their JAM modeling quality: green diamonds for Qual 3, black squares for Qual 2, and blue circles for Qual 1, each with associated error bars. The red solid line represents the best-fit line using $\overline{\gamma}$ values from all galaxies, whereas the blue solid line represents the best-fit line using only Qual 3 and 2 galaxies. The dashed and dotted lines indicate the 1σ and 3σ intrinsic scatter, respectively. The coefficients of the best-fit lines and intrinsic scatters were measured using the LtsFit Python package (Cappellari et al., 2013b). The shaded region shows the uncertainty associated with the best-fit line. For both models, the slope derived from high-fit-quality galaxies alone is more negative than the slope from all galaxies. However, in both cases, the best-fit lines and associated slopes are within the uncertainty of each other. The near-zero slope of the best-fit line from all galaxies suggests no significant evolution over cosmic time. Conversely, the negative slope from the best-fit line with high-fit-quality galaxies suggests that the total density slope of ETGs has become steeper at lower redshifts, corroborating findings from some lensing studies.

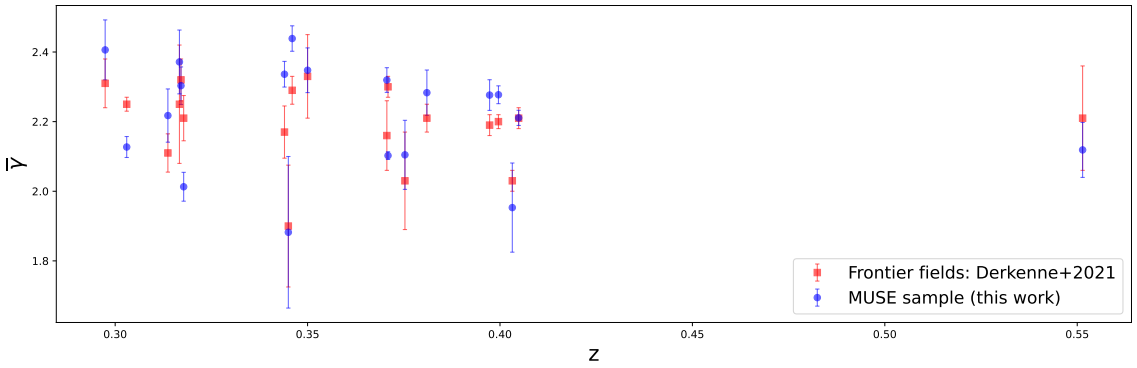


Figure 5.10: Comparison of the measured total density slope, $\overline{\gamma}$ for the overlapping galaxies from the MUSE sample (blue circles) and Frontier Field sample (red square)(Derkenne et al., 2021). The overlapping galaxies, in total 18, were identified by matching the galaxy IDs, coordinates, redshifts, and central velocity dispersions. For the MUSE sample, the measurements from the $\mathrm{JAM_{cyl}}$ + gNFW model were used as the comparison set was coming from a similar model. Although there are some differences in the underlying model assumptions and analysis processes between the two studies, in most cases, the measurements are within the 1σ uncertainty of each other.

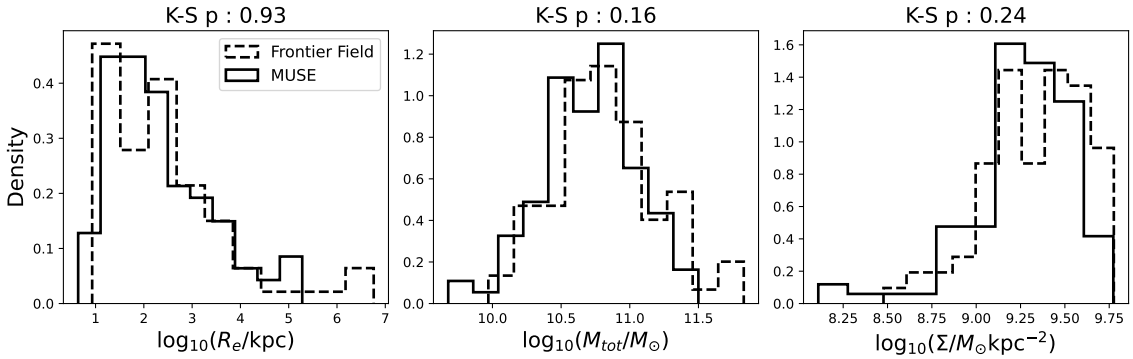


Figure 5.11: The number density histograms of the statistically matched Frontier Field (dashed line) and MUSE sample (solid line). From left to right the histograms for effective radius, R_e, total stellar mass, M_{tot}, and surface mass density Σ of the two samples are shown. The p-values of the corresponding K-S tests are shown as the title of the respective plots.

5.4.4 Redshift evolution with other dynamical and lensing studies

In the previous sections, I presented the total density slopes of the MUSE sample measured through six JAM models and showed that the models are consistent with each other. Additionally, I found that the $\mathrm{d}\overline{\gamma}/\mathrm{d}z$ from galaxies with fit quality 2 and 3 are steeper than the slope from all galaxies and mostly negative, suggesting that the $\overline{\gamma}$ have become steeper with cosmic time. In this section, I will compare and combine the MUSE sample with other samples with different methodologies and systematics from the literature to get a better picture of the evolution of the total density slope within $0.1 < z < 0.8$. I show these samples including the MUSE sample in Fig. 5.12 and the

Table 5.3: The coefficients of the best-fit lines to the measured total density slopes ($\overline{\gamma}$) using different dynamical and lensing studies.

Sample	N	a	b_0	Δ
Dynamics				
Frontier Fields (Derkenne et al., 2021)	80			
MUSE sample (this work)	101	2.14 ± 0.01	0.02 ± 0.12	0.20
Lensing				
SLACS (Auger et al., 2010)	55			
SL2S (Sonnenfeld et al., 2013)	25	2.05 ± 0.02	-0.19 ± 0.10	0.23
BELLS & BELLS Gallery (Li et al., 2018)	40			
Lensing + Dynamics	301	2.11 ± 0.01	-0.09 ± 0.08	0.22

coefficients of the best-fit lines from these combined samples are listed in Table 5.3. In this analysis, I ignore the systematics originating from the underlying methodologies as evaluating the effect of these systematics on measurements is out of the scope of this work.

5.4.4.1 Comparison with Frontier Field sample

Derkenne et al. (2021) used a sample of 90 ETGs from Frontier Fields and measured the total density slopes employing axisymmetric Jeans modeling through the JAMPY package. Similar to this work, the kinematics of these galaxies were extracted from MUSE-Deep cubes, and the surface brightness was modeled as MGEs using HST images. Additionally, they used a cylindrical oriented velocity ellipsoid with a gNFW mass profile and constant anisotropy model. Still, there were some differences in the parameter design, adopted boundaries, and measurement process of the total density slopes. The reported median of the total density slope from this sample is 2.11 ± 0.03. Considering measurements from the $\mathrm{JAM_{cyl}}$ + gNFW model, the median of $\overline{\gamma}$ for the MUSE sample is 2.15 ± 0.03, and if I only consider galaxies within the same redshift range of the Frontier Field then the median becomes 2.17 ± 0.03. These median values are approximately 1.5σ different than each other. The similarity of the studies also provides an opportunity to compare the measured $\overline{\gamma}$ values for the overlapping galaxies from the two samples. I found that there are 18 common galaxies between the MUSE and Frontier Field samples, which were identified by matching the galaxy IDs, coordinates, and redshifts. For the MUSE sample, the measurements from the $\mathrm{JAM_{cyl}}$ + gNFW

model were used as the Frontier Field measurements were coming from a similar model. In Fig. 5.10, I compare the $\overline{\gamma}$ measurements coming from these two samples and I found that in most cases the measurements are within the 1σ uncertainty of each other. This additional consistency check besides the above ones strengthens the validity of this work as these two studies used the same data, tools, and techniques though there were some differences in the underlying model assumptions and analysis processes.

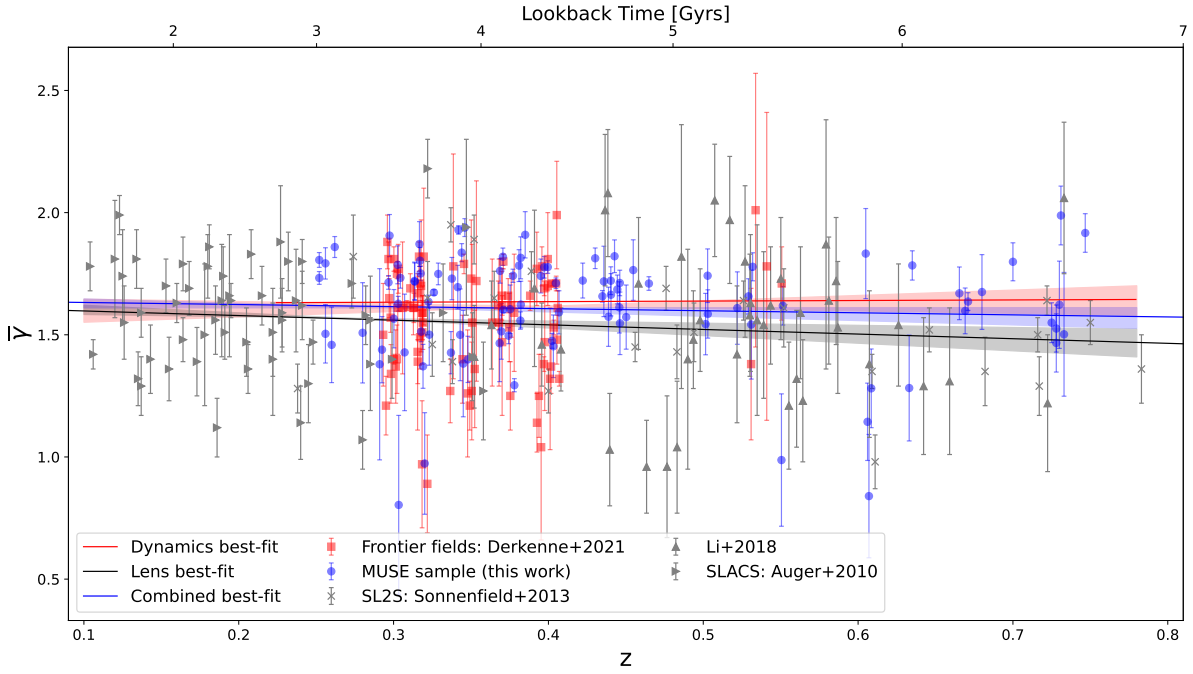


Figure 5.12: Total density slope,$\overline{\gamma}$ as a function of redshift from different dynamical and lensing studies. The measured $\overline{\gamma}$ using dynamical modeling techniques are plotted with non-grey colors - the MUSE values are shown as blue circles and the Frontier Field quantities (Derkenne et al., 2021) as red squares. Total density slopes measured using gravitational lensing techniques (Auger et al., 2010; Sonnenfeld et al., 2013; Li et al., 2018) are presented using different grey markers. The 1σ uncertainties on each estimated $\overline{\gamma}$ are also plotted using associated colors. The red, grey, and blue solid lines show the best-fit lines from the combined dynamics sample (MUSE + Frontier Field), combined lens sample (SLACS + SL2S + BELLS & BELLS Gallery), and combined lens + dynamics sample respectively and the associated shaded region in the same color are 1 σ confidence interval estimated through a bootstrap sampling method. Though the dynamics and lens sample vary in mass and size, their surface mass density distributions, which is the most correlated galaxy parameter to $\overline{\gamma}$, originate from the same underlying population (a two-sample K-S test yields a p-value of 0.11 rejecting the null hypothesis that the underlying surface mass density distribution is different).

5.4.4.2 Redshift evolution in combined Dynamics sample

Around 85% of the galaxies in the Frontier Field sample are within the redshift range $0.3 < z < 0.4$, thus it is not possible to check the redshift evolution within this sample. However, this sample

combined with MUSE would provide a significantly larger sample than either and be helpful to test redshift evolution at intermediate redshift. I performed two-sample Kolmogorov–Smirnov (K-S) tests on the Frontier Field and MUSE samples to check whether they were drawn from the same underlying distribution in terms of effective radius, total mass, and surface mass density. To achieve statistically matched samples I constrained $\log_{10}\Sigma(M_{\odot}\mathrm{kpc}^{-2}) \leq 9.8$ for each sample. After applying the cut, the number of MUSE and Frontier Field samples was reduced to 101 and 80 respectively. I found that the samples' R_e, M_{tot}, and Σ distributions are statistically the same with p-values of 0.96, 0.16, and 0.24 respectively. In Fig 5.11, I plot the number density histograms of these three parameters for both samples. The R_e and M_{tot} quantities for Frontier Field sample were collected from Derkenne et al. (2021) and surface mass density was measured using the equation 5.4. I call this sample the dynamics sample. The MAGPI sample (Derkenne et al., 2023) also used Jeans dynamical modeling method and contains 30 galaxies at around $z \sim 0.3$ to study the environmental effects on the evolution of the total density slope. However, these MAGPI galaxies are on average larger and more massive than both the MUSE and Frontier Field samples and do not statistically match either. Therefore, I did not include this sample in the combined dynamics sample. Other studies in the literature that also employed the dynamical modeling method used galaxies from the local Universe and outside the redshift range of this analysis (e.g. Poci et al., 2017; Bellstedt et al., 2018; Zhu et al., 2023). This combined dynamics sample still contains only 33% of the total galaxies above $z > 0.4$, primarily coming from the MUSE sample. Regardless, I used this sample to measure $\mathrm{d}\overline{\gamma}/\mathrm{d}z$ at intermediate redshift. The combined dynamics sample and the best-fit line fitted through the LtsFit package are shown in Fig. 5.12. The estimated slope from this combined sample is $\mathrm{d}\overline{\gamma}/\mathrm{d}z = 0.02 \pm 0.12$ indicating almost no evolution of total density slope over intermediate redshift range. However, this dynamics sample is dominated by galaxies within the redshift range $0.25 < z < 0.4$ (122 out of 181 galaxies) and may contribute to the reduced sensitivity to redshift trends, compared to an evenly distributed sample. Thus increasing the sample sizes at higher redshifts, with high-quality IFU data will be crucial to determining the slope evolution.

5.4.4.3 Redshift evolution in a combined lens sample

Using massive ETGs acting as strong gravitational lenses, the lensing studies found that the total density slope evolves from shallow to steep over a large redshift baseline. These studies also

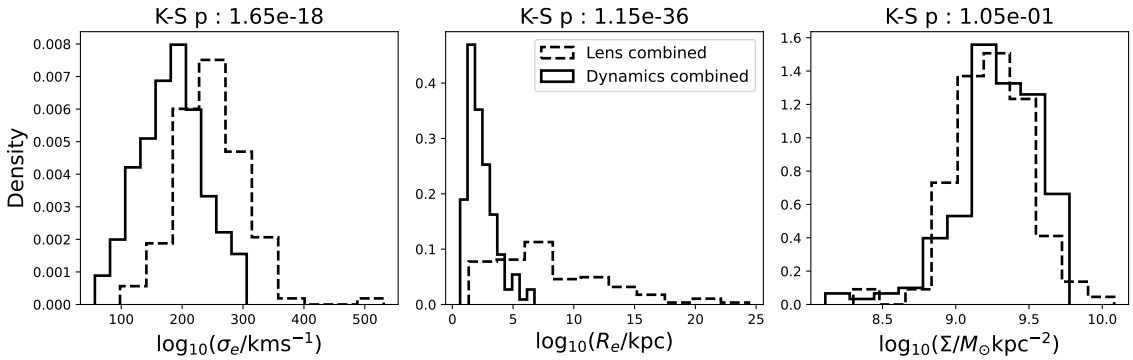


Figure 5.13: The number density histograms of the combined dynamics (dashed line) and lens sample (solid line). From left to right the histograms for velocity dispersion, σ_e, effective radius, R_e, and surface mass density Σ of the two samples are shown. The p-values of the corresponding K-S tests are shown as the title of the respective plots. Though the two samples do not match in mass and size they statistically match over Σ.

observed that the total density slope changes with other parameters such as radius and surface mass density. However, the evolution of $\overline{\gamma}$ with redshift is still found to exist even after considering those parameters (Bolton et al., 2012; Sonnenfeld et al., 2013; Li et al., 2018, e.g.). In this analysis, I only considered SLACS, SL2S, and BELLS samples from Auger et al. (2010), Sonnenfeld et al. (2013) and Li et al. (2018) respectively as these studies are within the redshift range of $0.1 < z < 0.8$, the representative work based on the corresponding sample and provide necessary measurements to incorporate in this analysis. The original sample in Li et al. (2018) included the SL2S sample from Sonnenfeld et al. (2013) that I excluded to omit double-counting of those galaxies. The final combined lens sample of 120 galaxies consists of 55 galaxies from SLACS, 25 from SL2S, and 40 from the BELLS sample. A two-sample K-S test between each pair established that these three samples have the same underlying population distribution concerning velocity dispersion. I showed these lens samples using different grey makers in Fig. 5.12 and found that the slope, $\mathrm{d}\overline{\gamma}/\mathrm{d}z$ from the best-fit line is -0.19 ± 0.10 with an intrinsic RMS scatter of $\Delta = 0.23$. This result is similar to the findings of Sonnenfeld et al. (2013), which is $\mathrm{d}\overline{\gamma}/\mathrm{d}z = -0.10 \pm 0.12$, after combining dependencies of $\overline{\gamma}$ on other galaxy parameters. Next, I combined this lens sample with the dynamics sample to create the largest sample at intermediate redshift.

5.4.4.4 Redshift evolution in a combined dynamics and lens sample

The combined dynamics and lens sample individually provide a different picture of the redshift evolution of the total density slope. While the former suggests an absence of significant evolution,

the latter points to a steeper slope over cosmic time. The dynamics sample predominantly contains ETGs within $0.3 < z < 0.4$ and the lens sample is substantial at higher redshift and also at $z < 0.25$. This distribution over redshift makes these two samples complementary to each other irrespective of their methodological differences and as a combined sample provides the largest redshift baseline to investigate evolution. However, the strong lens ETGs are typically more massive and larger than their non-lensing counterparts and the two samples do not statistically match considering galaxy properties such as mass, radius, and velocity dispersion. The total density slope does not have a strong dependence on mass and velocity dispersion as observed from both dynamical and lensing studies. Contrarily, except for MAGPI all the samples considered in this work observed a prominent correlation between $\overline{\gamma}$, and the surface mass density and effective radius. Motivated by this observation, I checked whether the dynamics and lens samples have Σ distributions originating from the same underlying population. The surface mass densities for the lens samples were computed using the size and mass measurements in the respective works. I found that a two-sample K-S test rejects the null hypothesis that the dynamics and lens samples' surface mass density distributions were generated from the different underlying populations. And, as one would naively expect, they statistically do not match in R_e and σ_e. In Fig. 5.13, I show the number density histograms of these three parameters for both samples with associated p-values of the K-S tests. I combined the dynamic and lens samples based on their statistical resemblance in terms of surface mass density, and the best-fit line for this combined sample of 301 galaxies is depicted as the blue solid line in Fig. 5.12. The estimated variation with redshift, $\mathrm{d}\overline{\gamma}/\mathrm{d}z = -0.10 \pm 0.08$ with observed 1σ intrinsic scatter of $\Delta = 0.22$. This finding is in line with the observations from the lensing studies (e.g. Sonnenfeld et al., 2013) and the measurements from the NFW and gNFW-based JAM models considering all MUSE galaxies. Though this combined lens+dynamics sample is statistically definitive, the difference in the adopted methodologies and associated systematic effects on the measurements and unaccounted correlation of galaxy properties to $\overline{\gamma}$ may pose significant uncertainties to this result. To overcome this situation, we need a large sample evenly distributed over a long baseline to be studied using Jeans dynamical modeling technique. Additionally, the $\overline{\gamma}$ should also be measured from this large sample of lens galaxies using dynamic modeling to decrease systematics in the analysis process. Both of these tasks are out of the scope of this work and would be considered future projects.

5.5 Conclusion

In this Chapter, I analyzed the evolution of the total density slope as a function of cosmic time over intermediate redshift ($0.1 < z < 0.8$) motivated by the contradictory observations from the previous lensing studies and cosmological simulations. Cosmological simulations have found that the total density slope decreases with redshift and becomes close to isotropic ($\overline{\gamma}$= 2) at $z = 0$. However, the lensing studies observed an increasing trend of $\overline{\gamma}$ with redshift becoming steeper at lower redshift even after considering the dependence on other galaxy parameters such as size and surface mass density. I used a sample of ETGs gathered from MUSE-DEEP IFU data and measured the $\overline{\gamma}$ while predicting the kinematics of these galaxies using an axis-symmetric dynamical modeling method. To perform this task I employed six different JAM models that differ in mass profile assumptions (power-law, NFW, and gNFW) and orientations (cylindrical vs spherical) of the adopted velocity ellipsoids. The measurements from this MUSE sample were then compared among the six JAM models and used to estimate $\mathrm{d}\overline{\gamma}/\mathrm{d}z$ from best-fit lines. Additionally, I computed $\mathrm{d}\overline{\gamma}/\mathrm{d}z$ by combining the MUSE sample with other dynamical modeling and lensing studies. Here are the key results from this work

- The comparison of measured $\overline{\gamma}$ values between JAM models with two extreme assumptions of the velocity ellipsoid orientations and different mass profiles suggest that the power-law models tend to overestimate the $\overline{\gamma}$ values, particularly in the spherical orientation, whereas the measurements from the NFW and gNFW models remain mostly consistent and are not biased toward a specific mass model or velocity ellipsoid orientations.

- The slopes, $\mathrm{d}\overline{\gamma}/\mathrm{d}z$ derived from fitting to all MUSE galaxies and only to Qual 2 and 3 galaxies differ but provide a consistent picture. In the case of all galaxies, the $\mathrm{d}\overline{\gamma}/\mathrm{d}z$ from four JAM models (NFW and gNFW models) are around -0.1 and for the other case, it is around -0.4 for all six models. These observations are similar to the findings of the lensing studies and suggest an increment in total density slope with cosmic time.

- I found that the measured $\overline{\gamma}$ has a strong linear relation with effective radius, R_e, and surface mass density Σ with an estimated Pearson correlation coefficient -0.3 and 0.4 respectively. Other samples in lensing and dynamical modeling-based works also observed similar correlations. However, unlike the lensing-based studies, these correlations were not considered

while evaluating the linear relation between $\overline{\gamma}$ and redshift.

- The MUSE sample is a statistically matched sample to the Frontier Field and the measured total density slopes for overlapping members are within 1σ uncertainty of each other suggesting the robustness of those analyses regardless of several differences in the measurement process.

- The combined dynamics sample of 181 galaxies from MUSE and Frontier Field survey indicates an absence of significant evolution over cosmic time at intermediate redshift with $\mathrm{d}\overline{\gamma}/\mathrm{d}z = 0.02 \pm 0.12$.

- The slope, $\mathrm{d}\overline{\gamma}/\mathrm{d}z$ from the combined lens sample of 120 galaxies is -0.19 ± 0.10 with an intrinsic RMS scatter of $\Delta = 0.23$. This result is consistent with the findings of Sonnenfeld et al. (2013), which is $\mathrm{d}\overline{\gamma}/\mathrm{d}z = -0.10 \pm 0.12$, after combining dependencies of $\overline{\gamma}$ on other galaxy parameters.

- Finally, from the combined dynamics + lens sample of 301 galaxies, I measured a trend of $\frac{\mathrm{d}\overline{\gamma}}{\mathrm{d}z} = -0.09 \pm 0.08$ with observed 1σ intrinsic scatter of $\Delta = 0.22$. This finding is in line with the observations from the lensing studies and the measurements from the NFW and gNFW-based JAM models considering all MUSE galaxies.

  Understanding change in total density slope over lookback time is essential for gaining insights into the mechanisms of galaxy formation and evolution. This work with the MUSE sample provides a consistent picture of the evolution of the total density slope of ETGs at intermediate redshifts individually and together with other samples and supports the findings of the lensing studies using an independent method. Despite different underlying assumptions of models and regardless of the difference in the quality of fits, I found that in almost all cases there is an increasing trend of $\overline{\gamma}$ over redshift indicating the total density slopes in ETGs increase at lower redshift. However, a relatively lower number of galaxies at higher redshift and the unaccounted correlations of galaxy parameters to $\overline{\gamma}$ may pose some uncertainties to these results. To resolve this situation, a large sample with high-quality IFU data, evenly distributed over a long redshift baseline, is essential to be studied using Jeans dynamical modeling technique. I hope to carry out such an endeavor in the future.

Chapter 6

Summary and future work

In this dissertation, I conducted extensive research to advance our understanding of both galaxy evolution and cosmology using early-type galaxies (ETGs). By gathering a comprehensive sample of ETGs and extracting their stellar kinematics, I evaluated changes in key galaxy characteristics such as rotational support and the total density slope across redshifts. These analyses have provided insights into the dynamic changes that occur within these galaxies over cosmic time. Additionally, I developed a forward modeling method to collect kinematics data from ETGs that act as gravitational lenses, to enhance the precision of measured Hubble constant by expanding the sample size. This chapter summarizes the main results of this dissertation and discusses some future projects.

6.1 Stellar kinematics of ETGs to increase precision of H_0

The redshifts and velocity dispersions of lensing galaxies, a specialized class of early-type galaxies (ETGs), are critical for determining the Hubble constant through the time-delay strong lensing method. However, the spectra of lensing galaxies often become spatially blended with the much brighter lensed quasar images when using seeing-limited ground-based setups, and obtaining stellar kinematics data with a high signal-to-noise ratio (S/N) becomes challenging. To address this challenge, in Chapter 2, I developed a forward modeling technique that allows for the extraction of 1D spectra of eight lensing galaxies, even in the presence of brighter lensed quasar images. With these extracted spectra, I measured the redshifts and integrated velocity dispersions of these eight deflectors. Six of these lenses had no previously measured velocity dispersions, and for the other two, my measurements align with previously reported values. Additionally, I determined the previously unknown redshifts of the deflectors in J0818-2613 and J1817+2729. I also assessed

the potential covariance among the velocity dispersion measurements of the seven deflectors and found that covariances are generally negligible, though they should be considered in a few cases. Achieving percent-level precision in the measured H_0 requires a sample of 40 or more time-delay lenses with available stellar kinematics of the deflectors. The results presented in Chapter 2 contribute to this goal by expanding the current sample size.

6.2 A MUSE sample of ETGs to study galaxy evolution

The assembly history of mass and angular momentum in early-type galaxies are still open questions. To resolve these questions, a large number of studies have been conducted using ETGs in the local Universe, ETGs while similar studies were lacking at intermediate redshifts. One key reason behind this is the lack of availability of a statistically large sample with high-quality data. To bridge this gap, I gathered a sample of 180 galaxies at redshifts $0.25 < z < 0.75$ in Chapter 3. Utilizing MUSE-DEEP cubes, I extracted resolved kinematics of these galaxies up to a few effective radii and measured various kinematic, morphological, and stellar population properties. From my measurements, I found that regular rotators exhibit higher λ_R values compared to non-regular ones, confirming that regular rotators at intermediate redshifts are predominantly supported by ordered motion, whereas non-regular rotators are mostly supported by random motions. This trend has also been observed in the low redshift galaxies. For most galaxies, the measured λ_R values aligned with the visual classification derived from the extracted kinematics map. I also assessed the kinematic misalignment of these galaxies and found that similar to local ETGs, most regular rotators have a kinematic-photometric position angle misalignment below $|10°|$. Furthermore, I observed a strong correlation between the stellar population properties such as age, metallicity ([Z/H]), and mass-to-light ratio (M_*/L) with stellar velocity dispersion (σ_e). Similar to the early-type galaxies in the local Universe, the age, [Z/H], and M_*/L of these galaxies follow a line of constant σ_e on the mass-size plane. Additionally, my analysis showed that galaxies with an older population tend to be more metal-rich than those with a younger population at constant σ_e and overall metallicities increase with higher σ_e. These findings align with results from the MaNGA survey at low redshift and the LEGA-C sample at intermediate redshift. Overall, these observations suggest that the fundamental processes driving the evolution of ETGs, such as mergers and accretion, have remained relatively stable across different epochs. Additionally, these results enhance our understanding of the role of

ETGs in the larger context of cosmic evolution, as it suggests a continuity in their structural and kinematic characteristics over billions of years. I used the measured galaxy properties and extracted kinematics of this MUSE sample to explore two key questions in galaxy evolution in Chapters 4 and 5.

6.3 ETGs show evidence of a decrease in rotation support over cosmic time

In Chapter 4, I explored the level of rotational support in early-type galaxies (ETGs) across different cosmic epochs, by comparing the MUSE sample at intermediate redshift ($0.25 < z < 0.75$) with the MaNGA ETGs at low redshift ($0.0 < z < 0.05$). To conduct this analysis, I corrected the observed λ_R values of the MUSE sample for PSF effects following the same method applied to MaNGA ETGs. My comprehensive analysis confirms a significant decrease in rotational support in ETGs over cosmic time. I verified that the choice of apertures in measuring λ_R did not affect our conclusions even though an aperture size influences λ_R values. Additionally, my findings demonstrated that galaxies in both MUSE and MaNGA samples exhibit less rotational support with increasing stellar mass and/or velocity dispersion. This pattern aligns with previous observations of local ETGs and intermediate redshift quiescent galaxies, underscoring that stellar mass and velocity dispersion are reliable predictors of angular momentum and rotational support in ETGs at $z < 1$. The findings suggest that ETGs maintain consistent dynamical structures across different redshifts. Nonetheless, the underlying physical mechanisms responsible for the variations in rotational support are actively debated. This research contributes to a deeper understanding of the dynamical evolution of ETGs over cosmic time, underscoring the necessity of in-depth kinematic studies to decipher the intricate details of galaxy evolution.

6.4 Redshift evolution of the total density slope of ETGs

At intermediate redshift ($0.1 < z < 0.8$), previous lensing studies and cosmological simulations present conflicting views on the evolution of the total density slope of early-type galaxies (ETGs). To address this discrepancy, in Chapter 5, I examined the evolution of the $\overline{\gamma}$ values of MUSE galaxies as a function of cosmic time. I employed six different JAM models to measure $\overline{\gamma}$, which varied in their mass profile assumptions (power-law, NFW, and gNFW) and velocity ellipsoid orientations

(cylindrical vs. spherical). Comparing these models, I found that the NFW and gNFW models are generally consistent with each other, indicating they are unbiased regarding specific mass models or velocity ellipsoid orientations. In contrast, the power-law models tend to overestimate the $\overline{\gamma}$ values. The best-fit slopes, $\mathrm{d}\overline{\gamma}/\mathrm{d}z$, calculated from all galaxies using these models, fall within each other's uncertainty range, as is the case for high-fit-quality galaxies. However, for each model, the slopes differ by approximately 2σ between the full sample and their subset of high-fit-quality galaxies. Notably, except for the power-law models applied to all galaxies, other $\mathrm{d}\overline{\gamma}/\mathrm{d}z$ values are negative, suggesting that $\overline{\gamma}$ increases as redshift decreases. Additionally, I observed a strong linear relationship between the measured $\overline{\gamma}$ and the effective radius R_e and surface mass density Σ, which aligns with findings from previous lensing and dynamical modeling studies. Subsequently, I combined this MUSE sample with other lensing samples and Frontier Field galaxies to form a statistically robust sample. The estimated $\mathrm{d}\overline{\gamma}/\mathrm{d}z$ from the combined dynamics sample is consistent with zero, whereas the combined dynamics and lens sample align more closely with those obtained from the lensing data. This alignment is expected, as the lensing sample dominates both ends of the considered redshift range. However, systematic uncertainties related to measurement methods and unaccounted correlations of galaxy parameters with $\overline{\gamma}$ may introduce significant uncertainties to these results. This study underscores the need for a large sample with high-quality IFU data distributed evenly across a broad redshift baseline. Such a dataset would enable more precise measurements of $\overline{\gamma}$ and provide deeper insights into the galaxy mass distribution, its assembly, and its evolution over cosmic time.

6.5 Future work

My current research involves extracting and applying stellar kinematics information of early-type galaxies to study galaxy evolution and cosmology. For this purpose, I have gathered a sample of approximately 180 massive ETGs with IFU data within the redshift range 0.25-0.75, which is the first of its kind to the best of my knowledge. I have extracted their kinematics and studied their global structural, kinematic, and morphological properties. In my future research, I will utilize this sample as well as other new data such as observations from the Keck Cosmic Web Imager (KCWI) and James Web Space Telescope (JWST), and incorporate new techniques to address unresolved questions in galaxy evolution. Additionally, I will continue to work on improving the precision

of the H_0 measurement via time-delay cosmography (TDCOSMO). Here are some of the future endeavors that I will perform :

- One of the goals of compiling the MUSE sample was to select a subset of ETGs whose redshift and integrated velocity dispersion match the range of the TDCOSMO sample of lensing galaxies. The resolved kinematics data extracted from this selected non-lensed sample can provide insights into the global anisotropy of TDCOSMO-like early-type galaxies at the population level. I will work to generate a posterior distribution of the global kinematic anisotropy parameter for this sample and incorporate it as a prior in the Bayesian hierarchical framework for H_0 inference. This informed prior will help to mitigate the mass-anisotropy degeneracy and achieve the goal of measuring H_0 with a percent level precision.

- Stellar kinematics of lens galaxies, particularly resolved kinematics, are key to improving the precision of measured H_0 when one chooses not to break the mass-sheet degeneracy artificially, the dominant source of uncertainty in time-delay cosmography method, by assuming a mass profile a priori. However, extracting resolved kinematics is a challenging task. Therefore, I will work to develop methodologies to collect reliable stellar kinematics data from lens galaxies and incorporate them in the H_0 inference.

- In Shajib et al. (2023), we have modeled resolved kinematics data using axisymmetric Jeans equations and incorporated time-delay and lensing data as prior in the Bayesian inference of H_0. However, simultaneous modeling of the high-resolution image of the lens system along with resolved stellar kinematics data would enable us to exploit this data set to its full potential (Yıldırım et al., 2020, 2023). Hence, I want to modify the hierarchical Bayesian approach, where both lensing and dynamical parameters could be sampled together. This joint lens-dynamical modeling will have better constraining power to infer H_0 for a particular sample and will reach its full potential by incorporating data from all the available time-delay and non-time-delay lens systems.

- From studies with local galaxies (e.g. Cappellari, 2016) and from my current work, it is evident that different morphological galaxy properties, such as age, metallicity, mass-to-light ratios, etc. strongly depend on velocity dispersion. Consequently, when combining

a sample of lens galaxies across a range of redshifts with similar velocity dispersions, it is often assumed that they originate from the same underlying population, overlooking the fact that other morphological properties, such as total density slope, kinematic anisotropy, and dark matter fractions, may not be as strongly correlated with velocity dispersion. Hence, it is worth evaluating whether a sample of galaxies having similar velocity dispersion also exhibit a similar trend in the above galaxy properties and there is no significant redshift evolution. I want to combine a sample of lens galaxies including TDCOSMO, SHARP and SL2S lenses and conduct this analysis. This analysis will also help to investigate whether there is any morphological difference between time-delay and non-time-delay early-type galaxies from similar redshift (e.g. TDCOSMO vs SL2S vs SHARP).

6.6 Final remarks

In this dissertation, I worked to enhance our understanding of galaxy evolution and cosmology by studying early-type galaxies (ETGs). However, to improve the precision of these results, it is crucial to have a larger sample of ETGs at intermediate redshifts with higher-quality data. The advent of new space- and ground-based telescopes, such as the JWST, and the Extremely Large Telescope (ELT), will make it possible to gather such datasets. These extensive datasets will also provide us with a sufficient number of ETGs that act as gravitational lenses to closely investigate their internal structures. With a sample of 40 lens systems with suitable data, it is anticipated to achieve a $\sim 1\%$ precision in H_0 enabling us to distinguish between early- and late-time estimates of H_0 at 5σ precision.

References

Abbott, T. M. C. et al. 2018, MNRAS, 480, 3879, 1711.00403

Abdalla, E. et al. 2022, Journal of High Energy Astrophysics, 34, 49, 2203.06142

Agnello, A., Grillo, C., Jones, T., Treu, T., Bonamigo, M., & Suyu, S. H. 2018, MNRAS, 474, 3391, 1702.03942

Aiola, S. et al. 2020, JCAP, 2020, 047, 2007.07288

Alam, S. et al. 2015, ApJS, 219, 12, 1501.00963

Argo, M. K. et al. 2003, MNRAS, 338, 957, astro-ph/0210234

Auger, M. W., Treu, T., Bolton, A. S., Gavazzi, R., Koopmans, L. V. E., Marshall, P. J., Moustakas, L. A., & Burles, S. 2010, ApJ, 724, 511, 1007.2880

Bacon, R. et al. 2010, in Society of Photo-Optical Instrumentation Engineers (SPIE) Conference Series, Vol. 7735, Ground-based and Airborne Instrumentation for Astronomy III, ed. I. S. McLean, S. K. Ramsay, & H. Takami, 773508, 2211.16795

Bacon, R., Piqueras, L., Conseil, S., Richard, J., & Shepherd, M. 2016, MPDAF: MUSE Python Data Analysis Framework, Astrophysics Source Code Library, record ascl:1611.003, 1611.003

Barbary, K. 2016, Journal of Open Source Software, 1, 58

Barnes, J. E., & Hernquist, L. E. 1991, ApJ, 370, L65

Beifiori, A., Maraston, C., Thomas, D., & Johansson, J. 2011, A&A, 531, A109, 1012.3428

Belli, S., Newman, A. B., & Ellis, R. S. 2017, ApJ, 834, 18, 1608.00608

Bellstedt, S. et al. 2018, MNRAS, 476, 4543, 1803.02373

Berghea, C. T., Nelson, G. J., Rusu, C. E., Keeton, C. R., & Dudik, R. P. 2017, ApJ, 844, 90, 1705.08359

Bezanson, R. et al. 2018, ApJ, 858, 60, 1804.02402

Binney, J., & Tremaine, S. 1987, Galactic dynamics

Birrer, S., Amara, A., & Refregier, A. 2016, JCAP, 2016, 020, 1511.03662

Birrer, S. et al. 2020, A&A, 643, A165

Birrer, S., & Treu, T. 2021, A&A, 649, A61

Birrer, S. et al. 2019, MNRAS, 484, 4726, 1809.01274

Blakeslee, J. P., Jensen, J. B., Ma, C.-P., Milne, P. A., & Greene, J. E. 2021, ApJ, 911, 65, 2101.02221

Bolton, A. S. et al. 2012, ApJ, 757, 82, 1201.2988

Browne, I. W. A. et al. 2003, MNRAS, 341, 13, astro-ph/0211069

Bruzual, G., & Charlot, S. 2003, MNRAS, 344, 1000, astro-ph/0309134

Bryant, J. J. et al. 2015, MNRAS, 447, 2857, 1407.7335

Bundy, K. et al. 2015, ApJ, 798, 7, 1412.1482

Calzetti, D., Armus, L., Bohlin, R. C., Kinney, A. L., Koornneef, J., & Storchi-Bergmann, T. 2000, ApJ, 533, 682, astro-ph/9911459

Cappellari, M. 2002, MNRAS, 333, 400, astro-ph/0201430

——. 2008, MNRAS, 390, 71, 0806.0042

——. 2016, ARA&A, 54, 597, 1602.04267

——. 2017, MNRAS, 466, 798, 1607.08538

——. 2020, MNRAS, 494, 4819, 1907.09894

——. 2023, MNRAS, 526, 3273, 2208.14974

Cappellari, M., & Copin, Y. 2003, MNRAS, 342, 345, astro-ph/0302262

Cappellari, M., & Emsellem, E. 2004, PASP, 116, 138, astro-ph/0312201

Cappellari, M. et al. 2007, MNRAS, 379, 418, astro-ph/0703533

——. 2011, MNRAS, 413, 813, 1012.1551

——. 2013a, MNRAS, 432, 1862, 1208.3523

——. 2015, ApJ, 804, L21, 1504.00075

——. 2013b, MNRAS, 432, 1709, 1208.3522

Chambers, K. C. et al. 2016, arXiv e-prints, arXiv:1612.05560, 1612.05560

Chen, G. C. F. et al. 2021a, arXiv e-prints, arXiv:2107.10304, 2107.10304

——. 2019, MNRAS, 490, 1743, 1907.02533

Chen, G. C. F., Fassnacht, C. D., Suyu, S. H., Yıldırım, A., Komatsu, E., & Luis Bernal, J. 2021b, A&A, 652, A7, 2011.06002

Choi, J., Dotter, A., Conroy, C., Cantiello, M., Paxton, B., & Johnson, B. D. 2016, ApJ, 823, 102, 1604.08592

Cleveland, W. S., & Devlin, S. J. 1988, Journal of the American Statistical Association, 83, 596

Conroy, C., & Gunn, J. E. 2010, ApJ, 712, 833, 0911.3151

Conroy, C., Gunn, J. E., & White, M. 2009, ApJ, 699, 486, 0809.4261

Courbin, F. et al. 2018, A&A, 609, A71

de Zeeuw, P. T. et al. 2002, MNRAS, 329, 513, astro-ph/0109511

Delchambre, L. et al. 2019, A&A, 622, A165, 1807.02845

Derkenne, C. et al. 2023, MNRAS, 522, 3602, 2306.09630

Derkenne, C., McDermid, R. M., Poci, A., Remus, R.-S., Jørgensen, I., & Emsellem, E. 2021, MNRAS, 506, 3691, 2107.05206

Dolag, K. 2015, IAU General Assembly, 29, 2250156

Domínguez Sánchez, H., Margalef, B., Bernardi, M., & Huertas-Company, M. 2022, MNRAS, 509, 4024, 2110.10694

Dutton, A. A., & Treu, T. 2014, MNRAS, 438, 3594, 1303.4389

Eigenbrod, A., Courbin, F., Dye, S., Meylan, G., Sluse, D., Vuissoz, C., & Magain, P. 2006, A&A, 451, 747, astro-ph/0510641

Emsellem, E. et al. 2011, MNRAS, 414, 888, 1102.4444

——. 2007, MNRAS, 379, 401, astro-ph/0703531

Emsellem, E., Monnet, G., & Bacon, R. 1994, A&A, 285, 723

European Southern Observatory (ESO). 2017, MUSE reduced data obtained by standard ESO pipeline processing, co-added across multiple observations

Falco, E. E., Gorenstein, M. V., & Shapiro, I. I. 1985, ApJ, 289, L1

Falcón-Barroso, J., Sánchez-Blázquez, P., Vazdekis, A., Ricciardelli, E., Cardiel, N., Cenarro, A. J., Gorgas, J., & Peletier, R. F. 2011, A&A, 532, A95, 1107.2303

Falcón-Barroso, J. et al. 2019, A&A, 632, A59, 1910.06236

Foreman-Mackey, D., Hogg, D. W., Lang, D., & Goodman, J. 2013, PASP, 125, 306, 1202.3665

Freedman, W. L. et al. 2020, ApJ, 891, 57, 2002.01550

Gaia Collaboration et al. 2018, A&A, 616, A1, 1804.09365

Gavazzi, R., Treu, T., Rhodes, J. D., Koopmans, L. V. E., Bolton, A. S., Burles, S., Massey, R. J., & Moustakas, L. A. 2007, ApJ, 667, 176, astro-ph/0701589

Gilman, D., Birrer, S., & Treu, T. 2020, A&A, 642, A194, 2007.01308

Girardi, L., Bressan, A., Bertelli, G., & Chiosi, C. 2000, A&AS, 141, 371, astro-ph/9910164

Goicoechea, L. J., & Shalyapin, V. N. 2019, ApJ, 887, 126, 1911.12123

Gomer, M. R., Sluse, D., van de Vyvere, L., Birrer, S., & Courbin, F. 2022, arXiv e-prints, arXiv:2209.02076, 2209.02076

Graham, M. T. et al. 2018, MNRAS, 477, 4711, 1802.08213

Guérou, A. et al. 2017, A&A, 608, A5, 1710.07694

Hilz, M., Naab, T., & Ostriker, J. P. 2013, MNRAS, 429, 2924, 1206.5004

Hoaglin, D. C., Mosteller, F., & Tukey, J. W. 1983, Understanding robust and exploratory data anlysis

Hogg, D. W., Baldry, I. K., Blanton, M. R., & Eisenstein, D. J. 2002, arXiv e-prints, astro, astro-ph/0210394

Horne, K. 1986, PASP, 98, 609

Inada, N. et al. 2003, AJ, 126, 666, astro-ph/0304377

Inami, H. et al. 2017, A&A, 608, A2, 1710.03773

Jauzac, M., Klein, B., Kneib, J.-P., Richard, J., Rexroth, M., Schäfer, C., & Verdier, A. 2021, MNRAS, 508, 1206, 2006.10700

Jeans, J. H. 1922, MNRAS, 82, 122

Jee, I., Komatsu, E., & Suyu, S. H. 2015, JCAP, 2015, 033, 1410.7770

Jee, I., Komatsu, E., Suyu, S. H., & Huterer, D. 2016, JCAP, 2016, 031, 1509.03310

Kochanek, C. S. 2020, MNRAS, 493, 1725, 1911.05083

——. 2021, MNRAS, 501, 5021, 2003.08395

Koopmans, L. V. E., & Treu, T. 2004, in Astrophysics and Space Science Library, Vol. 301, Astrophysics and Space Science Library, ed. M. Plionis, 23, astro-ph/0308056

Koopmans, L. V. E., Treu, T., Bolton, A. S., Burles, S., & Moustakas, L. A. 2006, ApJ, 649, 599, astro-ph/0601628

Koopmans, L. V. E., Treu, T., Fassnacht, C. D., Blandford, R. D., & Surpi, G. 2003, ApJ, 599, 70, astro-ph/0306216

Kourkchi, E. et al. 2020, ApJ, 902, 145, 2009.00733

Krajnović, D., Cappellari, M., de Zeeuw, P. T., & Copin, Y. 2006, MNRAS, 366, 787, arXiv:astro-ph/0512200

Kundić, T. et al. 1997, ApJ, 482, 75, astro-ph/9610162

Lagattuta, D. J. et al. 2010, ApJ, 716, 1579, 0911.2236

——. 2019, MNRAS, 485, 3738, 1904.02158

Law, D. R. et al. 2016, AJ, 152, 83, 1607.08619

Lee, C. H. 2017, A&A, 605, L8, 1708.05131

Lemon, C. et al. 2022, arXiv e-prints, arXiv:2206.07714, 2206.07714

Lemon, C. A., Auger, M. W., & McMahon, R. G. 2019, MNRAS, 483, 4242, 1810.04480

Li, R. et al. 2019, MNRAS, 490, 2124, 1903.09282

Li, R., Shu, Y., & Wang, J. 2018, MNRAS, 480, 431, 1805.06624

Lu, S., Zhu, K., Cappellari, M., Li, R., Mao, S., & Xu, D. 2023, MNRAS, 526, 1022, 2304.11712

Mahler, G. et al. 2018, MNRAS, 473, 663, 1702.06962

Marigo, P., Girardi, L., Bressan, A., Groenewegen, M. A. T., Silva, L., & Granato, G. L. 2008, A&A, 482, 883, 0711.4922

McKean, J. P., Koopmans, L. V. E., Browne, I. W. A., Fassnacht, C. D., Blandford, R. D., Lubin, L. M., & Readhead, A. C. S. 2004, MNRAS, 350, 167, astro-ph/0402116

Melo, A. et al. 2021, A&A, 656, A108, 2110.01575

Mihos, J. C., & Hernquist, L. 1994, ApJ, 425, L13

Millon, M. et al. 2020a, A&A, 640, A105, 2002.05736

——. 2020b, A&A, 639, A101, 1912.08027

Moffat, A. F. J. 1969, A&A, 3, 455

Mozumdar, P., Fassnacht, C. D., Treu, T., Spiniello, C., & Shajib, A. J. 2023, A&A, 672, A20, 2209.14320

Myers, S. T. et al. 2003, MNRAS, 341, 1, astro-ph/0211073

Naab, T., & Ostriker, J. P. 2017, ARA&A, 55, 59, 1612.06891

Navarro, J. F., Frenk, C. S., & White, S. D. M. 1996, ApJ, 462, 563, astro-ph/9508025

Ofek, E. O., Maoz, D., Rix, H.-W., Kochanek, C. S., & Falco, E. E. 2006, ApJ, 641, 70, astro-ph/0510465

Oke, J. B. et al. 1995, PASP, 107, 375

Oscoz, A., Mediavilla, E., Goicoechea, L. J., Serra-Ricart, M., & Buitrago, J. 1997, ApJ, 479, L89

Oscoz, A., Serra-Ricart, M., Goicoechea, L. J., Buitrago, J., & Mediavilla, E. 1996, ApJ, 470, L19

Perley, D. A. 2019, PASP, 131, 084503, 1903.07629

Pesce, D. W. et al. 2020, ApJ, 891, L1, 2001.09213

Pillepich, A. et al. 2018, MNRAS, 473, 4077, 1703.02970

Planck Collaboration et al. 2020, A&A, 641, A6, 1807.06209

Poci, A., Cappellari, M., & McDermid, R. M. 2017, MNRAS, 467, 1397, 1612.05805

Prochaska, J. et al. 2020, The Journal of Open Source Software, 5, 2308, 2005.06505

Refsdal, S. 1964, MNRAS, 128, 307

Remus, R.-S., Dolag, K., Naab, T., Burkert, A., Hirschmann, M., Hoffmann, T. L., & Johansson, P. H. 2017, MNRAS, 464, 3742, 1603.01619

Richard, J. et al. 2021, A&A, 646, A83, 2009.09784

Riess, A. G. et al. 2021, arXiv e-prints, arXiv:2112.04510, 2112.04510

Ruff, A. J., Gavazzi, R., Marshall, P. J., Treu, T., Auger, M. W., & Brault, F. 2011, ApJ, 727, 96, 1008.3167

Rusu, C. E. et al. 2017, MNRAS, 467, 4220, 1607.01047

Rusu, C. E., & Lemon, C. A. 2018, Research Notes of the American Astronomical Society, 2, 187, 1810.00479

Rusu, C. E. et al. 2020, MNRAS, 498, 1440, 1905.09338

Salpeter, E. E. 1955, ApJ, 121, 161

Sánchez, S. F. et al. 2012, A&A, 538, A8, 1111.0962

Sánchez-Blázquez, P. et al. 2006, MNRAS, 371, 703, astro-ph/0607009

Schmidt, T. et al. 2022, arXiv e-prints, arXiv:2206.04696, 2206.04696

Schneider, P., & Sluse, D. 2013, A&A, 559, A37, 1306.0901

Schwarzschild, M. 1979, ApJ, 232, 236

Shajib, A. J. et al. 2020, MNRAS, 494, 6072, 1910.06306

——. 2019, MNRAS, 483, 5649, 1807.09278

——. 2023, A&A, 673, A9, 2301.02656

Shajib, A. J., Treu, T., & Agnello, A. 2018, MNRAS, 473, 210, 1709.01517

Shajib, A. J. et al. 2022, arXiv e-prints, arXiv:2202.11101, 2202.11101

Shalyapin, V. N., & Goicoechea, L. J. 2017, ApJ, 836, 14, 1701.04272

Sheinis, A. I., Bolte, M., Epps, H. W., Kibrick, R. I., Miller, J. S., Radovan, M. V., Bigelow, B. C., & Sutin, B. M. 2002, PASP, 114, 851, astro-ph/0204297

Sluse, D., Claeskens, J. F., Hutsemékers, D., & Surdej, J. 2007, A&A, 468, 885, astro-ph/0703030

Sluse, D. et al. 2019, MNRAS, 490, 613, 1905.08800

Sonnenfeld, A. 2018, MNRAS, 474, 4648, 1710.05925

Sonnenfeld, A., Treu, T., Gavazzi, R., Suyu, S. H., Marshall, P. J., Auger, M. W., & Nipoti, C. 2013, ApJ, 777, 98, 1307.4759

Stern, D. et al. 2021, ApJ, 921, 42, 2012.10051

Suyu, S. H. et al. 2017, MNRAS, 468, 2590, 1607.00017

——. 2014, ApJ, 788, L35, 1306.4732

Tortorelli, L. et al. 2018, MNRAS, 477, 648, 1803.02375

Tran, K.-V., Sahu, N., Suyu, S., Shajib, A., & AGEL Survey. 2024, in American Astronomical Society Meeting Abstracts, Vol. 243, American Astronomical Society Meeting Abstracts, 326.05

Treu, T., & Koopmans, L. V. E. 2002, MNRAS, 337, L6, astro-ph/0210002

Treu, T., & Koopmans, L. V. E. 2004, ApJ, 611, 739, astro-ph/0401373

Treu, T., & Marshall, P. J. 2016, The Astronomy and Astrophysics Review, 24

Valdes, F., Gupta, R., Rose, J. A., Singh, H. P., & Bell, D. J. 2004, ApJS, 152, 251, astro-ph/0402435

van de Sande, J. et al. 2017, ApJ, 835, 104, 1611.07039

Van de Vyvere, L., Gomer, M. R., Sluse, D., Xu, D., Birrer, S., Galan, A., & Vernardos, G. 2022, A&A, 659, A127, 2112.03932

van der Wel, A. et al. 2016, ApJS, 223, 29, 1603.05479

van Dokkum, P. G. et al. 2015, ApJ, 813, 23, 1506.03085

Vanzella, E. et al. 2021, A&A, 646, A57, 2009.08458

Verde, L., Treu, T., & Riess, A. G. 2019, Nature Astronomy, 3, 891, 1907.10625

Wake, D. A. et al. 2017, AJ, 154, 86, 1707.02989

Wang, Y. et al. 2019, MNRAS, 490, 5722, 1910.08552

Weaver, J. R. et al. 2022, ApJS, 258, 11, 2110.13923

Weilbacher, P. M. et al. 2020, A&A, 641, A28, 2006.08638

Westfall, K. B. et al. 2019, AJ, 158, 231, 1901.00856

White, S. D. M., & Frenk, C. S. 1991, ApJ, 379, 52

Wisnioski, E. et al. 2015, ApJ, 799, 209, 1409.6791

Wong, K. C. et al. 2017, MNRAS, 465, 4895, 1607.01403

——. 2020, MNRAS, 498, 1420, 1907.04869

Wyithe, J. S. B., Turner, E. L., & Spergel, D. N. 2001, ApJ, 555, 504, astro-ph/0007354

Xu, D., Sluse, D., Schneider, P., Springel, V., Vogelsberger, M., Nelson, D., & Hernquist, L. 2016, MNRAS, 456, 739, 1507.07937

Yıldırım, A., Suyu, S. H., Chen, G. C. F., & Komatsu, E. 2023, A&A, 675, A21, 2109.14615

Yıldırım, A., Suyu, S. H., & Halkola, A. 2020, MNRAS, 493, 4783, 1904.07237

York, D. G. et al. 2000, AJ, 120, 1579, astro-ph/0006396

York, T. et al. 2005, MNRAS, 361, 259, astro-ph/0505093

Zhu, K., Lu, S., Cappellari, M., Li, R., Mao, S., & Gao, L. 2023, MNRAS, 522, 6326, 2304.11711